

Diese Dissertation haben begutachtet:

.....



## DISSERTATION

# THz spectroscopy of novel spin and quantum Hall systems

ausgeführt zum Zwecke der Erlangung des akademischen Grades eines  
Doktors der Naturwissenschaften unter der Leitung von

Univ.Prof. Dr.rer.nat. Andrei Pimenov

E138 Institut für Festkörperphysik

eingereicht an der Technischen Universität Wien  
Fakultät für Physik

von

Uladzislau Dziom

Matrikelnummer: 01228578

Wasagasse 23/4, 1090 Wien

Wien, am 10. April 2018



# Kurzfassung

In dieser Arbeit werden Ergebnisse von der Untersuchung verschiedener Tieftemperaturphänomene mittels Ferninfrarotspektroskopie präsentiert. Die meisten Experimente wurden mit einem Mach-Zehnder-Interferometer im Bereich von 40–1200 GHz durchgeführt. Zusätzlich zu der klassischen Messung der Absorption wurde besondere Aufmerksamkeit auf die Untersuchung der Drehung der Polarisationssebene gelegt. Zu den untersuchten Systemen gehören zweidimensionale Elektronengase (HgTe/CdHgTe-Quantenwells mit kritischer Dicke und GaAs/AlGaAs-Heteroübergänge) sowie multiferroisches Dysprosium-Manganit.

Die elektronische Bandstruktur in HgTe/CdHgTe-Quantenwells wird durch eine starke Spin-Bahn-Wechselwirkung in Quecksilbertellurid beeinflusst. Nach theoretischen Berechnungen nimmt die Bandstruktur bei einer kritischen Dicke (6.6 nm) der HgTe-Schicht eine Form ähnlich einem Dirac-Kegel an. Diese Vorhersage wurde durch Messungen der Zyklotronresonanz experimentell bestätigt. Die beobachtete Abhängigkeit der Masse als Funktion der Quadratwurzel der Dichte ist eine direkte Bestätigung der linearen Dispersionsrelation der Elektronen. In den Proben, deren Fermienergie in der unteren Hälfte des Dirac-Kegels liegt, ermöglichten Messungen der Rotation der Polarisationssebene bei 320–340 GHz eine Beobachtung des dynamischen Quanten-Hall-Effekts. In starken magnetischen Feldern wurde ein quantisiertes Verhalten von dem Rotationswinkel des Faraday-Effekts beobachtet, welches dem Wert der Feinstrukturkonstante ( $1/137$ ) entsprochen hat. Da der Faraday-Winkel in direktem Zusammenhang mit der dynamischen Hall-Leitfähigkeit steht, ist diese ebenfalls quantisiert und zeigt den fundamentalen Wert  $e^2/h$ .

Der dynamische ganzzahlige Quanten-Hall-Effekt wurde außerdem in GaAs/AlGaAs-Heteroübergängen untersucht. Unter 100 GHz wurde eine Quantisierung der Hall-Leitfähigkeit gemessen. Über dieser Frequenz verwischen die Quantenplateaus und werden durch kleine Quantenoszillationen im Realteil der Leitfähigkeit ersetzt. Ähnliche Oszillationen wurden auch im Imaginärteil beobachtet. Dieser Effekt tritt jedoch nicht bei der Nullfrequenz auf, da der Imaginärteil im statischen Fall verschwindet. Die Amplitude der Oszillationen verringert sich mit steigender Frequenz und ab 1 THz zeigt die Hall-Leitfähigkeit kein Merkmal mehr, das mit dem Füllen von Landau-Niveaus verbunden werden könnte. Das Bild, das aus diesen Experimenten entsteht, stimmt teilweise mit analytischen Berechnungen für den Grenzfall, in dem die Störstellen als Deltafunktionen angenommen werden, und dem Grenzfall mit einem glatten Potential überein. Es steht jedoch im Widerspruch zu Ergebnissen von numerischen Berechnungen, die einen Fall zwischen diesen beiden Limits annehmen.

Eine weitere interessante Erscheinungsform der Spin-Bahn-Kopplung wurde im klassischen multiferroischen Manganit  $\text{DyMnO}_3$  nachgewiesen. In diesem Material führt die mikroskopische Spin-Bahn-Wechselwirkung zu einer Kopplung zwischen antiferromagnetischer und ferroelektrischer Ordnung. Aufgrund der intrinsischen magnetoelektrischen Kopplung an Elektromagnonen, rotiert linear polarisierte Terahertzstrahlung bei der Propagation durch die Probe. Amplitude und Richtung der Polarisationsdrehung sind durch die Orientierungen der ferroelektrischen Domänen definiert und können mit einer statischen Spannung verändert werden. Diese Experimente erlauben die elektrische Kontrolle der Terahertz-Polarisation durch die Nutzung des dynamischen magnetoelektrischen Effekts.

# Abstract

This thesis presents results of far-infrared spectroscopic studies of several low-temperature phenomena. Most of the experiments have been carried out in 40–1200 GHz range using a Mach-Zehnder interferometer. In addition to classical measurements of absorption, much attention has been put to the study of rotation of the polarization plane. Among investigated systems are two-dimensional electron gases (HgTe/CdHgTe quantum wells of critical thickness and GaAs/AlGaAs heterojunctions) and multiferroic dysprosium manganite.

The electron band structure in HgTe/CdHgTe quantum wells is affected by a strong spin-orbit interaction in mercury telluride. According to theoretical calculations, the band structure takes a form close to a Dirac cone for a critical thickness (6.6 nm) of the HgTe layer. This prediction was experimentally confirmed by measurements of the cyclotron resonance. In external magnetic field the cyclotron resonance is seen as a dip in a transmission coefficient. Its position is determined by the cyclotron mass and its amplitude is connected to the charge density. The observed square-root dependence of the mass as a function of density provides a direct confirmation of the linear electron dispersion. Measurements of rotation of the polarization plane at 320–340 GHz allowed to observe the dynamic quantum Hall effect in the samples, in which the Fermi level is in the lower part of the Dirac cone. In high magnetic fields the Faraday rotation angle was found to demonstrate a quantized behavior, taking a value of the fine-structure constant ( $1/137$ ). The Faraday angle is directly connected to the dynamic Hall conductivity, which is thus also quantized, showing the universal value  $e^2/h$ .

The dynamic integer quantum Hall effect has been also studied in GaAs/AlGaAs heterojunctions. Quantization of the Hall conductivity has been detected below 100 GHz. Above this frequency the quantum plateaus are smeared out and replaced by small quantum oscillations in the real part of the conductivity. Similar oscillations were observed in the imaginary part as well. This effect has no analog at zero frequency, since the imaginary part is zero in the static case. The amplitude of the oscillations decreases with increasing frequency, and at 1 THz the Hall conductivity does not demonstrate any features related to the filling of Landau levels. This experimental picture is in partial agreement with analytical calculations for a delta-impurity limit and for a limit of a smooth potential, but in a disagreement with the results of numerical calculations for an intermediate case.

Another interesting manifestation of the spin-orbit coupling has been demonstrated in a classical multiferroic manganite  $\text{DyMnO}_3$ . In this material the microscopic spin-orbit interaction leads to a coupling between antiferromagnetic and ferroelectric orders. Because of intrinsic magnetoelectric coupling with electromagnons a linearly polarized terahertz light rotates upon passing through the sample. The amplitude and the direction of the polarization rotation are defined by the orientation of ferroelectric domains and can be changed by static voltage. These experiments allow the terahertz polarization to be electrically tuned using the dynamic magnetoelectric effect.



# Contents

<b>1</b>	<b>Introduction</b>	<b>1</b>
<b>2</b>	<b>Experimental technique and data treatment</b>	<b>3</b>
2.1	Generalization of Fresnel equations for stratified samples . . . . .	3
2.1.1	Plane wave in a linear medium . . . . .	3
2.1.2	Transmission through isotropic dielectric slab and thin metallic film .	5
2.2	Continuous wave sub-THz spectroscopy . . . . .	8
2.2.1	Mach-Zehnder interferometer . . . . .	8
2.2.2	Field distribution between focusing lenses . . . . .	12
2.2.3	Standing waves in spectra . . . . .	14
2.2.4	Standing waves in magnetic field scans . . . . .	17
2.2.5	Signal stability at fixed frequency . . . . .	20
2.2.6	Measuring two signals with one detector . . . . .	22
<b>3</b>	<b>Two-dimensional electron gas in magnetic field</b>	<b>29</b>
3.1	One-electron Drude model . . . . .	29
3.2	Boltzmann equation. Cyclotron mass . . . . .	31
3.3	Superradiant decay and Drude relaxation time . . . . .	34
<b>4</b>	<b>Mercury telluride films with critical thickness</b>	<b>39</b>
4.1	Introduction into physics of HgTe quantum wells . . . . .	39
4.2	HgTe/CdHgTe samples . . . . .	40
4.3	Samples without a gate . . . . .	41
4.3.1	Control of the Fermi level by illumination . . . . .	41
4.3.2	Cyclotron resonance of Dirac-like carriers . . . . .	42
4.3.3	Fitting the transmission using the Drude model . . . . .	45
4.3.4	Drude parameters . . . . .	50
4.3.5	Hole contribution . . . . .	52
4.3.6	Landau level FTIR spectroscopy . . . . .	55
4.3.7	Conclusion . . . . .	58
4.4	Samples with Mylar gates . . . . .	59
4.4.1	Preparation of gates . . . . .	59
4.4.2	Drude parameters . . . . .	60
4.4.3	Band structure reconstruction . . . . .	65
4.4.4	Universal Faraday rotation . . . . .	67

<b>5</b>	<b>Dynamic QHE in GaAs/AlGaAs heterojunctions</b>	<b>73</b>
5.1	Introduction to the dynamic quantum Hall effect . . . . .	73
5.2	Samples . . . . .	74
5.3	DC measurements . . . . .	74
5.4	THz experiments . . . . .	78
5.5	Data processing . . . . .	79
5.6	Real part of the high-frequency Hall conductivity . . . . .	81
5.7	Imaginary part of the high-frequency Hall conductivity . . . . .	83
5.8	Review of theoretical models . . . . .	83
5.9	Summary . . . . .	86
<b>6</b>	<b>Dzyaloshinskii-Moriya electromagnon in dysprosium manganite</b>	<b>87</b>
6.1	Introduction to electromagnons . . . . .	87
6.2	Dzyaloshinskii-Moriya electromagnon in dysprosium manganite . . . . .	88
6.3	Complex correction of crossed transmission . . . . .	91
6.4	Direct observation of dynamic magnetoelectric susceptibility . . . . .	92
6.5	Conclusion . . . . .	96
<b>7</b>	<b>Summary and outlook</b>	<b>97</b>
	<b>Acknowledgments</b>	<b>101</b>
	<b>Bibliography</b>	<b>103</b>
	<b>List of own publications</b>	<b>115</b>

# 1 Introduction

Most part of information coming to the human brain results from analysis of visible light, reflected from surrounding objects. Systematic experimental study of interaction of light with matter was started in XVII century [1]. Since that time, the experimentally accessible frequency range has broadened tremendously, and nowadays it spreads from zero to higher than  $10^{18}$  Hz. Spectroscopy has become one of the most powerful research tools in modern physics. Although radiation of any frequency satisfies the same laws, experimental techniques vary for different ranges. It is challenging to realize the same experimental setup, but  $10^{18}$  times smaller (larger). Interaction of radiation with matter is qualitatively different for radio waves and X-rays. Probing solids with radiation of various wavelengths allows to study their structure on any scale. For example, one can determine energy levels of nuclei using gamma rays and investigate the motion of domain walls by using capacitance spectroscopy at several Hertz.

This work is mostly devoted to the spectral range 40–1100 GHz, which is quite specific [2]. It makes a bridge between two well-recognized ranges. The upper limit of  $\approx 1$  THz can be treated as a lower border of infrared (IR) light and frequencies below 40 GHz can be assigned to the microwave range. In IR spectroscopic experiments the wavelength of radiation is usually much smaller, than typical dimensions of optical elements and samples. The opposite limit is reached at microwaves and an intermediate case takes place in the range 40–1100 GHz. We will call this range “THz”, or “submillimeter”, or “far-IR”, although neither of the terms seems to be absolutely correct. There are several techniques that cover the THz range at least partially. Most of experiments in this work have been carried out using continuous wave transmission spectroscopy. Coherent THz radiation is generated by a backward wave oscillator (BWO). The frequency of radiation can be continuously tuned in a certain range. An interferometric arrangement is used to measure both the amplitude and the phase of transmission coefficients. Chapter 2 describes a general matrix formalism that allows to connect experimentally measured quantities with properties of investigated materials. Second part of chapter 2 contains a basic introduction into the experimental BWO spectroscopy and a consideration of some specific aspects of this method.

Recent extensive studies of HgTe/CdHgTe quantum wells are driven by both fundamental and practical interest. Because of the large atomic number of Hg, electron properties of HgTe are strongly affected by the spin-orbit interaction [3]. In some configurations this interaction leads to the locking between the electron momentum and the electron spin. This locking opens possibilities to use the spin degree of freedom for effective storage and transfer of data. Interest from fundamental science is caused by the possibility to realize Majorana quasiparticles. In 1937 E. Majorana described theoretically a hypothetical elementary particle: a fermion that is its own antiparticle. Thus far no elementary particles with such properties have been found, but quasiparticles in heterostructures, combined of HgTe and a superconductor, do resemble

Majorana fermions [4]. Chapter 4 is devoted to the spectroscopic study of HgTe/CdHgTe quantum wells with a critical thickness of the HgTe layer. In these systems the spin-orbit interaction leads to a nearly linear dispersion of the charge carriers [3, 5]. Thus another kind of relativistic-like quasiparticles is realized in these quantum wells: Dirac fermions. Recent achievements in the growth technology of HgTe/CdHgTe heterostructures allowed to produce ultra-pure samples [6]. The high mobility of the charge carriers allows to probe the band structure via the cyclotron resonance. Another outcome of the increased quality of the samples is an observation of quantized Faraday rotation in sub-THz range. This effect is closely related to the dynamic quantum Hall effect.

Many solid state physicists consider the quantum Hall effect (QHE) to be the most amazing phenomenon in solid state physics [7], discovered in XX century (maybe competing with superconductivity). The perfect quantization of the Hall conductivity is used for resistance calibrations. The QHE has been studied extensively at low frequencies. As frequencies increase to the microwave range, standard transport techniques become inapplicable. In this case the high-frequency Hall conductivity can be measured using a crossed waveguide setup. In preceding experiments the quantum plateaus have been shown to exist up to the upper limit of the microwave range (30–50 GHz) [8, 9], and behavior at even higher frequencies remained unknown thus far. Different theoretical considerations provide opposite predictions for the THz range [10–13]. In order to fill the gap in knowledge, the dynamic Hall effect has been experimentally studied in the range 70–1100 GHz. The spectroscopic experiments were accompanied by simultaneous transport measurements in the van der Pauw geometry, in order to compare static and dynamic Hall conductivities directly. The results of this study are presented in chapter 5.

Another manifestation of the spin-orbit interaction has been demonstrated in dysprosium manganite. At low temperatures this material is a multiferroic: it is ordered antiferromagnetically and ferroelectrically, and these orders are coupled. Intensive study of such multiferroics is driven by the idea to control magnetic properties by electric field and vice versa. Realization of this idea can be used to improve efficiency of memory cells [14]. THz spectroscopy is useful for studying excitations in magnetically ordered materials, since typical frequencies of magnons are in the far-IR range. Because of the coupling between the electric and magnetic orders in dysprosium manganite, some magnons become electrically active (electromagnons). Chapter 6 presents results of experiments, in which such electromagnon was used to control polarization of THz radiation by applying static electric voltage to the sample.

## 2 Experimental technique and data treatment

### 2.1 Generalization of Fresnel equations for stratified samples

In this section we establish connections between quantities, that can be measured in spectroscopic experiments, such as transmission and reflection, with material properties (dielectric permittivity, magnetic permeability, conductivity). We will treat a  $4 \times 4$  matrix formalism, developed by Teitler and Hennis [15] and Berreman [16] in order to analyze transmission and reflection of samples with anisotropic properties. This approach provides an accurate solution of Maxwell's equations in a medium with an arbitrary linear local material relations between electromagnetic fields  $\mathbf{E}$ ,  $\mathbf{D}$ ,  $\mathbf{B}$ ,  $\mathbf{H}$ . A sample is assumed to be an infinite plane-parallel slab, perpendicular to  $z$ -direction. Optionally, the sample can consist of several layers with different properties.

#### 2.1.1 Plane wave in a linear medium

Consider a plane monochromatic electromagnetic wave with angular frequency  $\omega$ , traveling through medium, which can be described by the linear material equations:

$$\begin{pmatrix} D_x \\ D_y \\ D_z \\ B_x \\ B_y \\ B_z \end{pmatrix} = M_\varepsilon \begin{pmatrix} E_x \\ E_y \\ E_z \\ H_x \\ H_y \\ H_z \end{pmatrix}; \quad M_\varepsilon = \begin{pmatrix} \hat{\varepsilon} & \hat{\chi}_{em} \\ \hat{\chi}_{me} & \hat{\mu} \end{pmatrix}, \quad (2.1)$$

where  $M_\varepsilon$  is a  $6 \times 6$  matrix,  $\hat{\varepsilon}$ ,  $\hat{\mu}$ ,  $\hat{\chi}_{em}$  and  $\hat{\chi}_{me}$  are  $3 \times 3$  submatrices, that represent tensors of dielectric permittivity, magnetic permeability, electromagnetic and magnetoelectric permittivity respectively in the chosen coordinate system. In ordinary materials magnetic and magnetoelectric effects are negligible, in this case  $\hat{\mu}$  is an identity matrix,  $\hat{\chi}_{me}$  and  $\hat{\chi}_{em}$  are zero matrices.

For each electromagnetic vector  $\mathbf{E}$ ,  $\mathbf{D}$ ,  $\mathbf{B}$ ,  $\mathbf{H}$  we find solution of Maxwell equations in the form of a plane wave:

$$\mathbf{A}(\mathbf{r}, t) = \mathbf{A}_0 e^{i(\mathbf{q}\mathbf{r} - \omega t)}$$

Taking derivatives of such a vector function gives especially simple results:

$$\nabla \mathbf{A} = i\mathbf{q}\mathbf{A}; \quad \nabla \times \mathbf{A} = i\mathbf{q} \times \mathbf{A}; \quad \frac{\partial \mathbf{A}}{\partial t} = -i\omega \mathbf{A}.$$

After a substitution in Maxwell equations, containing curls, one obtains

$$\begin{aligned} i\mathbf{q} \times \mathbf{H} &= -i\frac{\omega}{c}\mathbf{D}; \\ i\mathbf{q} \times \mathbf{E} &= i\frac{\omega}{c}\mathbf{B}. \end{aligned} \quad (2.2)$$

A cross product of two vectors can be written in a matrix form as a product of a skew-symmetric matrix, consisting of the components of the first vector, and the second vector. After a substitution of material equations (2.1), we obtain the system of six linear equations:

$$\begin{pmatrix} 0 & 0 & 0 & 0 & -q_z & q_y \\ 0 & 0 & 0 & q_z & 0 & -q_x \\ 0 & 0 & 0 & -q_y & q_x & 0 \\ 0 & q_z & -q_y & 0 & 0 & 0 \\ -q_z & 0 & q_x & 0 & 0 & 0 \\ q_y & -q_x & 0 & 0 & 0 & 0 \end{pmatrix} \begin{pmatrix} E_x \\ E_y \\ E_z \\ H_x \\ H_y \\ H_z \end{pmatrix} = -\frac{\omega}{c} M_\varepsilon \begin{pmatrix} E_x \\ E_y \\ E_z \\ H_x \\ H_y \\ H_z \end{pmatrix} \quad (2.3)$$

To have a non-trivial solution for the electromagnetic fields, the system should be degenerate and its determinant must be zero. For a given angular frequency  $\omega$  one can expect an infinite number of solutions, which correspond to different directions of the wave vector  $\mathbf{q}$ . If we fix the direction of propagation, for example, by assuming  $q_x = q_y = 0$ , then zero determinant can be achieved at four values of  $q_z$  only. It follows from the fact, that  $q_z$  appears in four equations, so the determinant of the system is a polynomial of power four with respect to  $q_z$ .

By removing the field components  $E_z$  and  $H_z$ , using lines 3 and 6 in the system (2.3), the problem can be formulated as an eigenvalue problem:

$$q_z \begin{pmatrix} E_x \\ E_y \\ H_x \\ H_y \end{pmatrix} = M_{4 \times 4} \begin{pmatrix} E_x \\ E_y \\ H_x \\ H_y \end{pmatrix}. \quad (2.4)$$

The coefficients of the matrix  $M_{4 \times 4}$  can be directly expressed through the material properties (2.1) and the fixed components  $q_x, q_y$  of the wave vector. Four solutions of this problem correspond to two pair of eigenmodes, traveling in the opposite directions. For example, in a trivial case of vacuum, this method gives two double-degenerate solutions  $q_z = \pm\omega/c$  for the wave vector.

Let us define a column  $X = (E_x \ E_y \ H_x \ H_y)^T$  and  $k = q_z$ . At the given angular frequency  $\omega$  and for fixed components  $q_x, q_y$  any field configuration can be represented by a linear combination of eigenvectors of matrix  $M_{4 \times 4}$  with corresponding exponential multipliers:

$$X(z) = \sum_{i=1}^4 \alpha_i X_i e^{ik_i z} = \begin{pmatrix} X_1 & X_2 & X_3 & X_4 \end{pmatrix} \begin{pmatrix} e^{ik_1 z} & 0 & 0 & 0 \\ 0 & e^{ik_2 z} & 0 & 0 \\ 0 & 0 & e^{ik_3 z} & 0 \\ 0 & 0 & 0 & e^{ik_4 z} \end{pmatrix} \begin{pmatrix} \alpha_1 \\ \alpha_2 \\ \alpha_3 \\ \alpha_4 \end{pmatrix}.$$

Here time and  $x, y$  dependence, given by a multiplier  $e^{i(q_x x + q_y y - \omega t)}$ , is omitted. The matrix of the expansion coefficients  $\alpha_i$  can be expressed through the field at some point  $z_0$  and removed from the expression:

$$K \stackrel{\text{def}}{=} \begin{pmatrix} X_1 & X_2 & X_3 & X_4 \end{pmatrix};$$

$$M(z) \stackrel{\text{def}}{=} K \begin{pmatrix} e^{ik_1 z} & 0 & 0 & 0 \\ 0 & e^{ik_2 z} & 0 & 0 \\ 0 & 0 & e^{ik_3 z} & 0 \\ 0 & 0 & 0 & e^{ik_4 z} \end{pmatrix} K^{-1};$$

$$X(z) = M(z - z_0)X(z_0). \quad (2.5)$$

Equation (2.5) connects electromagnetic field at two planes by the transfer matrix  $M$ . In order to calculate this matrix, one has to solve an eigenproblem for the matrix  $M_{4 \times 4}$ . In some simple cases, treated below, this procedure can be done analytically. If the matrix  $M_\varepsilon$  of permittivity has a lot of non-zero elements, then the analytical expressions become too cumbersome and it is more convenient to find the transfer matrix with the use of numerical algorithms.

### 2.1.2 Transmission through isotropic dielectric slab and thin metallic film

In case of an isotropic dielectric with the complex dielectric permittivity  $\varepsilon$  the transfer matrix has the next form:

$$D(z) = \begin{pmatrix} \cos(kz) & 0 & 0 & \frac{i}{\sqrt{\varepsilon}} \sin(kz) \\ 0 & \cos(kz) & -\frac{i}{\sqrt{\varepsilon}} \sin(kz) & 0 \\ 0 & -i\sqrt{\varepsilon} \sin(kz) & \cos(kz) & 0 \\ i\sqrt{\varepsilon} \sin(kz) & 0 & 0 & \cos(kz) \end{pmatrix}, \quad (2.6)$$

where  $k = \sqrt{\varepsilon}\omega/c$ . Consider an infinite dielectric slab, placed in vacuum between planes  $z = 0$  and  $z = d$ , perpendicular to  $z$ -axis (Fig. 2.1). Assume an incident plane wave with a complex amplitude equal to 1 is created by an external source of radiation. The angular frequency of the wave is assumed to be  $\omega$ , the polarization is linear with  $\mathbf{E} \parallel Ox$  and the incidence is normal. The electromagnetic field of the incident wave is given by

$$\begin{pmatrix} E_x \\ E_y \\ H_x \\ H_y \end{pmatrix} = \begin{pmatrix} 1 \\ 0 \\ 0 \\ 1 \end{pmatrix} e^{i(k_0 z - \omega t)},$$

where  $k_0 = \omega/c$ . The reflected and transmitted waves can be represented as a sum of two linearly polarized waves. The wave with the same polarization  $\mathbf{E} \parallel Ox$  as the incident one is called “parallel” and corresponding amplitudes are assigned with a subscript  $\parallel$ . The wave with

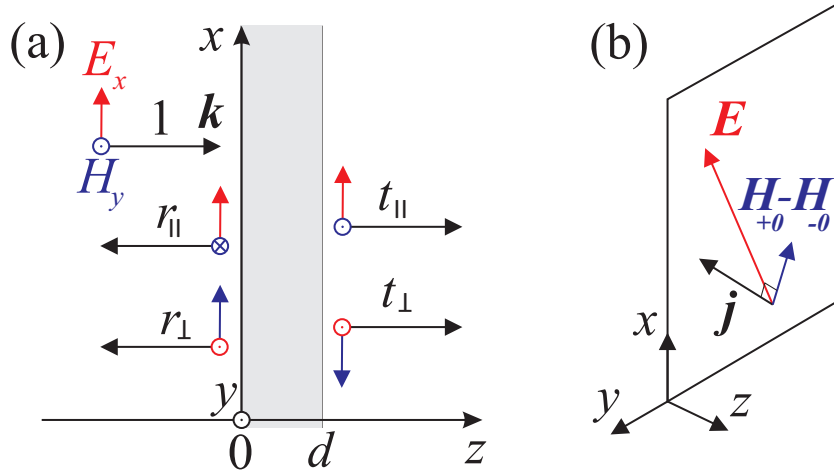


**Figure 2.1:** a) An infinite dielectric slab of thickness  $d$  is perpendicular to  $z$ -axis. A radiation source creates a linearly polarized plane incident wave with a wave vector  $(0, 0, k)$  and amplitude 1. The reflected and transmitted radiation can be represented by a sum of two linearly polarized waves with amplitudes  $r_{\parallel}$ ,  $r_{\perp}$  and  $t_{\parallel}$ ,  $t_{\perp}$  respectively. b) Relation between electromagnetic fields on sides of a thin conducting film. If the film is thin enough, then the tangential components of the electric field are equal on both sides, while the tangential components of the magnetic field differ by  $\frac{4\pi}{c}j$ , where  $j = |\hat{\sigma}\mathbf{E}d|$  is a linear current density, created by the electric field. The difference between the magnetic fields is perpendicular to the direction of the current density.

the perpendicular polarization  $\mathbf{E} \parallel Oy$  is called “crossed” and its amplitudes are marked by  $\perp$ . The fields on the sides of the slab are related by the transfer matrix (2.6):

$$\begin{aligned}
 X(0) &= 1 \begin{pmatrix} 1 \\ 0 \\ 0 \\ 1 \end{pmatrix} e^{i(k_0 \times 0)} + r_{\parallel} \begin{pmatrix} 1 \\ 0 \\ 0 \\ -1 \end{pmatrix} e^{i(-k_0 \times 0)} + r_{\perp} \begin{pmatrix} 0 \\ 1 \\ 1 \\ 0 \end{pmatrix} e^{i(-k_0 \times 0)}, \\
 X(d) &= t_{\parallel} \begin{pmatrix} 1 \\ 0 \\ 0 \\ 1 \end{pmatrix} e^{ik_0 d} + t_{\perp} \begin{pmatrix} 0 \\ 1 \\ -1 \\ 0 \end{pmatrix} e^{ik_0 d}, \\
 X(d) &= D(d)X(0).
 \end{aligned} \tag{2.7}$$

Relation (2.7) is a system of four linear equations with respect to four complex amplitudes of reflection and transmission  $r_{\parallel}$ ,  $r_{\perp}$ ,  $t_{\parallel}$ ,  $t_{\perp}$ . By solving the linear system, one can obtain a well-known expression for the transmission through the dielectric slab:

$$t_{\parallel} = \frac{\exp(-i\frac{\omega}{c}d)}{\cos(\sqrt{\varepsilon}\frac{\omega}{c}d) - \frac{i}{2}(\sqrt{\varepsilon} + \frac{1}{\sqrt{\varepsilon}})\sin(\sqrt{\varepsilon}\frac{\omega}{c}d)}. \tag{2.8}$$

Note that the same coordinate system for incident and transmitted waves is used in this work. As a result, a layer of vacuum of thickness  $d$  produces no phase shift and has  $t_{\parallel} = 1$ .

At a given frequency  $\omega$  a metallic medium with the tensor of complex conductivity  $\hat{\sigma}$  is mathematically equivalent to a dielectric medium with the dielectric permittivity

$$\hat{\varepsilon} = I + \frac{4\pi i}{\omega} \hat{\sigma},$$



where  $I$  is an identity matrix. Assume that the thickness  $d$  is small enough and the following conditions are satisfied:

$$\frac{\omega}{c}d \ll 1; \quad d \ll \frac{c}{\sqrt{2\pi\sigma\omega}}.$$

The first condition means that the film thickness should be much smaller than the wavelength of the radiation in vacuum. The second condition requires that the film thickness is also much smaller than the skin-depth in the metallic medium, so the field can be treated as approximately uniform inside the film. Suppose the tensor of conductivity in the chosen coordinate system is given by

$$\hat{\sigma} = \begin{pmatrix} \sigma_{xx} & \sigma_{xy} & 0 \\ \sigma_{yx} & \sigma_{yy} & 0 \\ 0 & 0 & \sigma_{zz} \end{pmatrix}.$$

Then, following the procedure, described above, one can obtain a transfer matrix for the thin conducting film:

$$F = \begin{pmatrix} 1 & 0 & 0 & 0 \\ 0 & 1 & 0 & 0 \\ \frac{4\pi}{c}\sigma_{yx}d & \frac{4\pi}{c}\sigma_{yy}d & 1 & 0 \\ -\frac{4\pi}{c}\sigma_{xx}d & -\frac{4\pi}{c}\sigma_{xy}d & 0 & 1 \end{pmatrix}. \quad (2.9)$$

In a less strict way, the transfer matrix  $F$  can be obtained by a simple physical reasoning, using Fig. 2.1(b). If the film is thin enough, then the tangential components of the electric field are equal on both sides of the film. Therefore in the case of the normal incidence the electric field can be treated as uniform across the film thickness. The electric field creates a current density  $\mathbf{j} = \hat{\sigma}\mathbf{E}$ , which leads to a jump in the tangential magnetic field, equal to  $\frac{4\pi}{c}jd$  and perpendicular to the direction of the current. Writing down these relations in a matrix form, one obtains the transfer matrix (2.9).

Some of the samples, studied in this work, were grown in a form of a thin conducting film on top of an insulating dielectric slab. In order to find the transmission coefficients through such a sample, one has to solve a system of linear equations, similar to (2.7):

$$X(a) = D(a)FX(0), \quad (2.10)$$

where  $a$  is the thickness of the dielectric substrate. In an external magnetic field, perpendicular to the film (Faraday geometry), the components of the conductivity tensor are connected as  $\sigma_{xx} = \sigma_{yy}$ ,  $\sigma_{xy} = -\sigma_{yx}$ . In this case the solution for the system (2.10) is:

$$t_{\parallel} = \frac{2a_{xx}e^{-\imath\frac{\omega}{c}a}}{a_{xx}^2 + a_{xy}^2}; \quad t_{\perp} = \frac{2a_{xy}e^{-\imath\frac{\omega}{c}a}}{a_{xx}^2 + a_{xy}^2}, \quad (2.11)$$

where

$$\beta = \sqrt{\varepsilon}\frac{\omega}{c}a; \\ a_{xx} = (1 + \frac{4\pi}{c}\sigma_{xx}d)(\cos \beta - \frac{\imath}{\sqrt{\varepsilon}}\sin \beta) + \cos \beta - \imath\sqrt{\varepsilon}\sin \beta; \quad (2.12)$$

$$a_{xy} = \frac{4\pi}{c} \sigma_{xy} d (\cos \beta - \frac{i}{\sqrt{\varepsilon}} \sin \beta). \quad (2.13)$$

In spectroscopic experiments the quantities  $t_{\parallel}$  and  $t_{\perp}$  are obtained as complex numbers. Equations (2.11) can be inverted to produce the explicit expressions for the diagonal and off-diagonal complex conductivities:

$$\sigma_{xx} = \frac{c\sqrt{\varepsilon}e^{-i\frac{\omega}{c}a}t_{\parallel}}{2\pi d(t_{\parallel}^2 + t_{\perp}^2)(\sqrt{\varepsilon}\cos\beta - i\sin\beta)} - c\frac{2\sqrt{\varepsilon}\cos\beta - i(1+\varepsilon)\sin\beta}{4\pi d(\sqrt{\varepsilon}\cos\beta - i\sin\beta)}; \quad (2.14)$$

$$\sigma_{xy} = \frac{c\sqrt{\varepsilon}e^{-i\frac{\omega}{c}a}t_{\perp}}{2\pi d(t_{\parallel}^2 + t_{\perp}^2)(\sqrt{\varepsilon}\cos\beta - i\sin\beta)}, \quad (2.15)$$

where  $a$  is the substrate thickness,  $\varepsilon$  is the dielectric permittivity of the substrate,  $d$  is the film thickness,  $\omega = 2\pi f$  is the angular frequency of the radiation,  $\beta = \sqrt{\varepsilon}\frac{\omega}{c}a$ .

## 2.2 Continuous wave sub-THz spectroscopy

The most part of experimental data in this work has been obtained with the use of the far-infrared spectroscopy. This frequency range lies between the microwaves and the mid-IR radiation. From the experimental point of view, the mid-IR radiation is very similar to the visible light, from which it differs by its wavelength only. At microwave frequencies the wavelength in vacuum is comparable to the size of elements of an experimental setup ( $\approx 5$  mm and larger), so the radiation cannot be effectively controlled by means of lenses and mirrors. Experimental techniques at microwaves widely use waveguides for continuous frequency measurements and resonators for discrete frequencies. Spectroscopic experiments in the far-IR (terahertz, sub-millimeter) range can be conducted in a way that is similar to the optical techniques. Collimated beams of the radiation travel in open space and can be controlled by lenses and mirrors. Due to the comparatively large wavelength, the far-IR beams diverge much faster, than the optical ones. The border, where the quasi-optical technique becomes inapplicable, depends on the size of investigated samples and on the requirements for the experimental setup. In case of the samples, that can be grown arbitrary large (more than  $1 \text{ cm}^2$  in cross-section), such measurements can be extended down to  $1 \text{ cm}^{-1}$  in open space. Measurements in a magnet with optical windows on samples of a smaller size (several  $\text{mm}^2$ ) can give unreliable results already below  $4 \text{ cm}^{-1}$ .

### 2.2.1 Mach-Zehnder interferometer

Backward wave oscillators (BWOs) generate monochromatic radiation, which frequency can be adjusted by changing an applied voltage. Principle of operation of a BWO is based on an electron beam, traveling along a periodic grid that plays a role of a slow-wave structure. Interaction of the electrons with the periodic electric field of the grid leads to the generation of radiation, which frequency is determined by the speed of the electrons and the period of the grid. The speed of the electrons is controlled by the accelerating voltage, which allows to sweep the generated frequency continuously in a certain range. Several lamps cover the

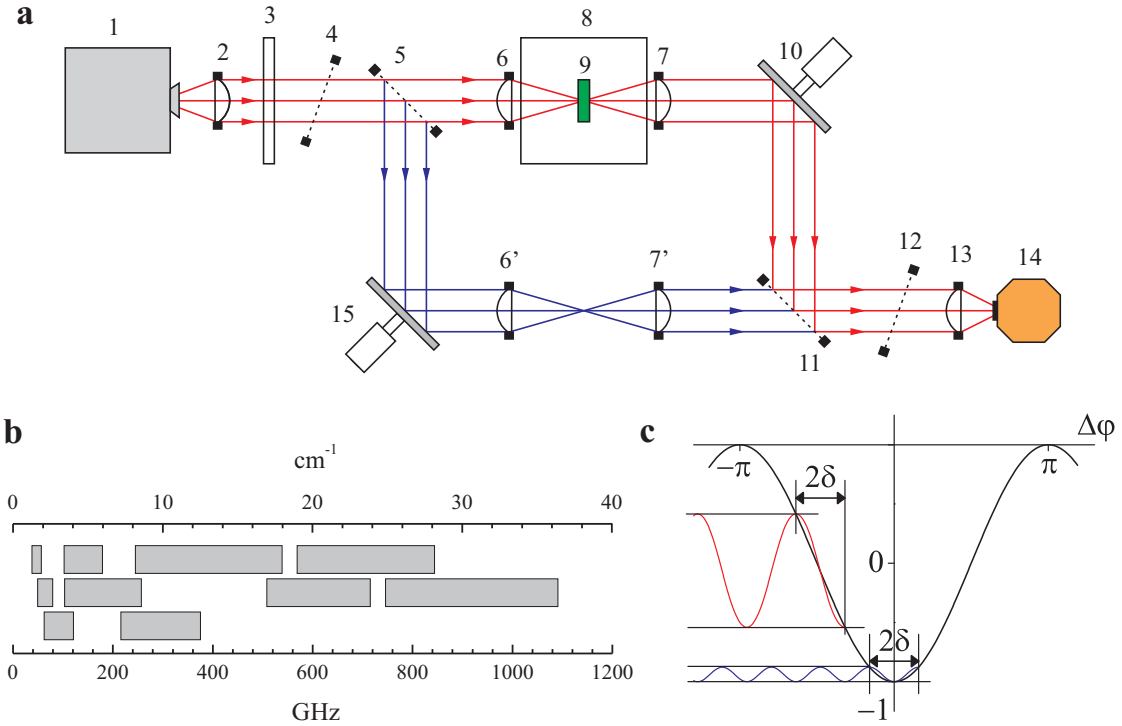


**Figure 2.2:** Quasi-optical Mach-Zehnder spectrometer. (a) Scheme of spectrometer. 1 – radiation source (BWO); 2 – source focusing lens; 3 – mechanical interrupting chopper; 4 – grid polarizer; 5 – beam splitter; 6, 6', 7, 7' – focusing lenses; 10 – movable mirror; 11, 12 – grid polarizers; 13 – detector focusing lens; 14 – detector; 15 – modulating mirror. (b) Working frequency ranges of the backward wave oscillators. (c) Illustration for the phase measurement algorithm. The sample and reference beams of the spectrometer are merged together by polarizer 11 and interfere after polarizer 12. The intensity of the resulting signal depends on the phase difference  $\Delta\varphi$  between the beams as shown by the black curve. Modulating mirror 15 causes oscillations of the intensity around a point, set by the position of motorized mirror 10. When the beams are in balance ( $\Delta\varphi = 0$ ), then the period of the intensity oscillations becomes twice smaller (blue curve) compared to the off-balance case (red curve).

band 38 GHz–1.1 THz, as shown in Fig. 2.2(b). Maximal radiation power of 25 mW can be achieved in low-frequency BWOs, while for high-frequency BWOs the typical generated power is below 1 mW.

At frequencies below 1 THz the radiation beams can be easily modified using dielectric lenses with spherical surfaces. In order to minimize signal losses and avoid undesirable reflections, the lens material must have low absorption and a low refracting index. The optimal combination of these properties is achieved in lenses made of teflon or polyethylene.

Figure 2.2(a) shows a scheme of a Mach-Zehnder interferometer, in which BWO (1) is used as a source of radiation. A focusing lens (2) converts a diverging wave into a quasi-parallel beam. A grid polarizer (5), acting as a beam splitter, splits the light into two beams with orthogonal linear polarizations. In transmission mode only the sample beam, depicted by the red color, is used. The reference beam is interrupted by a non-reflecting opaque flap and the motorized mirror (10) is fixed. In this mode a mechanical chopper (3) is used to modulate the radiation, coming from BWO, to discriminate it from the heat background, caused by nearby

room-temperature objects. The chopper is supplied with a photo-sensor that generates electric pulses on each interruption by the blades. Lenses (6) and (7) focus the beam on a sample and restore a parallel beam. The intensity of the beam, passed through the sample stage, is measured by a sensitive He-cooled bolometer (14), which converts the intensity into a voltage. The amplitude of the voltage modulation is measured by a custom lock-in amplifier, which uses the pulses from the photo-sensor on the chopper as a reference signal. Measurements of the transmission amplitude  $|t|$  consist of two steps. The intensity of the passing light is measured with a sample (9) and without the sample. The ratio of the intensities gives a squared absolute value  $|t|^2$  of the complex transmission amplitude.

In a phase measurement mode both beams are open and the chopper is removed. The initial wave is split by the grid polarizer (5). The component, which electric field is parallel to the grid wires, is reflected into the reference beam, while the component with electric field perpendicular to the wires passes through and form the sample beam. Since the waves in the two beams have orthogonal linear polarizations, they add without interference after the grid (11) and form an elliptically polarized wave. The grid (12) lets pass a linear wave, allowing the corresponding components from the sample and reference beams to interfere. The intensity, measured by the detector can be calculated as

$$I = |E_{\text{sam}}e^{i\varphi_{\text{sam}}} - E_{\text{ref}}e^{i\varphi_{\text{ref}}}|^2 = |E_{\text{sam}}|^2 + |E_{\text{ref}}|^2 - 2E_{\text{sam}}E_{\text{ref}}\cos(\varphi_{\text{sam}} - \varphi_{\text{ref}}). \quad (2.16)$$

Here  $Ee^{i\varphi}$  is a complex amplitude of the linearly polarized wave, passed through the sample or the reference beam and the final polarizer (12). By rotating the polarizer to an adjacent quadrant, one can add  $\pi$  to  $\varphi_{\text{sam}}$  or  $\varphi_{\text{ref}}$  and choose between addition and subtraction of the complex amplitudes. In order to minimize the intensity, measured by the detector when the two optical paths are equal, the final polarizer must be adjusted to subtraction of the beams, therefore the “-” sign is assumed in Eq. (2.16).

The motorized mirror (10) allows to change the optical length of the sample beam and adjust the phase  $\varphi_{\text{sam}}$  to make it equal to  $\varphi_{\text{ref}}$ . According to Eq. (2.16), if  $\Delta\varphi = \varphi_{\text{sam}} - \varphi_{\text{ref}} = 2\pi m$ , where  $m$  is an integer number, then the intensity  $I$  reaches its minimum. Therefore, the phases can be made equal up to  $2\pi m$  by finding such a position of the motorized mirror, at which a minimum in intensity  $I$  is achieved. As it will be explained below, the order  $m$  of the minimum does not affect the value of the obtained complex transmission.

From technical point of view, finding the position, at which  $\Delta\varphi = 2\pi m$  and the intensity is minimal, is performed in the following way, see Fig. 2.2(c). The modulating mirror (15) oscillates at the frequency  $\Omega \approx 28$  Hz, introducing an oscillating term in the phase difference:

$$\begin{aligned} I(t) &= \text{const} - 2E_{\text{sam}}E_{\text{ref}}\cos(\Delta\varphi + \delta \sin \Omega t) = \\ &= \text{const} - 2E_{\text{sam}}E_{\text{ref}}\cos(\Delta\varphi)\cos(\delta \sin \Omega t) + \\ &\quad + 2E_{\text{sam}}E_{\text{ref}}\sin(\Delta\varphi)\sin(\delta \sin \Omega t). \end{aligned} \quad (2.17)$$

Here  $\delta < \pi/2$  is an amplitude of the phase modulation, connected to the amplitude  $a$  of the mechanical motion of the mirror through

$$\delta = \frac{\omega a}{c}.$$

The first time-dependent term in Eq. (2.17) is proportional to  $\cos \Delta\varphi$ . It has a twice smaller period, than the oscillating mirror, as it follows from

$$\cos\left(\delta \sin \Omega\left(t + \frac{2\pi}{2\Omega}\right)\right) = \cos(\delta \sin \Omega t).$$

Therefore, in the Fourier representation this term produces only even harmonics with the frequencies  $2\Omega$ ,  $4\Omega$ ,  $6\Omega$ , etc. The first harmonic at frequency  $1\Omega$  is only produced by the second time-dependent term, which is proportional to  $\sin \Delta\varphi$ . A digital acquisition unit (DAU) measures the signal from the detector as a function of time and calculates the amplitude of the first harmonic. Depending on a sign of the amplitude, the motorized mirror is shifted in the appropriate direction to achieve zero amplitude of the first harmonic and satisfy  $\Delta\varphi = 0$ . The mirror position is measured with a sample ( $l_{\text{sam}}$ ) and without it ( $l_0$ ). The complex phase of the transmission coefficient  $t = |t|e^{i\varphi}$  is calculated as

$$\varphi = \omega \frac{l_{\text{sam}} - l_0}{c}. \quad (2.18)$$

When the motorized mirror satisfies the condition  $\Delta\varphi = 0$ , the amplitude of the second harmonic  $2\Omega$  is determined by the amplitudes  $E_{\text{sam}}$ ,  $E_{\text{ref}}$  and the modulation amplitude  $\delta$ , as it can be seen from Eq. (2.17). Since  $E_{\text{ref}}$  and  $\delta$  remain constant, the amplitude of the second harmonic can be used to obtain the absolute value  $|t|$  of the complex transmission amplitude. Using this technique allows to obtain both the absolute value and the complex phase in one measurement (with a sample and a calibration without it), with no need in conducting two separate experiments. There is no mathematical requirements for the oscillating phase amplitude  $\delta$  to be small. Since the amplitude of the second harmonic is proportional to  $\delta^2$ , the amplitude of the oscillating mirror should be set as large as possible, as long as the algorithm is stable. The optimal value for the phase modulation is assumed to be around  $\delta = \pi/3$ , which corresponds to the mirror amplitude  $a = \lambda/6$ , one sixth of the radiation wavelength.

As it can be seen from Eq. (2.18), an addition of  $m\lambda$  to the mirror position leads to the change in the measured phase difference by  $2\pi m$ . In this consideration we neglected those effects that are connected with a spreading of the beams and other imperfections. In this approximation, the same complex transmission value is obtained, regardless which order  $m$  is used. However, in dielectric measurements it is useful to find the zero-order position, at which the optical paths in the sample and the reference beams are exactly equal. Mathematically, different values of the complex dielectric permittivity  $\varepsilon$  can lead to the same complex transmission. For example, as it can be seen from Eq. (2.8), at frequency  $\omega = 2\pi c/d$  any material with a dielectric constant  $\varepsilon = n^2$ , where  $n$  is an integer, will cause no effect on the incident wave ( $t_{\parallel} = 1$ ). In this case one needs additional information for choosing the right value. Determination of the zero-order position with a sample and without it allows to calculate the optical path difference, caused by the sample, and to estimate the value of permittivity from the approximate relation:

$$(\sqrt{\text{Re}(\varepsilon)} - 1)d = l_{\text{sam}} - l_0.$$

With no sample in the beam, the position of the zeroth order can be easily determined, as it does not depend on the radiation frequency  $\omega$ . The same is valid for a sample in the beam, if the dispersion of the dielectric permittivity is small.

### 2.2.2 Field distribution between focusing lenses

Experimental data, obtained by means of the quasi-optical submillimeter spectroscopy, are used to calculate such important material properties as complex permittivity, magnetic permeability, magnetoelectric permittivity, high-frequency conductivity. It is a common practice to use equations, analogous to (2.8, 2.15), that were derived for the case of an infinite slab and the normal incidence of a plane wave. In fact, in real spectroscopic experiments electromagnetic radiation with a typical wavelength of 1 mm is collimated into  $\approx 5$  cm diameter beams. High quality samples are extremely difficult to grow, and for this reason their cross-section usually does not exceed several square millimeters. In order to measure transmission through such a small sample, the beam is focused with the aid of convex lenses. The distribution of the electromagnetic fields between the lenses can be, in principle, explored with a use of a movable scanning detector. Alternatively, the field pattern can be numerically calculated, using the finite element or finite difference methods. In the treated frequency range the wavelengths are comparable with the dimensions of the optical elements, which allows to solve the Maxwell equations explicitly, using a reasonable amount of nodes ( $10^6$ ).

Figure 2.3 shows the distribution of intensity of the high-frequency electric field between the focusing lenses, calculated with the use of the finite element method. All quantities in the calculation do not depend on  $y$ -direction, which corresponds to infinitely long cylindric lenses, an infinitely long diaphragm, etc. In other words, a two-dimensional problem has been solved instead of a three-dimensional, in order to decrease the number of nodes by several orders and speed up the calculation. The symmetry of the model allows to reduce the calculations to one half, since the field is symmetric with respect to the optical axis. The model setup includes two lenses with the dielectric constant  $\varepsilon_{\text{lens}} = 2.25$ . One of the surfaces is flat and the second is cylindric with the curvature radius  $r_{\text{lens}} = 50$  mm. Each lens is placed into an absorbing diaphragm with material parameters  $\varepsilon_{\text{abs}} = \mu_{\text{abs}} = 1 + 50i$ . Such equality of the permittivity and magnetic permeability leads to zero reflection at normal incidence, while the large imaginary parts cause a fast attenuation of electromagnetic waves in this medium. The dimensions of the model are  $100 \times 300$  mm<sup>2</sup>. A border condition on the edges, represented by green color in Fig. 2.3(a) was set to simulate an incident plane wave with the wave vector directed along  $z$ -axis. The polarization of this wave is linear with the electric field parallel to  $y$ -axis. Due to the symmetry with respect to the optical axis, shown by red dashed line,  $z$ -component of the magnetic field is zero on the optical axis. Therefore, a corresponding border condition was set for the nodes on this edge. Finally, a border condition simulating radiation with the absence of reflection was set on the borders, shown by magenta color. An additional absorbing diaphragm collimates the incident plane wave into a 66 mm wide beam. Figures 2.3(b, d) show the distribution of the electric field magnitude at frequencies 120 and 30 GHz respectively. The absolute value of the electric field is coded by color, as shown on the right scale. The amplitude of the incident wave is taken to be 1. While the distribution at 120 GHz is qualitatively similar to the picture that can be expected from the laws of geometric optics, the distribution at 30 GHz demonstrates significant deviations. The plots show that this case is hard to be treated rigorously analytically, since the field intensity changes fast in  $x$ -direction and the paraxial approximation is not valid. Nevertheless, even in these conditions the simulated transmission through a dielectric slab, see Fig. 2.3(c), is well

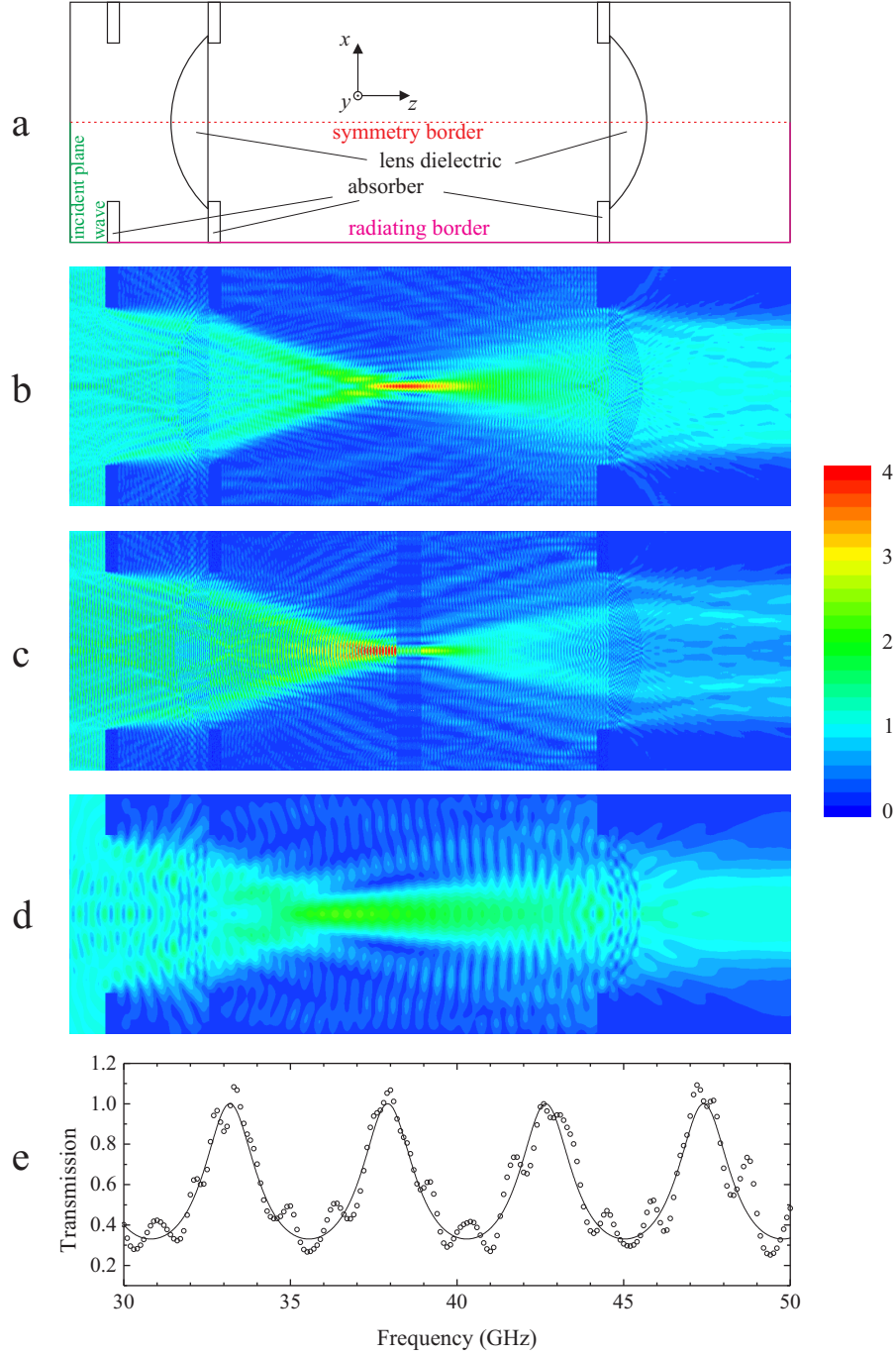


**Figure 2.3:** Two-dimensional finite element simulation of the distribution of the electric field between the focusing lenses. a) Scheme of the simulation. b) The distribution of the electric field at frequency 120 GHz. The absolute value of the high-frequency electric field is coded by colors as shown on the right. The amplitude of the incident plane wave is taken to be 1. c) Same as (b) with addition of an dielectric slab with  $\varepsilon = 10$  as a sample. d) Distribution of the electric field at frequency 30 GHz. e) Transmission, obtained from the simulation (squares), in comparison with the theoretical calculation (solid line).

described by Eq. (2.8). The high-frequency quasi-periodic deviations (standing waves), which can be observed in the spectrum plot, are caused by reflections between the optical elements. Their origin is treated below in details. In experiment, if the investigated material is available in the form of large slabs, then it is possible to measure the transmission with the lenses and without them. Both methods give the same results for the transmission coefficient. This fact justifies, to some extent, the usage of the theory, developed for the plane waves and infinite samples.

### 2.2.3 Standing waves in spectra

The simulated spectrum in Fig. 2.3(e) demonstrates quasi-periodic deviations from the theoretical curve. Such deviations usually present in experimentally obtained spectra as well. They are caused by re-reflections between the sample and other elements of the experimental setup (lenses, mylar windows, etc). The theoretical expressions, derived for a sample in free space, do not allow for these reflections. Using matrix formalism, presented in section 2.1, it is not difficult to reproduce these parasitic oscillations analytically. The real experimental setup can be represented by the matrix

$$M_{\text{setup}} = M_1 M_2 \dots M_n,$$

where matrices  $M_i$  correspond to the elements of the setup,  $M_n$  being the closest element to the source and  $M_1$  being the closest element to the detector. The coefficients of complex transmission and reflection of this system can be found by solving the linear system

$$M_{\text{setup}} \begin{pmatrix} 1 + r_{\parallel} \\ r_{\perp} \\ r_{\perp} \\ 1 - r_{\parallel} \end{pmatrix} = e^{i \frac{\omega}{c} z_{\text{setup}}} \begin{pmatrix} t_{\parallel} \\ t_{\perp} \\ -t_{\perp} \\ t_{\parallel} \end{pmatrix}, \quad (2.19)$$

where  $\omega$  is the angular frequency of radiation,  $z_{\text{setup}}$  is the distance between the initial and final surfaces of the setup. Optical windows, having a form of a dielectric slab with a thickness  $d$  and dielectric constant  $\varepsilon$ , can be represented by the matrix

$$M_{\text{diel}}(\varepsilon, d) = \begin{pmatrix} \cos \alpha & 0 & 0 & \frac{i}{\sqrt{\varepsilon}} \sin \alpha \\ 0 & \cos \alpha & -\frac{i}{\sqrt{\varepsilon}} \sin \alpha & 0 \\ 0 & -i\sqrt{\varepsilon} \sin \alpha & \cos \alpha & 0 \\ i\sqrt{\varepsilon} \sin \alpha & 0 & 0 & \cos \alpha \end{pmatrix}, \quad (2.20)$$

where  $\alpha = \sqrt{\varepsilon} \frac{\omega}{c} d$ . Elements, separated by a distance  $d$ , should be connected by the corresponding matrix

$$M_{\text{air}}(d) = M_{\text{diel}}(1, d).$$

In a very rough approximation, the focusing lenses can be approximated by a dielectric slab with some effective thickness and permittivity. More generally, an arbitrary element with given complex amplitudes  $r_{\parallel} = r$ ,  $t_{\parallel} = t$ ,  $r_{\perp} = t_{\perp} = 0$  can be represented by the transfer



matrix

$$M_{\text{custom}}(t, r) = \frac{1}{2t} \begin{pmatrix} t^2 + 1 - r^2 & 0 & 0 & t^2 - (1 + r)^2 \\ 0 & t^2 + 1 - r^2 & -t^2 + (1 + r)^2 & 0 \\ 0 & -t^2 + (1 - r)^2 & t^2 + 1 - r^2 & 0 \\ t^2 - (1 - r)^2 & 0 & 0 & t^2 + 1 - r^2 \end{pmatrix}. \quad (2.21)$$

The matrix (2.21) describes an isotropic optical element with zero thickness, which reflection and transmission do not depend on the polarization and the direction of the beam. The matrix can be obtained by applying this conditions to Eq. (2.19) and a complementary one for the opposite direction of light. The parameters  $r$  and  $t$  can be functions of frequency. By analogy, one can derive matrices for anisotropic elements, polarization rotators, etc. However, one should be careful while using such matrices for modeling, as an arbitrary set of chosen parameters can give unexpected results. For example, the matrix (2.21) with  $t = -r = 1/\sqrt{2}$  seems to describe a nonabsorbing element that reflects half the radiation power and transmits the other half. A Fabry-Pérot interferometer, consisting of two such elements separated by a distance  $d$ , is described by the transfer matrix

$$M_{\text{setup}} = M_{\text{custom}}\left(\frac{1}{\sqrt{2}}, -\frac{1}{\sqrt{2}}\right) M_{\text{air}}(d) M_{\text{custom}}\left(\frac{1}{\sqrt{2}}, -\frac{1}{\sqrt{2}}\right)$$

By solving Eq. (2.19), one obtains the reflection of such interferometer  $|r_{\text{F-P}}|^2 = 2$  at frequencies  $\omega = \pi n c/d$ , where  $n$  is an integer number. The “nonabsorbing element” proves to generate energy, if placed near the same element, the generation power being dependent on the distance between the elements. The necessary restrictions on  $r$  and  $t$  for a realistic nonabsorbing element can be established by a treatment of the energy balance. Assume waves with amplitudes  $a$  and  $b$  come to the element from the opposite sides. Then the balance between the energies that come and leave the element requires

$$|a|^2 + |b|^2 = |ra + tb|^2 + |ta + rb|^2 = (|r|^2 + |t|^2)(|a|^2 + |b|^2) + (t^*r + r^*t)(a^*b + b^*a).$$

This equality should be valid for arbitrary  $a$  and  $b$ , which leads to

$$|t|^2 + |r|^2 = 1; \quad r^*t + t^*r = 0, \quad (2.22)$$

or equivalently

$$|t|^2 + |r|^2 = 1; \quad \arg t - \arg r = \pm \frac{\pi}{2}.$$

The last expression shows that in the lossless case not only the absolute values of the amplitudes are connected, but also their complex phases. Another restriction comes from the continuity of tangential components of the electric field:

$$1 + r = t. \quad (2.23)$$

The equality is valid for an infinitely thin optical element. By combining (2.22) and (2.23), we conclude that any thin nonabsorbing optical element is determined by a single free parameter  $\varphi$ :

$$t = \frac{1 + e^{i\varphi}}{2}; \quad r = \frac{-1 + e^{i\varphi}}{2}. \quad (2.24)$$

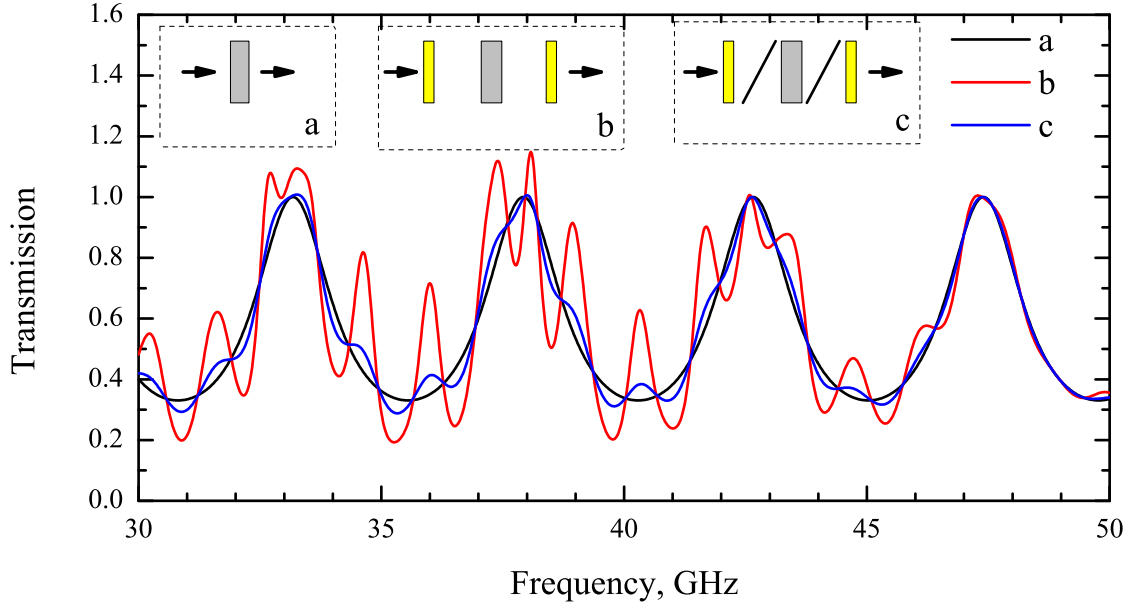


**Figure 2.4:** Frequency-dependent transmission, calculated in terms of the matrix formalism. (a) Infinite dielectric sample in free space (black curve). (b) The same sample between two dielectric slabs (red curve). Although their reflection is small, the slabs cause significant deviation from the spectrum (a). (c) Addition of non-reflecting attenuators reduces the deviation from the initial spectrum (blue curve).

Standing waves can cause significant experimental problems, as they affect both measured transmission amplitude and phase. A simple model setup, reproducing the emergence of the standing waves, is represented by the transfer matrix

$$M_1 = M_{\text{diel}}(\varepsilon_w, d_w) M_{\text{air}}(d) M_{\text{sample}} M_{\text{air}}(d) M_{\text{diel}}(\varepsilon_w, d_w).$$

Here  $M_{\text{diel}}(\varepsilon_w, d_w)$  stands for a dielectric slab with  $d_w = 0.5$  cm,  $\varepsilon_w = 1.5$ , separated by distance  $d = 10$  cm from a sample. In a very rough approximation these slabs simulate the focusing lenses in Fig. 2.3. The sample in the form of a dielectric slab with  $d_s = 1.0$  cm,  $\varepsilon_s = 10$  is represented by the corresponding matrix  $M_{\text{sample}} = M_{\text{diel}}(10, 1)$ . In order to simulate a real experiment, results of the measurement with the sample in the beam should be determined from equation (2.19) with  $M_{\text{setup}} = M_1$ ,  $z_{\text{setup}} = 2d_w + 2d + d_s$ . The reference measurement is obtained from (2.19) with the transfer matrix

$$M_{\text{setup}} = M_{\text{diel}}(\varepsilon_w, d_w) M_{\text{air}}(d) M_{\text{air}}(d_{\text{sample}}) M_{\text{air}}(d) M_{\text{diel}}(\varepsilon_w, d_w),$$

where the transfer matrix of the sample is replaced by a matrix for the layer of vacuum of the same thickness. In order to decrease the standing waves, the real lenses are made of materials with the dielectric constant as close to 1 as possible. In our model setup the slabs with  $\varepsilon_w = 1.5$  reflect up to 4% of the incident energy. This small reflection results in the periodic deviations, see Fig. 2.4. The black curve shows the transmission, calculated by using Eq. (2.8) for a sample in free space. The same result is obtained by setting  $\varepsilon_w = 1$  in the calculation. The period of the oscillations is close to  $c/(2\pi d)$ , where  $d$  is the distance between

the sample and the lenses, but this is an approximate expression. In this case the estimation is accurate up to 10%. Note that the periods of the standing waves are very close in Figs. 2.3(e) and 2.4.

The standing waves can be suppressed by putting absorbing non-reflecting elements between the sample and the focusing lenses. An important requirement here is the absence of reflections. Practically, it can be achieved by using a tilted sheet of some absorber. Due to the tilt, the reflected wave leaves the optical path, which is equal to the absence of any reflection. The blue curve in Fig. 2.4 shows the measured transmission, if the introduced elements are described by  $M_{\text{custom}}(r, t)$  with  $r = 0$  and  $t = 1/2$ . In this case the amplitude of the standing waves decreases approximately in  $1/|t|^2 = 4$  times. Thus, if the radiation source is powerful enough, the effect of the standing waves can be minimized. However this method is difficult to realize in experiments with the optical magnet. In the optical magnet the main contribution to the amplitude of the standing waves is supposed to come from the inner optical windows, separated by a distance of  $\approx 20$  mm from the sample. In order to suppress the reflections, the tilted absorbers should be introduced between the sample and the windows. The sample volume is small and its surfaces are made of metal. For this reason, the wave reflected by the absorber partially returns to the initial optical path, making the procedure less effective.

## 2.2.4 Standing waves in magnetic field scans

When the transmission coefficient is measured as a function of frequency, the standing waves reveal as the distinct oscillations. The period of the oscillations is determined by the distance between the optical elements. If the setup consists of several elements, separated by different distances, the periodic patterns add to form a noise-like picture. However, the measurements are reproducible, so the “noise” is not a random error.

In opposite to this, measurements of the transmission as a function of the external magnetic field at a fixed frequency produce curves that are free of such oscillations. The same is usually valid for any swept parameter, other than the frequency, like temperature or gate voltage. The effect of the standing waves in this case can be treated in the framework of the matrix formalism, just like it was done in the previous subsection. While the previous consideration was devoted to the setup, suitable for the finite-element calculation, here we will treat a setup, modeling more realistic experimental conditions. We consider a model sample that corresponds to the GaAs/AlGaAs heterojunction C0456, see chapter 5. In terms of the model it is a dielectric slab with the dielectric constant  $\varepsilon = 11.65$  and thickness  $d = 0.66$  mm. One of the surfaces of the slab is covered by an infinitely thin conducting film with the Drude conductivity tensor:

$$\begin{aligned}\sigma_{xx} = \sigma_{yy} &= \sigma_0 \frac{1 - i\omega\tau}{(1 - i\omega\tau)^2 + (\Omega_c\tau)^2}; \\ \sigma_{xy} = -\sigma_{yx} &= \sigma_0 \frac{\Omega_c\tau}{(1 - i\omega\tau)^2 + (\Omega_c\tau)^2}; \\ \Omega_c &= \frac{eB}{mc},\end{aligned}$$

where  $m = 0.07m_0$  is an effective electron mass,  $\tau = 4$  ps is an electron relaxation time and  $\sigma_0 = ne^2\tau/m = 1.3 \times c/(4\pi)$  is a static Drude conductivity that is proportional to the electron density  $n$ . This thin film represents the two-dimensional electron gas, formed in the heterojunction. The corresponding matrix is given by

$$M_{\text{film}} = \begin{pmatrix} 1 & 0 & 0 & 0 \\ 0 & 1 & 0 & 0 \\ -\frac{4\pi}{c}\sigma_{xy} & \frac{4\pi}{c}\sigma_{xx} & 1 & 0 \\ -\frac{4\pi}{c}\sigma_{xx} & -\frac{4\pi}{c}\sigma_{xy} & 0 & 1 \end{pmatrix}.$$

In order to model the Mylar optical windows, we put two additional slabs with  $\varepsilon = 2$  and  $d = 50$   $\mu\text{m}$ , separated from the sample by  $L = 25$  mm. The actual dielectric constant of Mylar is close to 3, but this value results in too high reflection. The value, used in the calculations, was reduced to 2, because the windows are not plane parallel and only a part of the reflected wave returns into the beam. Upper panels in Fig. 2.5 show the calculated transmission coefficient through a single window with these parameters. The left panel shows the full range 0–1200 GHz and the right panel shows a more narrow range 400–450 GHz. The reflection coefficient of the single window is equal to  $(1 - |t|^2)$  and for the frequency range of the right panels it is close to 4%.

We can find the “experimental” transmission coefficients  $t_{\parallel}^{\text{exp}}(\omega, B)$  and  $t_{\perp}^{\text{exp}}(\omega, B)$  for this setup by solving Eq. (2.19) with

$$M_{\text{setup}} = M_{\text{diel}}(2, 5 \cdot 10^{-3})M_{\text{air}}(2.5)M_{\text{diel}}(11.65, 0.066)M_{\text{film}}M_{\text{air}}(2.5)M_{\text{diel}}(2, 5 \cdot 10^{-3});$$

$$z_{\text{setup}} = 2 \times (5 \cdot 10^{-3} + 2.5) + 0.066 = 5.076.$$

In order to simulate a typical experimental field scan at a fixed frequency  $\omega$ , we calculate  $t_{\parallel}^{\text{exp}}(\omega, B_k)$  and  $t_{\perp}^{\text{exp}}(\omega, B_k)$  for 201 equidistant points  $B_k$  in the range 0–4 T. Then we fit these data by minimizing the residual

$$\sum_{k=0}^{200} \left( \left| t_{\parallel}^{\text{exp}}(\omega, B_k) - a_{\parallel} t_{\parallel}^{\text{th}}(\omega, B_k) \right|^2 + \left| t_{\perp}^{\text{exp}}(\omega, B_k) - a_{\perp} t_{\perp}^{\text{th}}(\omega, B_k) \right|^2 \right). \quad (2.25)$$

The “theoretical” coefficients  $t^{\text{th}}$  are calculated using Eq. (2.11) for the sample in free space (adapted for the 2D case by removing the film thickness). Two complex coefficients  $a_{\parallel, \perp}$  can be varied along with the Drude parameters ( $\sigma_0, \tau, m$ ) to minimize the residual (2.25). The results of the simulation in the frequency range 0–1200 GHz are shown in Fig. 2.5.

Figures 2.5(b, b’) show the parallel spectrum in zero magnetic field. The red curve is the transmission through the sample in free space. As the reflection coefficient of the Mylar windows increases with the frequency, the amplitude of the standing waves also increases. The period of the oscillations is close to 5 GHz, which is close to their period in the experimental spectra, see Figs. (4.4(e), 5.6). However the amplitude of the standing waves does not grow with the frequency in experiments. The real optical windows have an irregular shape, and probably for this reason the frequency dependence of the amplitude differs from our model.

Figures 2.5(c, c’) show the residual fitting error as a function of frequency. The error periodically crosses zero, which means that the fitting curve perfectly matches the simulated

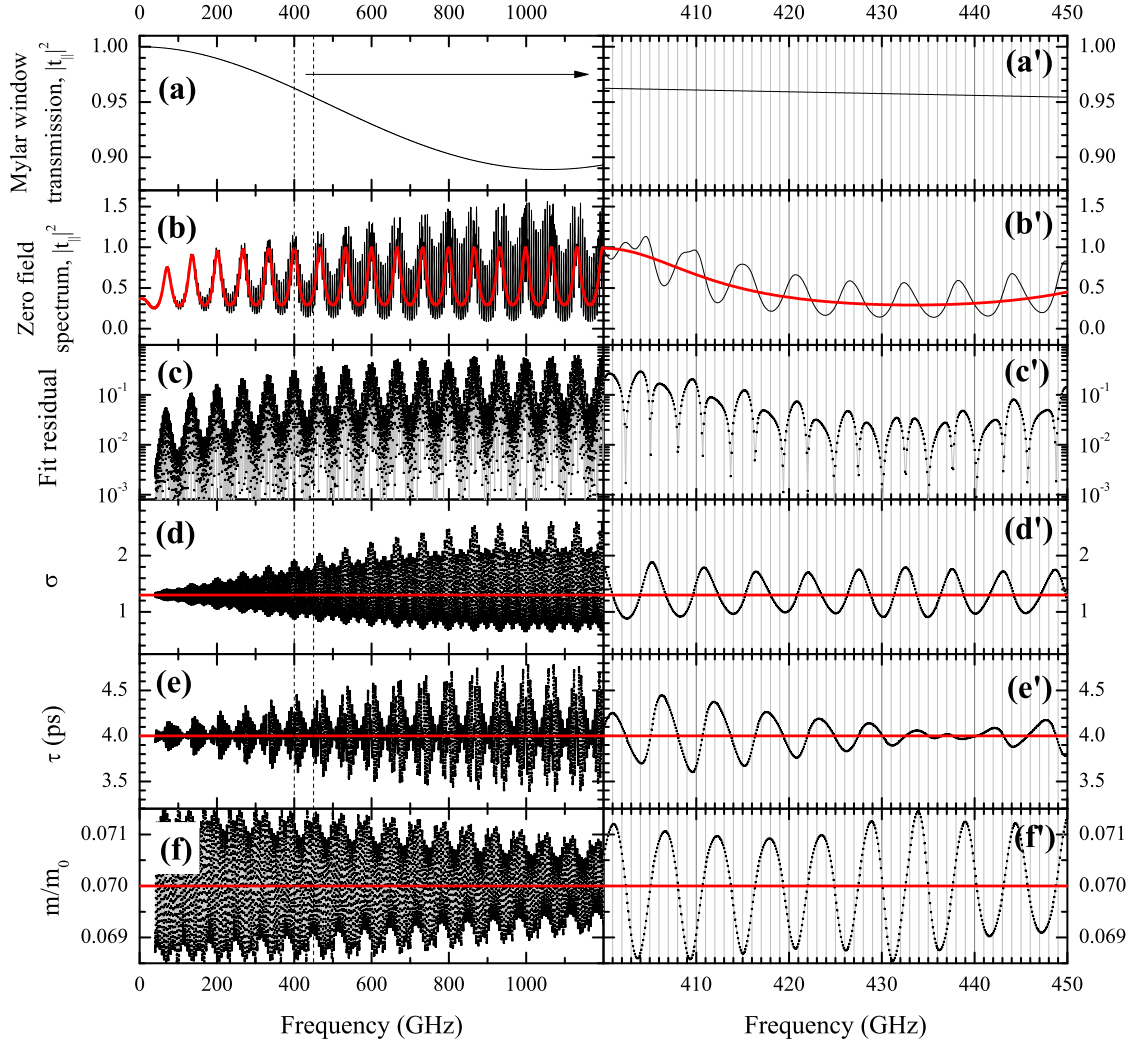


**Figure 2.5:** Effect of Mylar optical windows on the transmission measurements of a GaAs/AlGaAs heterojunction, calculated using the matrix formalism. Left panels show the full frequency range 0–1200 GHz and right panels show the range 400–450 GHz. (a, a') Parallel transmission through a single Mylar window. (b, b') Parallel transmission through the sample in free space (red) and through the sample between two optical windows (black). (c, c') Residual error (2.25) as a function of the frequency. (d, d'–f, f') Drude parameters obtained from the fit of magnetic scans at fixed frequencies (black). Red lines show the values, used in the simulation.

data at these points. When the fit is perfect, the Drude parameters  $\tau$  and  $m$  are equal to the “true” relaxation time and the mass. However parameter  $\sigma_0$  at these points is never correct, see Figs. 2.5(c’–f’). In the fitting procedure we assume implicitly, that the effect of the standing waves can be described by a simple multiplication by the complex coefficients  $a$ . The analysis of this model show that the amplitude of the cyclotron peak in magnetic scans is distorted differently from the off-resonance transmission level. The distortion cannot be “corrected” by the simple multiplication. Instead, the Drude parameter  $\sigma_0$  deviates from its correct value to change the resonance amplitude and to decrease the residual error. Parameter  $\sigma_0$  turns out to be the most sensitive to the standing waves. The 4% reflection of the window can cause 40% error in the estimation of  $\sigma_0$ , while the error for  $m$  and  $\tau$  in this case is about 10%.

To conclude, the effect of the standing waves on magnetic scans has been considered in the framework of the simple matrix model. Although the parasitic reflections do not reveal as oscillations in the magnetic scans, they do affect the experimental transmission. This distortion can cause significant errors in the estimated model parameters. If the accurate measurement of this parameters is the goal of the study, then the effect of the standing waves must be either suppressed, either be taken into account during the data treatment.

### 2.2.5 Signal stability at fixed frequency

At fixed frequency, transmission coefficients are measured as a function of some external parameter applied to a sample: temperature, magnetic or electric field, gate voltage, lighting etc. Experimental accuracy of such scans strongly depends on stability of the signal. Ideally, any change in the transmission should be only caused by some change in properties of the sample. In fact, even measurements without any sample usually demonstrate signal dependence on the swept parameter, and taking into account these deviations can be a challenging task. The main reasons of this unwanted phenomenon are mechanical instability of the optical elements and instability of the radiation source. In this chapter we will treat solutions that were implemented to compensate changes in generated radiation power of backward-wave oscillators.

Operation of BWO is based on an electron beam, passing near a periodic slow-wave structure. While the frequency of radiation, generated by BWO, smoothly depends on the accelerating voltage, the dependence of the power has numerous points of discontinuity and a large oscillating derivative. A strong magnet in BWO serves as a focusing device for the electron beam. During magnetic measurements BWO is placed in proximity of another strong superconducting optical magnet on a distance of  $\approx 1.5$  m. The magnetic field, induced by the superconducting coil on a large distance from it can be approximated by the field of a magnetic dipole. The field magnitude decreases as  $1/r^3$  and reaches several Gauss at the position of BWO. Although the enclosure of BWO has magnetic screening properties, sweeping of the external magnetic field leads to a change in the generated power. Increase of the magnetic field from 0 to 7 T can cause up to 30% change in the signal, the change being dependent on the generation frequency. High frequency BWOs typically show a more pronounced dependence on the external magnetic field.

A natural solution of this problem would be a movement of the source to a large distance from the magnet. However the optical table has only limited dimensions. Moreover, increas-

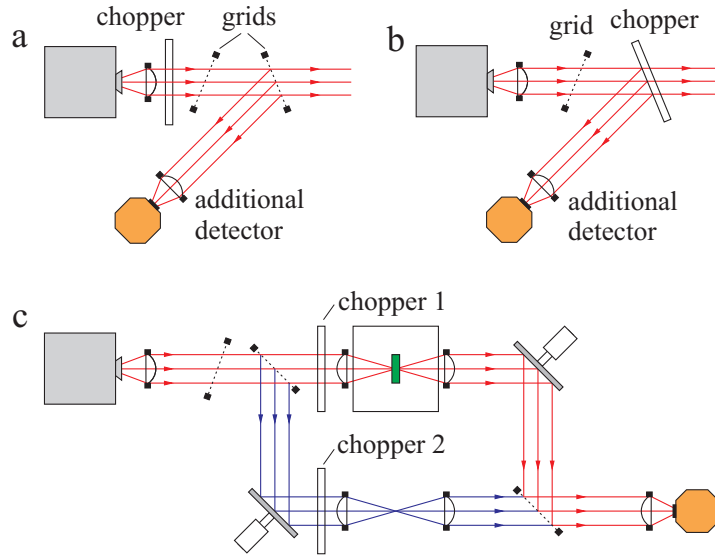


**Figure 2.6:** Measurement of the BWO generation power simultaneously with the transmission through the sample. a) Using an additional detector to measure radiation intensity right at the BWO's output. The second polarizer redirects a part of initial beam into the additional detector, while the first polarizer is necessary for the split beams to have proportional intensities. b) Same as (a), but with a mechanical chopper instead of the grid polarizer for the redirection, in order to suppress effects of sample reflection on the additional detector. c) Measurement of intensities of two beams, using one detector. The beams are modulated by mechanical choppers with different frequencies, allowing to extract corresponding harmonic amplitudes during the signal processing. In opposite to the setup in Fig. 2.2(a), the final grid analyzer is removed, since the beams must not interfere.

ing of the optical path leads to signal spread losses, which can be critical while using low-power high frequency sources. Another way is to cancel the external magnetic field by using a passive magnetic screening or an active compensating coil. However BWO's enclosure itself has magnetic screening properties and the simple addition of another screening box would be not efficient. The active compensation requires an adjustment of the proportional coefficient between the magnetic fields of the optical magnet and the current in the compensating coil. Because of a field inhomogeneity, this coefficient might be dependent on the generated frequency. None of the three methods corrects the changes in the generated power, that are not connected with the external magnetic field. They can occur due to various reasons like a change of environment temperature, a change of a cooling water flow, etc.

A separate measurement of the BWO signal without a sample as a function of magnetic field can be used to remove the dependence of generated power. This procedure doubles the time, required for experiments and the consumption of cryogenic liquids. Just as the methods, described above, it does not correct the irreproducible jumps of the power. Measurement of the BWO signal simultaneously with the transmission through the sample solves both problems. If an additional far-IR detector is available, this can be done simply by a redirection of a part of the initial beam into the second controlling detector, see Fig. 2.6(a, b). In this case the first polarizer plays a very important role, since the linear orthogonal components of the generated elliptical wave can have different dependencies on time or magnetic field. The factory digital acquisition unit (DAU) has two separate ports to connect IR bolometer and Golay cell as detectors. Unfortunately, only one of the detectors can be used at once. The signal from

the second detector must be measured using an additional lock-in amplifier. An alternative method, described below in details, requires only one detector to obtain the intensities of two beams.

Just like in the phase measurement mode, the initial beam is split into two beams with orthogonal linear polarizations, see Fig. 2.6(c). In opposite to the setup in Fig. 2.2(a), two separate mechanical interrupting choppers are placed into the beams. The choppers have significantly different frequencies. In the realized setup one chopper was hardware stabilized at the frequency 22.7 Hz, while the second one had the frequency around 98 Hz with no active stabilization. Joined together by the second beamsplitter, the beams come to the detector almost with no interference, since the polarizer, that makes them interfere in the phase measurement mode, is removed. The IR detector converts the radiation intensity into a voltage and the output of the detector is connected to the DAU input port. Here the DAU is used as an amplifier and a low-pass filter. The voltage from the DAU analog output is digitized by a National Instruments NI-6351 board at a 50 kHz sample rate with a 16-bit resolution. In very early preliminary experiments a PC AC'97 was used for this purpose. The amplitudes of the harmonics are extracted numerically, as described in the next section.

### 2.2.6 Measuring two signals with one detector

Calculation of a harmonic amplitude is mathematically straightforward for a function  $f(t)$  defined on the whole real axis. If  $f(t)$  is “good enough”, it can be represented as

$$f_t(t) = \int_{-\infty}^{+\infty} f_\omega(\omega) \frac{e^{-i\omega t}}{\sqrt{2\pi}} d\omega, \quad (2.26)$$

where

$$f_\omega(\omega) = \int_{-\infty}^{+\infty} f_t(t) \frac{e^{i\omega t}}{\sqrt{2\pi}} dt. \quad (2.27)$$

Function  $f$  can be treated as a vector, which is represented by  $f_t$  in a time “basis” and by  $f_\omega$  in a frequency basis. Formulas 2.26, 2.27, commonly recognized as inverse and direct Fourier transform, have a form of a scalar product of a vector  $f$  with basis vectors. Base vectors of the frequency basis have a form of exponential functions in the time basis and vice versa. Any exponential function  $\phi$  has a property

$$\phi(x + y) = \phi(x)\phi(y),$$

which leads to a very important consequence, known as a convolution theorem. Suppose a vector is represented by a product of two functions  $f_t(t)g_t(t)$  in the time basis. Then in the frequency basis the vector will have a form

$$\int_{-\infty}^{+\infty} f_t(t)g_t(t) \frac{e^{i\omega t}}{\sqrt{2\pi}} dt =$$



$$\begin{aligned}
&= \int_{-\infty}^{+\infty} f_t(t) \frac{e^{i\omega t}}{\sqrt{2\pi}} \int_{-\infty}^{+\infty} g_\omega(\xi) \frac{e^{-i\xi t}}{\sqrt{2\pi}} d\xi dt = \frac{1}{\sqrt{2\pi}} \int_{-\infty}^{+\infty} f_t(t) \frac{e^{i(\omega-\xi)t}}{\sqrt{2\pi}} \int_{-\infty}^{+\infty} g_\omega(\xi) d\xi dt = \\
&= \frac{1}{\sqrt{2\pi}} \int_{-\infty}^{+\infty} f_\omega(\omega - \xi) g_\omega(\xi) d\xi.
\end{aligned}$$

The last expression is a convolution of representations  $f_\omega$  and  $g_\omega$  in the frequency basis (or, equivalent, Fourier transforms of  $f_t$  and  $g_t$ ). Thus, multiplication in the time basis corresponds to convolution in the frequency basis. In the same way one can show that multiplication in the frequency basis corresponds to convolution in the time basis.

Operation of convolution  $h = f * g$ , mathematically defined by an integral or a sum expression, allows a simple intuitive interpretation. One of the functions, say  $f$ , can be treated as “initial”, and the convolution results in a new function  $h$ . A value of  $h$  at a given point is equal to a sum of (generally, all) values of  $f$  with weight coefficients, defined by the function  $g$ . If  $g(t)$  is negligibly small for large  $|t|$ , then the value of  $h$  at a given point is defined only by values of  $f$  in the adjacent points, and if  $g$  is positive,  $h(t)$  can be viewed as a weighted average of neighbour values  $f$ . In this case operation of convolution can be imagined as a smoothing or a blur. In fact, the blur effect in raster image processing is realized by a convolution with some function (for example, two-dimensional Gaussian). Another example is a smoothing of a sampled function by taking a simple average of several neighbour values, which is equivalent to a convolution with a rectangular function.

In the experimental setup, depicted in Fig. 2.6(c), the initial nonmodulated beam from the BWO source is split into two beams by a grid polarizer. Each of the beams is modulated by a separate mechanical chopper. The beams are joined by another grid without interference, so that the detected intensity is a simple sum of two signals to be measured. Fig. 2.7(c) shows a model signal

$$f(t) = \sin(2\pi f_1 t) + \sin(2\pi f_2 t), \quad (2.28)$$

consisting of two pure sine harmonics with frequencies  $f_1 = 22.75$  and  $f_2 = 97$  Hz. If we treat the signal on the infinite interval  $-\infty < t < +\infty$ , then its spectrum is a sum of four delta functions:

$$f_\omega(\omega) = i\sqrt{\frac{\pi}{2}} [-\delta(\omega_1 + \omega) + \delta(\omega_1 - \omega) - \delta(\omega_2 + \omega) + \delta(\omega_2 - \omega)], \quad (2.29)$$

where  $\omega_i = 2\pi f_i$ . In the real experimental setup the choppers do not produce a sine harmonic. Instead, they create a periodic signal, containing all corresponding multiple frequencies  $f$ ,  $2f$ ,  $3f$ , etc. In addition, if a chopper consists of several blades, that are not perfectly equal, it will also create subharmonics. In a real experiment one has to adjust frequencies to avoid overlapping of a chopper frequency with (sub)harmonics of the other chopper. For illustrative purposes, the model signal has only two harmonics.

The time interval  $\tau = 0.74$  s in Fig. 2.7(c) is close to a typical measurement time. Measuring the signal  $f_t(t)$  within a finite period of time  $\tau$  is mathematically equivalent to a multi-

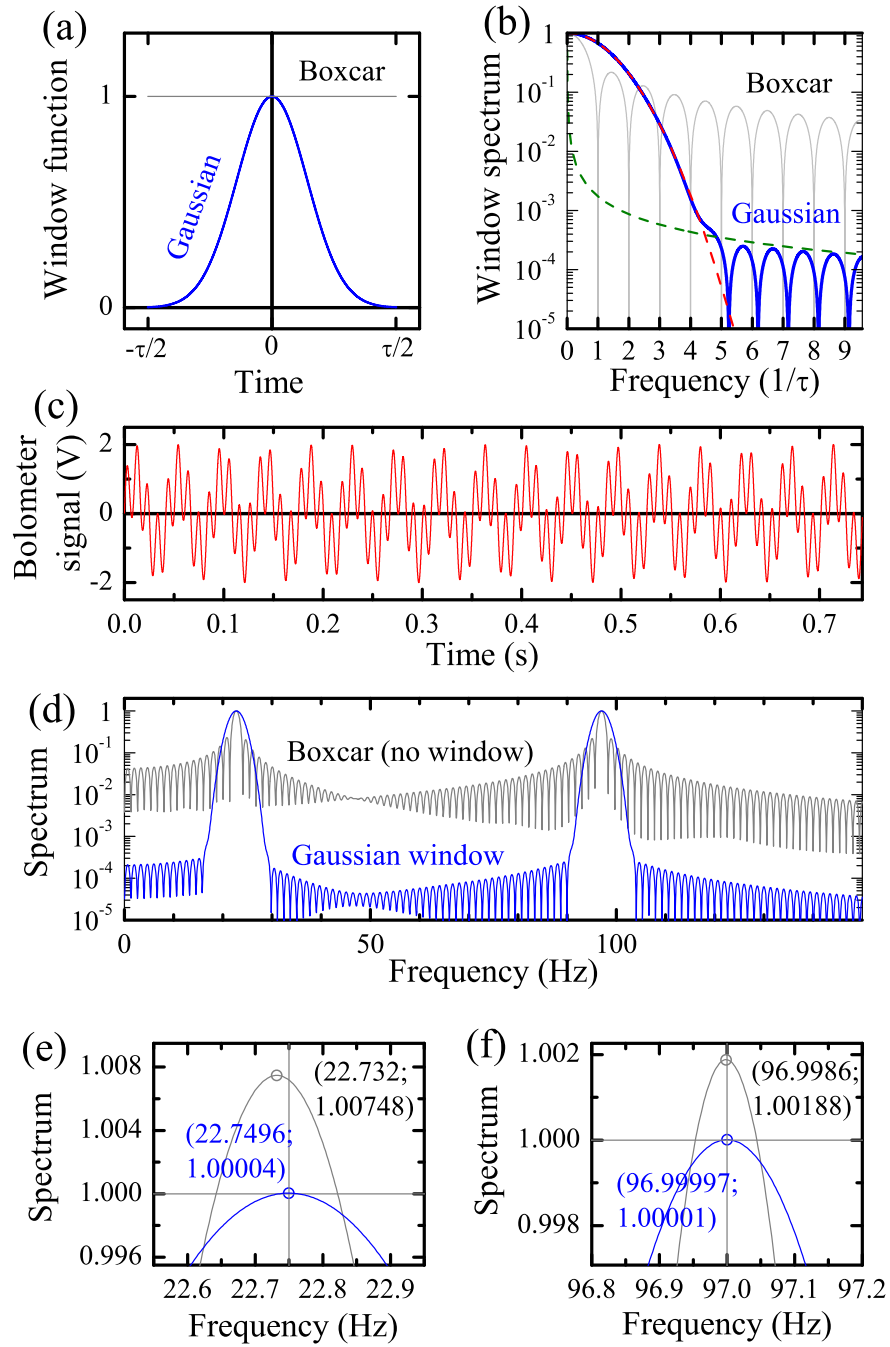


**Figure 2.7:** Extraction of amplitudes of harmonics at two different frequencies. Boxcar and Gaussian window functions are shown in the time representation (a) and in the frequency representation (b). (c) - model noiseless signal, consisting of two sine harmonics at 22.75 and 97 Hz with amplitude 1 each. (d) - spectrum of initial signal (gray) and the signal, multiplied by the Gaussian window (blue). (e,f) - zoom in on the peaks at 22.75 and 97 Hz. Peak positions and amplitudes, shown in brackets, demonstrate an increase of accuracy, caused by the windowing.

plication by a boxcar window function, shown in Fig. 2.7(a):

$$g_t(t) = \begin{cases} 1 & \text{if } |t| \leq \tau/2; \\ 0 & \text{if } |t| > \tau/2. \end{cases}$$

The spectrum of the boxcar function

$$g_\omega(\omega) = \frac{\tau}{\sqrt{2\pi}} \frac{\sin(\omega\tau/2)}{\omega\tau/2} = \frac{\tau}{\sqrt{2\pi}} \text{sinc}(\omega\tau/2).$$

is a well-known in signal processing sinc function. A normalized plot of the sinc function is shown in Fig. 2.7(b) on a logarithmic scale. Due to the points of discontinuity at  $t = \pm\tau/2$ , the spectrum decreases very slowly with frequency as  $1/\omega$ . According to the convolution theorem, the spectrum  $f_\omega$  of the signal (2.29) is convolved with the spectrum  $g_\omega$  of the window function. A convolution of a smooth function  $g(\omega)$  with a delta function  $\delta(\omega_0 - \omega)$

$$\int_{-\infty}^{+\infty} g(\omega - \xi) \delta(\omega_0 - \xi) d\xi = g(\omega - \omega_0) \quad (2.30)$$

results in the function  $g$ , shifted to  $\omega_0$ . Since the spectrum (2.29) of the infinite signal consists of four delta functions, the spectrum of the confined signal is a sum of four sinc functions, centered at  $\pm f_{1,2}$ , as shown in Fig. 2.7(d) by a gray curve. Because of the slow decreasing of the sinc function, the peak amplitude at any  $f_i$  is affected by the tails of the peaks at other frequencies. Figures 2.7(e, f) show the spectrum of the confined signal near the frequencies  $f_{1,2}$ . The absolute value is normalized to give a unit amplitude for a single harmonic. The deviation from  $|f_\omega(\omega_{1,2})| = 1$ , as expected for the model signal (2.28), is caused by the tails of other peaks. The relative error in the amplitude is comparable with resonance absorption of some samples with a low electron density. Therefore, the straightforward calculation of a Fourier amplitude on a finite interval does not provide the necessary accuracy.

The problem can be solved by using an appropriate window function  $g(t)$ . Instead of  $f(t)$  we will analyse a windowed signal  $h(t) = f(t)g(t)$ . By definition, the window function is taken to be zero outside the interval  $-\tau/2 \leq t \leq \tau/2$ , so the values of  $f(t)$  outside the interval are not needed for the calculation. According to the convolution theorem and (2.30), every harmonic  $e^{i\omega_0 t}$  in the infinite signal  $f(t)$  produces a peak in the spectrum  $h_\omega(\omega)$ . This peak is centered at  $\omega_0$  and its shape is given by the absolute value of the window spectrum  $g_\omega(\omega)$ . We want the value of  $h_\omega(\omega_0)$  to be solely proportional to  $f_\omega(\omega_0)$  and not affected by other harmonics. For this purpose, the absolute value  $|g_\omega|$  must be negligibly small for  $|\omega| \geq \Delta\omega$ , where  $\Delta\omega$  is the minimal difference between adjacent harmonics in  $f(t)$ . According to the uncertainty principle, since  $g(t)$  is zero outside the interval  $|t| \leq \tau/2$ , its spectral width  $\delta\omega$  cannot be smaller, than  $\sim \tau^{-1}$ . Generally, the uncertainty principle holds for any function  $g$ :

$$\delta t^2 \delta \omega^2 = \int_{-\infty}^{+\infty} t^2 |g_t(t)|^2 dt \times \int_{-\infty}^{+\infty} \omega^2 |g_\omega(\omega)|^2 d\omega \geq \frac{1}{4}. \quad (2.31)$$

The strict equality here is attained if  $g$  is a Gaussian function:

$$g(t) = \exp\left(-\frac{t^2}{2\sigma^2}\right).$$

Its Fourier transform

$$g_\omega(\omega) = \sigma \exp\left(-\frac{\sigma^2\omega^2}{2}\right)$$

is again a Gaussian. Since the spectrum decreases extremely fast, let us construct a window on this base. For this purpose, we replace the values by zeros outside the finite interval:

$$g_t(t) = \begin{cases} \exp\left(-\frac{t^2}{2\sigma^2}\right) & \text{if } |t| \leq \tau/2; \\ 0 & \text{if } |t| > \tau/2. \end{cases} \quad (2.32)$$

Figures 2.7(a, b) show the window function (2.32) in the time and frequency representations with the parameter  $\sigma = \tau/(5\sqrt{2}) \approx \tau/7$ . In the low-frequency domain  $|g_\omega|$  is close to a Gaussian. On the logarithmic scale in Fig. 2.7(b) this asymptotic behavior is shown by a red dashed parabola. The truncation leads to the discontinuous steps at  $\pm\tau/2$  of height  $\approx 2 \times 10^{-3}$ . Due to the steps the high-frequency tail rolls off as  $\propto \omega^{-1}$ , as shown by a green curve in Fig. 2.7(b). However the proportional coefficient is significantly reduced in comparison with the boxcar window. Figures 2.7(e, f) show the peaks in  $h_\omega$  for the boxcar (gray) and the Gaussian (blue) windows. The use of the Gaussian window allows to improve the measurement accuracy of the peak amplitudes and frequencies. By adjusting the parameter  $\sigma$  one can trade off between the level of the high-frequency lobes and the width of the central peak in  $|g_\omega|$ . In contrast to the model signal (2.28) with a discrete spectrum, the bolometer signal contains a random noise  $\delta f(t)$  with a broadband spectrum  $\delta f_\omega(\omega)$ . In some approximation, the noise simply adds to the useful signal  $f(t)$ . The error in the amplitude, caused by this noise, is given by

$$\delta h_\omega = \int_{-\infty}^{+\infty} \delta f(t) g(t) \frac{e^{i\omega t}}{\sqrt{2\pi}} dt = \frac{1}{\sqrt{2\pi}} \int_{-\infty}^{+\infty} \delta f_\omega(\omega - \xi) g_\omega(\xi) d\xi.$$

In the continuous case  $\delta f_\omega$  is a very abstract object. In the numerical calculations all the integrals are replaced by corresponding sums, so let us replace the integration by a sum over discrete frequencies  $\xi_k = k\Delta\xi$ , where  $\Delta\xi$  is small:

$$\delta h_\omega = \frac{1}{\sqrt{2\pi}} \sum_{k=-\infty}^{+\infty} \delta f_\omega(\omega - \xi_k) g_\omega(\xi_k) \Delta\xi.$$

If we assume that the noise is white, then  $\delta f_\omega(\omega - \xi_k)$  are random complex variables. Their real and imaginary parts are normally distributed with a zero mean value. If  $\sigma \ll \tau$ , then the window function  $g_\omega$  effectively limits the summation by the interval  $\xi \lesssim \sigma^{-1}$ . Therefore,  $\delta h_\omega$  is a sum of  $N \propto 1/\sigma$  random variables with the same distributions, and we can write:

$$|\delta h_\omega|^2 \propto 1/\sigma. \quad (2.33)$$

A small value of  $\sigma$  produces a window that is narrow in the time representation. According to (2.33), this case is characterized by an increase of the error, caused by the random broadband noise. At the same time, the level of the high-frequency lobes in  $g_\omega$  decreases, which is favorable for the separation of strong discrete harmonics in  $f(t)$ . In the opposite limit of large  $\sigma$  we obtain the boxcar window. The boxcar window is optimal for filtering out the broadband noise, but it is unsuitable for the separation of strong discrete harmonics. The intermediate value of  $\sigma = 5\sqrt{2}$  was found to be optimal in the experiments.

As mentioned above, the low-frequency part of  $\log |g_\omega(\omega)|$  is very close to a parabola. This feature of the Gaussian window can be useful for a real-time processing algorithm. If the approximate position of the peak is known, one can numerically calculate  $h_\omega$  at three close frequencies. For instance, the values can be obtained directly from a fast discrete Fourier transform. The three pairs  $(f, \log |h_\omega|)$  define a parabola, which maximum determines a new approximation of the peak frequency. Then one of the initial pair is replaced by the new one to make an iterative algorithm. If the initial triplet lies within the peak width, the method converges after one or two iterations. The presented approach has been used in measurements of the cyclotron resonance in HgTe/CdHgTe quantum wells, see section 4.3.



## 3 Two-dimensional electron gas in magnetic field

### 3.1 One-electron Drude model

In this chapter we treat electron properties of a two-dimensional system in an external magnetic field. A detailed consideration of three-dimensional systems can be found in Refs. [17, 18]. We will calculate the conductivity tensor in two ways that are based on the same assumption about relaxation processes. First, we adopt a totally phenomenological classical approach, based on Newtonian mechanics. After that we will treat a slightly more rigorous statistical consideration, involving the Boltzmann equation and the semi-classical band theory. The second method allows to establish connections between the band structure and the phenomenological quantities of the first approach.

The first approach was first suggested by Drude [19, 20] soon after Thomson's discovery of the electron. We apply this method to a two-dimensional electron gas in an external uniform magnetic field. Each electron is treated as a classical particle with the mass  $m$  and the charge  $e$ . The mechanical motion is confined by some external forces in the plane  $z = 0$ . The external uniform magnetic field is directed along  $z$ -axis, perpendicular to the  $xy$ -plane. We assume that a linearly polarized monochromatic electromagnetic wave of angular frequency  $\omega$  is incident on the gas. The wave has the wave vector directed along  $z$ -axis. Thus the harmonically oscillating electric field  $\mathbf{E}_{\text{ext}}e^{-i\omega t}$  of this wave is the same in each point of the  $xy$ -plane. The equation of motion for an electron with the position vector  $\mathbf{r}(t)$  takes the form:

$$m\ddot{\mathbf{r}} = e(\mathbf{E}_{\text{ext}}e^{-i\omega t} + \mathbf{E}_{\text{self}} + \frac{1}{c}\dot{\mathbf{r}} \times \mathbf{B}) - \frac{m}{\tau}\dot{\mathbf{r}}. \quad (3.1)$$

The first term on the right side is the Lorentz force. It includes the constant field  $\mathbf{B}$  and the harmonic electric field  $\mathbf{E}_{\text{ext}}e^{-i\omega t}$ . The term  $\mathbf{E}_{\text{self}}$  is the electric field, induced by all other electrons. We neglect the interaction of the electron with the non-static magnetic field, since

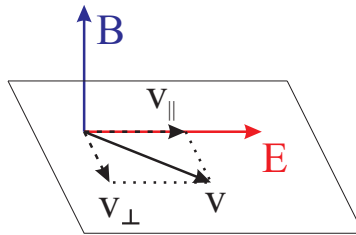


**Figure 3.1:** Two-dimensional electron gas in external magnetic field.

it is by orders of magnitude weaker, than other forces. The term  $-m\dot{\mathbf{r}}/\tau$  introduces a viscous friction force to allow for the scattering. In the absence of any fields ( $E_{ext} = E_{self} = B = 0$ ) the motion would exponentially decay as  $\dot{\mathbf{r}}_0 e^{-t/\tau}$ .

Differential equation (3.1) describes the motion of the electron for any initial conditions at  $t = 0$ . Its solution can be represented as  $\mathbf{r}(t) = \mathbf{r}_p(t) + \mathbf{r}_h(t)$ , where  $\mathbf{r}_p(t)$  is a particular solution for Eq. (3.1) and  $\mathbf{r}_h(t)$  is a solution for the homogeneous equation with no driving force:

$$m\ddot{\mathbf{r}} = e(\mathbf{E}_{self} + \frac{1}{c}\dot{\mathbf{r}} \times \mathbf{B}) - \frac{m}{\tau}\dot{\mathbf{r}}. \quad (3.2)$$

Homogeneous equation (3.2) describes a transient motion of the electron. Because of the dissipation, the transient processes decay and at  $t \gg \tau$  the motion of electrons is described by the particular solution:  $\mathbf{r}(t) = \mathbf{r}_p(t)$ . We try to find the particular solution in the form  $\dot{\mathbf{r}} = \mathbf{v}e^{-i\omega t}$ , where  $\mathbf{v}$  is a constant complex vector. Then the electric field  $\mathbf{E}_{self}$ , induced by other electrons, also oscillates harmonically and for the total electric field we can write  $\mathbf{E}_{ext}e^{-i\omega t} + \mathbf{E}_{self} = \mathbf{E}e^{-i\omega t}$ , where  $\mathbf{E}$  is a constant vector. By substituting  $\dot{\mathbf{r}} = \mathbf{v}e^{-i\omega t}$  in Eq. (3.1) we obtain:

$$(-i\omega + \frac{1}{\tau})\mathbf{v} - \frac{e}{mc}\mathbf{v} \times \mathbf{B} = \frac{e}{m}\mathbf{E}. \quad (3.3)$$

The vector  $\mathbf{v}$  can be expressed as a linear combination of vectors  $\mathbf{e}_{\parallel} \parallel \mathbf{E}$  and  $\mathbf{e}_{\perp} \perp \mathbf{E}$ :

$$\mathbf{v} = \mathbf{v}_{\parallel} + \mathbf{v}_{\perp} = v_{\parallel}\mathbf{e}_{\parallel} + v_{\perp}\mathbf{e}_{\perp}. \quad (3.4)$$

By substituting (3.4) in Eq. (3.3) we obtain the system of linear equations:

$$\begin{cases} (\frac{1}{\tau} - i\omega)v_{\parallel} + \Omega v_{\perp} = \frac{eE}{m}; \\ (\frac{1}{\tau} - i\omega)v_{\perp} - \Omega v_{\parallel} = 0, \end{cases} \quad (3.5)$$

where  $\Omega = eB/(mc)$  is a cyclotron frequency. The coefficients  $v_{\parallel}$ ,  $v_{\perp}$  and the vector  $\mathbf{v}$  can be obtained directly from Eq. (3.5). We are interested in the two-dimensional current density  $\mathbf{j}$ . It is connected to the velocity as  $\mathbf{j} = en\mathbf{v}$ , where  $n$  is a two-dimensional density of electrons. Using the values for  $v_{\parallel}$ ,  $v_{\perp}$ , we obtain the linear relation between the vectors of the electric field and the current density:

$$\begin{aligned} j_{\parallel} &= \sigma_{xx}E; & \sigma_{xx} &= \sigma_0 \frac{1 - i\omega\tau}{(1 - i\omega\tau)^2 + (\Omega\tau)^2}; \\ j_{\perp} &= \sigma_{xy}E; & \sigma_{xy} &= \sigma_0 \frac{\Omega\tau}{(1 - i\omega\tau)^2 + (\Omega\tau)^2}, \end{aligned} \quad (3.6)$$

where  $\sigma_0 = ne^2\tau/m$  is the static conductivity at  $B = 0$ . The choice of the indexes comes from the form of the relation  $\mathbf{j} = \hat{\sigma}\mathbf{E}$  in an arbitrary coordinate system in the  $xy$ -plane:

$$\mathbf{j} = \mathbf{j}_{\parallel} + \mathbf{j}_{\perp} = \sigma_{xx} \begin{pmatrix} 1 & 0 \\ 0 & 1 \end{pmatrix} \begin{pmatrix} E_x \\ E_y \end{pmatrix} + \sigma_{xy} \begin{pmatrix} 0 & 1 \\ -1 & 0 \end{pmatrix} \begin{pmatrix} E_x \\ E_y \end{pmatrix} = \begin{pmatrix} \sigma_{xx} & \sigma_{xy} \\ -\sigma_{xy} & \sigma_{xx} \end{pmatrix} \begin{pmatrix} E_x \\ E_y \end{pmatrix}.$$



Although Eqs. (3.6) are obtained in terms of the very simple one-particle model, they keep their form in a more strict consideration, which is discussed in the next section.

### 3.2 Boltzmann equation. Cyclotron mass

In section 3.1 the electrons were treated as classical particles with a parabolic energy spectrum  $\varepsilon(\mathbf{k}) = \hbar^2 \mathbf{k}^2 / (2m)$ . This approach can be modified in order to describe electronic properties of metals and semiconductors. Electrons are viewed as semi-classical quasiparticles that can be characterized by its position vector  $\mathbf{r}$  and its wave vector  $\mathbf{k}$  simultaneously [21]. The wave vector plays a role of an effective momentum of the electron in the crystal:

$$\hbar \dot{\mathbf{k}} = e(\mathbf{E}e^{-i\omega t} + \frac{1}{c} \mathbf{v} \times \mathbf{B}). \quad (3.7)$$

The effect of the crystal on the dynamic properties of the electron is contained in the energy spectrum  $\varepsilon(\mathbf{k})$  that is no longer given by the simple parabolic dependence. The velocity  $\mathbf{v} = \dot{\mathbf{r}}$  in Eq. (3.7) is connected to the spectrum as

$$\mathbf{v} = \frac{1}{\hbar} \frac{\partial \varepsilon(\mathbf{k})}{\partial \mathbf{k}}. \quad (3.8)$$

Later in this section we will assume that the energy  $\varepsilon$  depends on the absolute value of the wave vector  $k = |\mathbf{k}| = \sqrt{k_x^2 + k_y^2}$  only:

$$\varepsilon = \varepsilon(k). \quad (3.9)$$

In this case the band structure is represented by a surface of revolution in  $(k_x, k_y, \varepsilon)$  space and the velocity takes the form

$$\mathbf{v} = \frac{1}{\hbar} \varepsilon' \frac{\mathbf{k}}{k}. \quad (3.10)$$

Using the statistical approach, we will describe the state of the system by means of a distribution function  $f$ . Due to the symmetry of the problem, all quantities, including  $f$ , are expected to be independent on the  $(x, y)$  position. The distribution function  $f$  is determined by the number of electrons in a small momentum volume  $d\mathbf{k} = dk_x dk_y$  per unit area:

$$n(\mathbf{k}, t) = \frac{\Delta N}{\Delta S} = f(\mathbf{k}, t) \frac{d\mathbf{k}}{2\pi^2}. \quad (3.11)$$

In the absence of external fields,  $f$  is given by the equilibrium Fermi-Dirac distribution

$$f_0(\varepsilon) = \frac{1}{1 + \exp\left(\frac{\varepsilon - \mu}{k_B T}\right)}. \quad (3.12)$$

The knowledge of the distribution function allows to calculate any property of the system. In particular, the current density is given by the integral

$$\mathbf{j} = e \int \frac{d\mathbf{k}}{2\pi^2} f \mathbf{v}. \quad (3.13)$$

In order to determine the response of the system to the applied fields, one has to solve the Boltzmann equation [22, 23]:

$$\frac{\partial f}{\partial t} + \mathbf{v} \cdot \frac{\partial f}{\partial \mathbf{r}} + e(\mathbf{E}e^{-i\omega t} + \frac{1}{c}\mathbf{v} \times \mathbf{B}) \cdot \frac{1}{\hbar} \frac{\partial f}{\partial \mathbf{k}} = \left(\frac{\partial f}{\partial t}\right)_{\text{collision}}. \quad (3.14)$$

The collision integral  $(\frac{\partial f}{\partial t})_{\text{collision}}$  describes the change of  $f$ , caused by the scattering on impurities, phonons, etc. In general case, the expression for  $(\frac{\partial f}{\partial t})_{\text{collision}}$  contains an integration of scattering probabilities  $W_{\mathbf{k},\mathbf{k}'}$  over momentum space,  $W_{\mathbf{k},\mathbf{k}'}$  being dependent on  $f$ . We will restrict to the so-called relaxation time approximation. We assume that the scattering processes can be taken into account by the simple collision integral

$$\left(\frac{\partial f}{\partial t}\right)_{\text{collision}} = \frac{f - f_0}{\tau(k)}. \quad (3.15)$$

In the absence of external fields,  $f_0$  satisfies Eq. (3.14) with the collision integral (3.15). We try the solution of Eq. (3.14) in the form

$$f(\mathbf{k}, t) = f_0(\varepsilon(\mathbf{k})) + g(\mathbf{k})e^{-i\omega t}. \quad (3.16)$$

Since  $f_0$  is time-independent, the partial time derivative takes the form  $\partial f / \partial t = -i\omega g e^{-i\omega t}$ . The space derivative  $\partial f / \partial \mathbf{r} = \mathbf{0}$ , since  $f$  does not depend on the position in  $xy$ -plane. In the linear approximation we neglect the terms, proportional to  $\mathbf{E}^2$  and higher. Thus we assume  $g \propto E$  and use the approximate transformation:

$$\mathbf{E} \cdot \frac{\partial}{\partial \mathbf{k}} (f_0 + g e^{-i\omega t}) \approx \mathbf{E} \cdot \frac{\partial f_0}{\partial \mathbf{k}} = \mathbf{E} \cdot \frac{\partial f_0}{\partial \varepsilon} \frac{\partial \varepsilon}{\partial \mathbf{k}} = \hbar \mathbf{E} \cdot \mathbf{v} \frac{\partial f_0}{\partial \varepsilon}. \quad (3.17)$$

We have thus the intermediate equation for the unknown function  $g$ :

$$\left(\frac{1}{\tau} - i\omega\right)g + e\mathbf{E} \cdot \mathbf{v} \frac{\partial f_0}{\partial \varepsilon} + \frac{e}{c\hbar}(\mathbf{v} \times \mathbf{B}) \cdot \frac{\partial g}{\partial \mathbf{k}} = 0. \quad (3.18)$$

The next substitution

$$g = y \frac{\partial f_0}{\partial \varepsilon} \quad (3.19)$$

allows to rewrite the equation in a slightly more compact form. The derivative over  $\mathbf{k}$  transforms as

$$\frac{\partial}{\partial \mathbf{k}} \left(y \frac{\partial f_0}{\partial \varepsilon}\right) = \frac{\partial y}{\partial \mathbf{k}} \frac{\partial f_0}{\partial \varepsilon} + y \frac{\partial^2 f_0}{\partial \varepsilon^2} \hbar \mathbf{v}. \quad (3.20)$$

After a substitution into Eq. (3.18) the second term, proportional to  $\mathbf{v}$ , gives zero and the equation for  $y$  is

$$\left(\frac{1}{\tau} - i\omega\right)y + e\mathbf{E} \cdot \mathbf{v} + \frac{e}{c\hbar}(\mathbf{v} \times \mathbf{B}) \cdot \frac{\partial y}{\partial \mathbf{k}} = 0. \quad (3.21)$$

Thus far, the circular symmetry, expressed by Eqs. (3.9–3.10) was not used. Let us choose a coordinate system, in which the electric field  $\mathbf{E}$  is directed along  $x$ -axis (Fig. 3.2). We use the expression (3.10) for  $\mathbf{v}$  and try a solution in the form

$$y(\mathbf{k}) = \alpha(k)k_x + \beta(k)k_y = \alpha(k)k \cos(\varphi) + \beta(k)k \sin(\varphi). \quad (3.22)$$

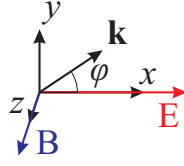


Figure 3.2

After some straightforward calculations, one obtains a linear system for  $\alpha$  and  $\beta$ , which solution is given by

$$m_c(k) = \frac{\hbar^2 k}{\varepsilon'(k)}; \quad (3.23)$$

$$\Omega(k) = \frac{eB}{m_c c}; \quad (3.24)$$

$$\alpha(k) = -\frac{eE\hbar\tau(k)}{m_c(k)} \frac{1 - i\omega\tau(k)}{(1 - i\omega\tau(k))^2 + (\Omega(k)\tau(k))^2}; \quad (3.25)$$

$$\beta(k) = \frac{eE\hbar\tau(k)}{m_c(k)} \frac{\Omega(k)\tau(k)}{(1 - i\omega\tau(k))^2 + (\Omega(k)\tau(k))^2}. \quad (3.26)$$

The current density can be calculated now with the use of Eq. (3.13). Since  $\mathbf{j} = \mathbf{0}$  in equilibrium,  $f_0$  can be omitted in the integral:

$$\begin{aligned} \mathbf{j} &= e^{-i\omega t} \int \frac{e}{2\pi^2} g \mathbf{v} d\mathbf{k} = e^{-i\omega t} \frac{e}{2\pi^2} \int_0^{+\infty} k dk \int_0^{2\pi} d\varphi \frac{\varepsilon'}{\hbar} \frac{\partial f_0}{\partial \varepsilon} k \begin{pmatrix} \cos \varphi \\ \sin \varphi \end{pmatrix} (\alpha \cos \varphi + \beta \sin \varphi) = \\ &= e^{-i\omega t} \frac{e}{2\pi\hbar} \int_0^{+\infty} k^2 \varepsilon' \frac{\partial f_0}{\partial \varepsilon} \begin{pmatrix} \alpha \\ \beta \end{pmatrix} dk. \end{aligned} \quad (3.27)$$

In the limit of low temperatures the distribution function  $f_0$  tends to the Heaviside step function and its derivative tends to the delta function:

$$f_0(\varepsilon) = \begin{cases} 1, & \text{if } \varepsilon < \mu; \\ 0, & \text{if } \varepsilon > \mu; \end{cases} \quad \frac{\partial f_0}{\partial \varepsilon} = -\delta(\varepsilon - \mu). \quad (3.28)$$

In this case the two-dimensional electron density is connected to the Fermi wave vector  $k_F$ , defined by  $\varepsilon(k_F) = \mu$ , as follows:

$$n = \int_0^{+\infty} \frac{f_0(\varepsilon(k))}{2\pi^2} 2\pi k dk = \frac{k_F^2}{2\pi}. \quad (3.29)$$

After changing to integration over the energy in (3.27) and using Eqs. (3.28–3.29), the current density takes the form

$$\mathbf{j} = -\frac{ne}{\hbar} \begin{pmatrix} \alpha \\ \beta \end{pmatrix} e^{-i\omega t}. \quad (3.30)$$

The conductivity tensor, corresponding to relation (3.30), coincides with the tensor (3.6) from the Drude model. The phenomenological Drude parameters are in the following correspondence with the parameters of the statistical treatment:  $n$  is the two-dimensional electron density (3.29),  $\tau = \tau(k_F)$  is the relaxation time at the Fermi level, and the effective cyclotron mass  $m = m_c(k_F)$  is determined by the band structure (3.23). Equation (3.23) for the effective mass is in agreement with the customary definition of  $m_c$  through the  $k$ -space area  $A$  enclosed by the electron orbit [18]:

$$m_c = \frac{\hbar^2}{2\pi} \frac{\partial A}{\partial \varepsilon} = \frac{\hbar^2}{2\pi} \frac{\partial(\pi k^2)}{\partial k} \frac{\partial k}{\partial \varepsilon} = \frac{\hbar^2 k}{\varepsilon'}.$$

In the case of a parabolic dispersion  $\varepsilon = \hbar^2 k^2 / (2m)$  the cyclotron mass does not depend on the electron density:  $m_c = m$ . In the case of a linear dispersion  $\varepsilon = \hbar v k$  the cyclotron mass changes with the density, as it follows from Eqs. (3.23, 3.29):

$$m_c = \frac{\hbar k_F}{v} = \frac{\hbar \sqrt{2\pi n}}{v}.$$

Thus in the case of the strongly degenerate Fermi gas the conductivity can be treated correctly in terms of the one-particle model. This model will be used again in section 3.3 in order to analyze an effect of a superradiant decay.

### 3.3 Superradiant decay and Drude relaxation time

In section 3.1 we treated the motion of electrons, driven by an external electromagnetic wave. Now we will consider a process of relaxation in the absence of external harmonic fields (a static magnetic field  $\mathbf{B}$  is still applied). The motion of an electron in this case is described by Eq. (3.2). The field  $\mathbf{E}_{\text{self}}$  is determined by all other electrons. Therefore the relaxation process of the electron can depend on the state of the whole gas. We assume that in the moment  $t = 0$  all electrons have the same velocity and they are uniformly distributed in the plane. Such a state can be created by a fast switching off the driving field or by applying a  $\delta$ -pulse to the gas at rest. While the electrons accelerate, the gas radiates electromagnetic waves. The radiation causes an additional loss of the kinetic energy, therefore the electrons would slow down even in the absence of scattering ( $1/\tau = 0$ ). Taking into account the symmetry of the problem, we can expect the radiation of two plane waves with wave vectors  $\mathbf{k}$  and  $-\mathbf{k}$  that are perpendicular to the plane, see Fig. (3.3). The amplitude of the magnetic field  $\mathbf{H}$  near the plane can be determined by applying the integral form of Maxwell's equation to the contour  $C$ :

$$\oint_C \mathbf{H} \cdot d\mathbf{l} = \frac{4\pi}{c} I,$$

where  $I$  is the current that the contour encloses. The term with  $\partial \mathbf{E} / \partial t$  can be omitted since we take the contour  $C$  of a vanishing area. Thus  $H$  is connected to the two-dimensional current density as  $H = 2\pi j / c$ . Since  $E = H$  in a plane harmonic wave, the electric field is given by

$$\mathbf{E}_{\text{self}} = -\frac{2\pi}{c} \mathbf{j} = -\frac{2\pi}{c} en \mathbf{v}. \quad (3.31)$$

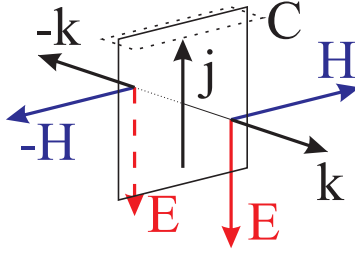


**Figure 3.3:** Radiation of a two-dimensional electron gas.

The electric field, induced by the gas, is antiparallel to the current density, as it is expected for the relaxation motion. Equation (3.2) transforms thus to

$$\ddot{\mathbf{r}} + \left(\frac{1}{\tau} + \frac{2\pi e^2 n}{mc}\right)\dot{\mathbf{r}} - \frac{e}{mc}\dot{\mathbf{r}} \times \mathbf{B} = 0. \quad (3.32)$$

We try the solution in the form of  $\dot{\mathbf{r}} = \mathbf{v}_0 e^{-i\omega t}$ , where  $\omega$  is a complex unknown and  $\mathbf{v}_0$  is a constant complex vector. By substituting it in Eq. (3.32) we obtain the linear system:

$$\begin{cases} (\Gamma - i\omega)v_{0x} - \Omega v_{0y} = 0; \\ \Omega v_{0x} + (\Gamma - i\omega)v_{0y} = 0, \end{cases} \quad (3.33)$$

where  $\Omega = eB/(mc)$  is again the cyclotron frequency and  $\Gamma = 1/\tau + 2\pi e^2 n/(mc)$ . In order to have a non-trivial solution  $\mathbf{v}_0 \neq \mathbf{0}$ , the determinant must be equal to zero. This condition is satisfied for  $\omega = \pm\Omega - i\Gamma$ . The components of the corresponding solutions are connected as  $v_{0x} = \pm i v_{0y}$ . If we choose the coordinate system, in which at  $t = 0$  the gas moves in  $x$ -direction, then the solution is

$$\dot{\mathbf{r}}(t) = v \begin{pmatrix} \cos(\Omega t) \\ -\sin(\Omega t) \end{pmatrix} e^{-\Gamma t}. \quad (3.34)$$

In the absence of scattering ( $1/\tau = 0$ ) and other electrons ( $n = 0$ ) the electron would move along a circle with the angular frequency  $\Omega$ . The scattering causes the exponential decrease of the speed and the presence of other electrons leads to the same effect. The loss of kinetic energy of the gas per unit of area

$$\frac{dE}{dt} = n\mathbf{v} \cdot \frac{d(m\mathbf{v})}{dt} = -\frac{nv^2 m e^{-\Gamma t}}{\tau} - \frac{2\pi e^2 n^2 v^2 e^{-\Gamma t}}{c}$$

consists of two terms. The first term, proportional to the electron density  $n$ , stands for the losses due to the viscous friction force. The second term, proportional to the squared electron density  $n^2$ , is equal to the radiation power. It is due to  $n^2$  dependency the effect was named “superradiance”: in the case of the coherent motion the radiation losses increase faster than linearly with the number of emitters [24].

Equations (3.31, 3.34) result in the expression for the electric field of the radiated wave:  $E(t) \propto e^{-\Gamma t}$ . The relaxation coefficient can be represented as  $\Gamma = (1/\tau + 1/\tau_{\text{SR}})^{-1}$ . One can

obtain the value of  $\Gamma$  experimentally by measuring the exponentially decreasing response to a delta-like pulse [25]. Such experiments can be conducted with the use of the time-domain spectroscopy. If the charge density  $n$  and Drude relaxation time  $\tau$  are so large that ( $\tau_{\text{SR}} \ll \tau$ ), then  $\Gamma$  is mostly determined by the radiation losses. Because of uncertainties in the experimental values of  $\Gamma$ ,  $n$  and mass  $m$ , the estimation of  $\tau$  may become impossible. It happens if the relative error exceeds the effect of  $\tau$  on the rate  $\Gamma$ .

Continuous wave measurements also have this limitation. A direct connection between these two methods can be shown with the use of the Fourier transform. In continuous wave experiments an incident harmonic wave  $e^{-i\omega(t-z/c)}$  transmits through the gas with the coefficient

$$t_{\parallel} = \frac{1 + \frac{2\pi}{c}\sigma_{xx}}{(1 + \frac{2\pi}{c}\sigma_{xx})^2 + (\frac{2\pi}{c}\sigma_{xy})^2}. \quad (3.35)$$

The expression is obtained using Eq. (2.11) for the electron gas without a substrate ( $\beta = 0$ ). A substitution of (3.6) results in the explicit function of frequency  $\omega$ :

$$t_{\parallel}(\omega) = 1 - \frac{2\pi\sigma_0}{c\tau} \frac{(\omega + i\Gamma)i}{(\omega + i\Gamma)^2 - \Omega^2}. \quad (3.36)$$

An incident delta pulse  $E_{\text{inc}}(t - z/c) = \delta(t - z/c)$  can be treated as a linear combination of all harmonics with a constant amplitude:

$$\delta(t) = \int_{-\infty}^{+\infty} \frac{e^{-i\omega t}}{2\pi} d\omega.$$

As the harmonics transmit through the gas, each of them attenuates by the factor  $t_{\parallel}(\omega)$ . Thus in order to find the full transmitted wave one needs to calculate the inverse Fourier transform of  $t_{\parallel}(\omega)$ :

$$E_{\text{tr}}(t - z/c) = \int_{-\infty}^{+\infty} t_{\parallel}(\omega) \frac{e^{-i\omega(t-z/c)}}{2\pi} d\omega.$$

The unity term in (3.36) results in a transmitted  $\delta$ -pulse and the second term is a spectrum of a harmonically decaying function. After a formal integration one obtains  $E_{\text{tr}}(t - z/c) = 0$ , if  $t - z/c < 0$  and

$$E_{\text{tr}}(t - z/c) = \delta(t - z/c) - \frac{2\pi\sigma_0}{c\tau} e^{-\Gamma(t-z/c)} \cos(\Omega(t - z/c)), \quad (3.37)$$

if  $t - z/c \geq 0$ . Equation (3.37) reproduces the result (3.34), demonstrating that the radiation losses are taken into account in Eqs. (2.11).

In order to estimate the Drude parameters, one can fit a magnetic field dependence of the transmission coefficients at some fixed frequency with Eqs. (2.11). If the frequency is high enough ( $\omega \gg \Gamma$ ), then the dependence  $t_{\parallel}(B)$  has a dip around  $B_c = \omega mc/e$ , and  $t_{\perp}(B)$  has a peak at this point, see Fig. (3.4). The shape of the peaks in the first approximation can be characterized by their position, amplitude and width. Intuitively, one might expect

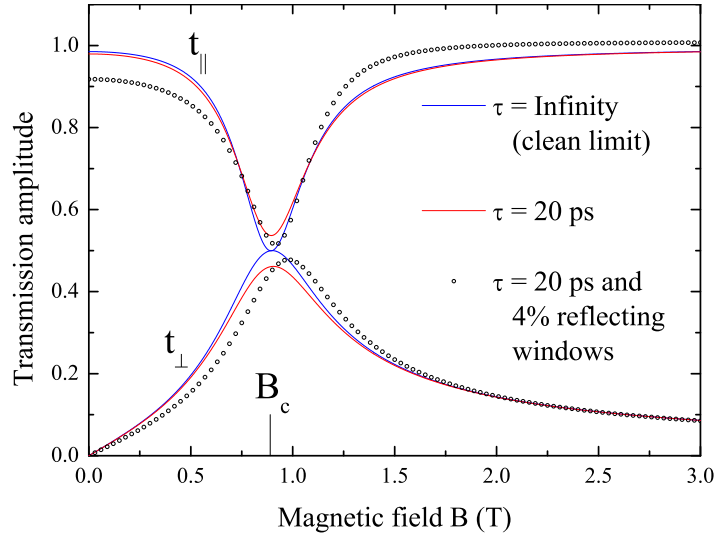


**Figure 3.4:** The shape of the cyclotron resonance in the case when radiative losses prevail over losses, caused by the scattering. The distortion of the shape (open circles) due to standing waves makes it impossible to determine the value of the Drude scattering time  $\tau$  (compare red and blue solid curves).

a direct connection between these quantities and the Drude parameters  $m$ ,  $\sigma_0$  and  $\tau$ . Such connection is valid only if the peak amplitude is small:  $|\Delta t_{\parallel,\perp}| \ll 1$ . Formally, the value of the Drude parameters has no constraints, while the amplitude of the peak cannot exceed 1. The incident linear wave can be viewed as a superposition of two circular components. In resonance, only one of the circular components is blocked, while the other one passes through with no absorption. Thus, the amplitude of the peaks is limited by the value of  $\approx 1/2$ , which can be modified due to the presence of a substrate. If  $t_{\parallel,\perp}(B_c) \approx 1/2$ , then an increase of  $\tau$  results in a negligibly small change of the resonance shape, as shown in Fig. (3.4). Red curves in Fig. (3.4) show the calculated dependencies  $t_{\parallel,\perp}(B)$  for the next set of parameters:  $n = 8 \times 10^{11} \text{ cm}^{-2}$ ,  $m = 0.07m_0$ ,  $\tau = 20 \times 10^{-12} \text{ s}$ ,  $f = 356 \text{ GHz}$ , substrate permittivity  $\varepsilon = 12$  and substrate thickness  $a = 367 \text{ }\mu\text{m}$ . The Drude parameters has been obtained in experiments on an illuminated GaAs/AlGaAs heterojunction K035x5 (see chapter 5). At 356 GHz the transfer-matrix of the substrate is close to an identity matrix, therefore the shape of the resonance is close to the one of a free-standing gas (Eq. (3.35) can be also obtained for  $\beta = \pi z$ , where  $z$  is an integer). Around  $B_c = 0.89 \text{ T}$  both transmission coefficients are close to  $1/2$ . The value of  $\tau_{\text{SR}} = mc/(2\pi e^2 n) = 1.6 \times 10^{-12} \text{ s}$  is much smaller than Drude  $\tau$  in this case. Therefore  $\Gamma$  is mostly determined by the radiation losses. Blue curves in Fig. (3.4) are calculated for  $\tau = \infty$ , other parameters remained unchanged. In addition, open circles in Fig. (3.4) show the calculated transmission through the same sample ( $\tau = 20 \times 10^{-12} \text{ s}$ ), placed between two Mylar optical windows that reflect about 4% of radiation (see section 2.2.3). Due to the standing waves, the shape of the resonance becomes distorted. As a result, the solid curves fit the open circles similarly good (bad). The fitting procedure in these conditions becomes unstable, since a slight change in the frequency leads to a totally different value of  $\tau$ , that gives the smallest residual error.

Thus the situation in continuous wave measurements is similar to the problem in the time-

domain spectrometry. In the case of the coherent motion, if the charge density is high and the Drude relaxation time is long, then the losses are mostly determined by the radiation. Since the response time (TDS) and the width of the resonance (CW) can be estimated with a finite accuracy, the Drude relaxation time becomes impossible to determine without any additional measurements. At the same time, the charge density and the effective mass can be still determined from the spectroscopic experiments. If  $\tau$  is assumed to be frequency-independent, then a combination of transport measurements at zero frequency (or, practically, several Hz) with the spectroscopic data solves the problem.



## 4 Mercury telluride films with critical thickness

### 4.1 Introduction into physics of HgTe quantum wells

Physical properties of relativistic Dirac states [26, 27] have attracted much interest recently, as they exhibit a number of unusual and nontrivial electrodynamic properties. These effects arise from linear dispersion of the charge carriers known as Dirac cone. Within a Dirac cone the cyclotron effective mass of the charge carriers strongly depends upon the position of the Fermi level (as controlled by the charge density) and vanishes at the center of the cone. Unusual electrodynamics at the interface between classical and quantum physics is expected as, e.g., a universal Faraday effect or an anomalous Kerr rotation [28–31].

Among various materials the system HgTe is outstanding as it provides a universal tool to investigate several complementary effects within the same composition. The bulk HgTe is characterized by an inverted band structure, see Fig. 4.1. This means that the  $\Gamma_6$  band (which in conventional semiconductors is a conduction band) lays below the  $\Gamma_8$  bands (which are normally the light- and heavy-holes bands). In such a case the  $\Gamma_6$  band is a completely filled valence band, the heavy-holes subband of  $\Gamma_8$  is a valence band and the light-holes subband of  $\Gamma_8$  is a conduction band. As the light- and heavy-holes bands are degenerate at the center of the Brillouin zone, HgTe is a zero-gap semiconductor. In HgTe/CdHgTe quantum wells a thin layer of HgTe is placed between thick layers of  $\text{Cd}_{0.7}\text{Hg}_{0.3}\text{Te}$ . As the thickness of HgTe is decreased, the  $\Gamma_6$  band in the thin layer rises in the energy and at the critical thickness of 6.3 nm passes over the  $\Gamma_8$  bands. At smaller thicknesses,  $\Gamma_6$  band is located above the  $\Gamma_8$  bands and the HgTe layer becomes a "conventional" semiconductor with the non-zero gap. This behavior can be understood, taking into account the influence of the  $\text{Cd}_{0.7}\text{Hg}_{0.3}\text{Te}$  layers, characterized by the conventional order of the bands, see the right panel in Fig. 4.1. If the thickness of HgTe layer is equal to critical (6.3 nm), the gap between the  $\Gamma_6$  and the light holes from the  $\Gamma_8$  bands disappears and a two-dimensional (2D) electron gas is formed with a Dirac cone dispersion [3, 33].

Magneto-optical experiments in semiconductor films provide a well-established tool to investigate the charge dynamics in external magnetic fields [17]. Earlier this technique was successfully applied to investigate the complicated band structure in HgTe single crystals. More recently, the magneto-optics especially in the terahertz range have been utilized to study the two- and three-dimensional conducting states in graphene,  $\text{Bi}_2\text{Se}_3$  and HgTe [34–36]. Compared to transport methods, optical measurements have the advantages of being contact-free and of directly accessing the effective mass via the cyclotron resonance. Both the presence of contacts and the patterning could lead to substantial changes of carrier concentration and

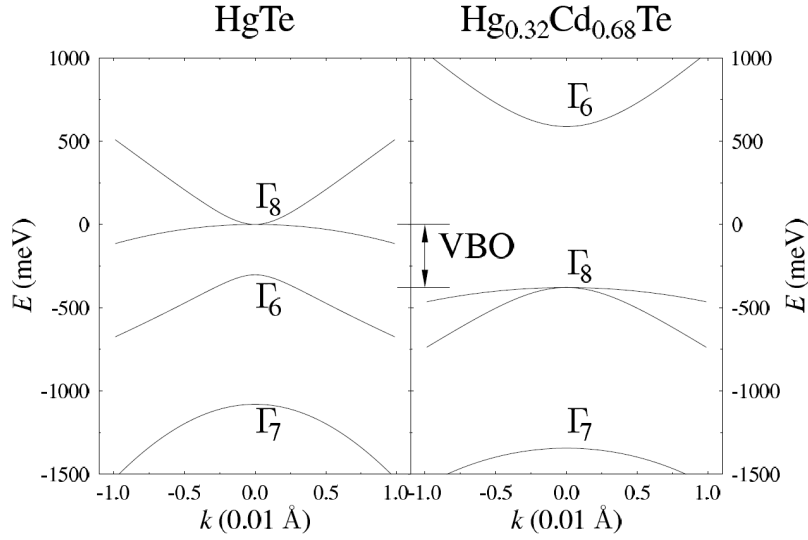


**Figure 4.1:** Band structures of  $\text{HgTe}$  and  $\text{Cd}_{0.68}\text{Hg}_{0.32}\text{Te}$ , as calculated within Kane model. The figure is taken from Refs. [5, 32].

of the position of the Fermi level. In the case of  $\text{HgTe}/\text{CdHgTe}$  quantum wells these are very crucial parameters as the most interesting phenomena are expected in the vicinity of the Dirac point. The ability to observe the cyclotron resonance is another advantage of the magneto-optical technique. The cyclotron mass of the charge carriers  $m_c$  can be determined from the resonance frequency and it is directly connected to the band structure near the Fermi level.

In experiments on the electrodynamics of two-dimensional electron gases, the control of the charge density is very important. Such parameter is necessary to shift the Fermi level between electron- and hole-conduction within the Dirac cone. A classical tool to achieve this goal is to use a transparent gate electrode to change the charge concentration. Terahertz experiments using this approach are described in section 4.4. An alternative route to modify the charge density is to use the phenomenon of persistent photoconductivity. This method is well established in  $\text{HgTe}$  semiconductors with both parabolic and linear dispersions [37–40]. At low temperatures the channel of recombination of the light-induced electrons is forbidden by the momentum conservation. The results obtained with the use of this approach are presented in section 4.3.

## 4.2 $\text{HgTe}/\text{CdHgTe}$ samples

The  $\text{HgTe}/\text{CdHgTe}$  quantum wells (QW) have been grown using the molecular beam epitaxy method. A typical detailed structure [6, 39] of QW is shown in Fig. 4.2(a). An undoped GaAs with the surface orientation (013) was used as a substrate with a thickness  $\approx 0.5$  mm. The substrate material is characterized by the scalar dielectric constant  $\epsilon_{\text{GaAs}} \approx 12$  with a negligible imaginary part in the whole range of the Mach-Zehnder spectrometer (40–1100 GHz).

During the growth the evaporated tellurium reaches the surface in a form of diatomic molecules  $\text{Te}_2$ . Analysis in terms of thermodynamics shows that at the surface the molecules

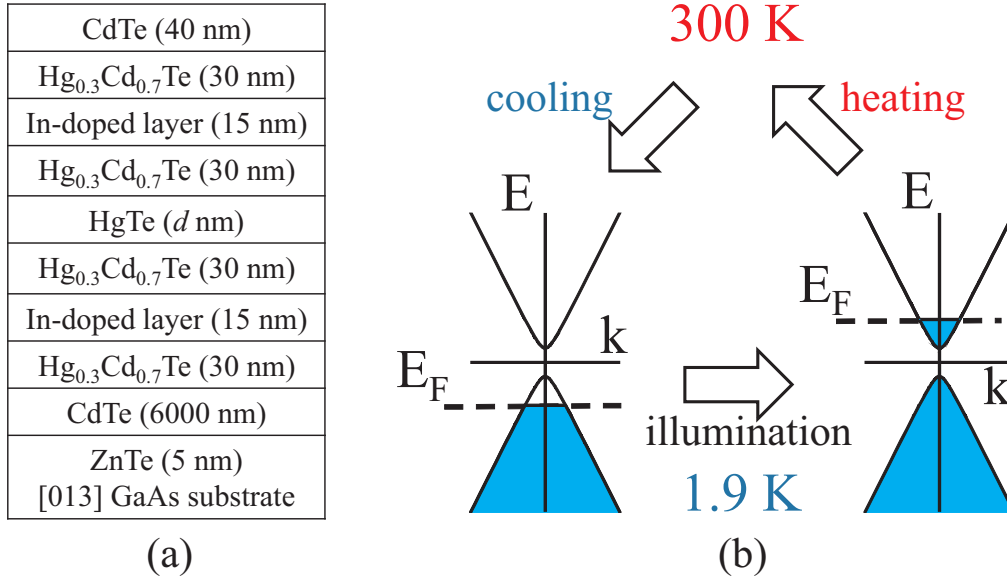


**Figure 4.2:** (a) – Detailed structure of HgTe/CdHgTe quantum wells. (b) – Control of the charge density using the phenomenon of persistent photoconductivity.

can form CdHgTe or pure Te phases [6]. The (013) surface of GaAs is less favorable for the formation of the polycrystalline tellurium [41]. Thus the usage of the (013) surface allows to reduce the density of defects and improve the quality of the heterostructures. In comparison to the samples grown on a CdTe substrate, the heterostructures on GaAs demonstrate a strong effect of persistent photoconductivity. We have used this effect to tune the charge density and the Fermi level, as described in the next section.

Control of the Fermi level by illumination was utilized in experiments with two samples that will be denoted as #1 and #2 throughout section 4.3. Sample #2 was also used in later experiments with Mylar gates, see section 4.4. The thickness  $d$  of the HgTe layer in both samples was 6.3 nm, which is close to the critical value. Mercury telluride (HgTe) films with the critical thickness are characterized by a 2D band structure with a Dirac cone in the vicinity of the Fermi energy [3, 33, 42]. Compared to the closely similar case of graphene [43], in which the Dirac cones are fourfold degenerate due to spin and valley degeneracy, in HgTe, the cone is only twofold degenerate. Another important fact is that, contrary to graphene, the Dirac cone in the 2D HgTe is predicted to be asymmetric with respect to electron and hole sides [27]. This is one more argument why information about the actual band structure is important.

## 4.3 Samples without a gate

### 4.3.1 Control of the Fermi level by illumination

An important feature of the HgTe samples on GaAs substrates is the possibility to tune the density of charge carriers in the HgTe layer utilizing the phenomenon of persistent photocon-

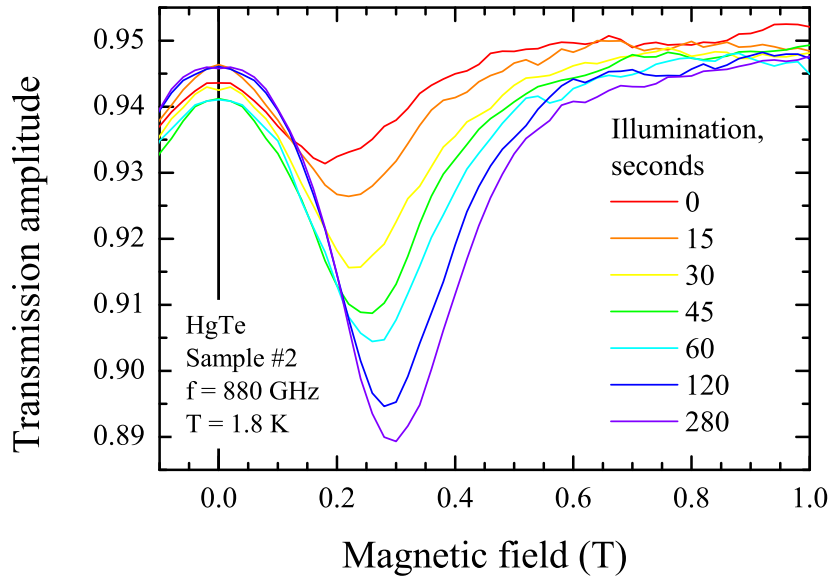


**Figure 4.3:** Demonstration of the charge control by light illumination in HgTe. The minimum in the parallel transmission around  $\approx 0.3$  T corresponds to the cyclotron resonance of the Dirac-like carriers. The deepening of the minimum under illumination reflects the increase of the charge density. The shift in position of the minimum indicates the change in effective mass according to the expression  $m_c = eB/\omega_c$ .

ductivity [44]. In order to use this method, we cool a sample down to 1.8 K in the darkness, see Fig. 4.2(b). At 1.8 K the charge density and the Fermi level take some values, affected by defects in the heterostructure. The values are not exactly reproducible after heating to the room temperature. At low temperatures illumination by visible light within several seconds causes the charge density to change. If the initial Fermi level was in the valence band, then the density of holes decreases, and if the Fermi level was in the conduction band, then the density of electrons increases. After the light is turned off, the charge density relaxes to some value, which is still different from the initial one. If the sample is kept in the darkness, this new value of the density persists for a long time period (of the orders of weeks), giving a possibility to conduct spectroscopic experiments at the fixed density. The charge density has a property to saturate at some value after a long illumination. In order to relax the electrons back to electron traps and obtain the initial conditions (approximately), the sample must be heated to 300 K and cooled down again.

In our setup the samples were illuminated by means of a green light LED mounted behind the nontransparent windows made of black paper (which is quite transparent for the terahertz radiation and opaque for IR and visible light). The amount of additional charge carriers brought into the HgTe layer is controlled by the illumination time.

### 4.3.2 Cyclotron resonance of Dirac-like carriers

Spectroscopic experiments in the terahertz frequency range ( $3 \text{ cm}^{-1} < \nu < 30 \text{ cm}^{-1}$ ) have been carried out in a Mach-Zehnder interferometer arrangement (section 2.2.1) which allows measurements of the amplitude and the phase shift in a geometry with controlled polarization

of radiation. Theoretical transmittance curves for various geometries were calculated from the susceptibilities using the matrix formalism (section 2.1).

The main results were obtained in the constant-frequency measurement mode. In such case the frequency of the terahertz radiation is fixed and both the transmission amplitude and the phase shift of the radiation passing through the sample are measured as a function of the magnetic field. With respect to the polarization of the radiation there are two main geometries which were used in our work. (In both cases a wire-grid polarizer was placed in front of the sample producing linearly polarized incidence wave.) In one case another wire-grid polarizer placed behind the sample was oriented parallel to the incident polarization. We denote this arrangement as parallel polarizers geometry. In the other case the second polarizer was oriented at  $90^\circ$  with respect to the first one. This layout is called crossed polarizers geometry. Measuring the amplitude and the phase shift of the transmitted radiation in two geometries corresponds to full determination of the transmission matrix of the sample [45]. It should be noted that for the case of trivial sample, like isotropic dielectric, only signal in the parallel geometry is expected. Nonzero signal in the crossed geometry is indicative of some sort of polarization rotation or appearance of nonzero ellipticity after passing through the sample.

Typical measured data of HgTe films in parallel and crossed geometries are shown in Fig. 4.4. The transmission amplitude in the parallel geometry is shown in the lower left panel (b). Two distinct symmetrical minima are clearly seen at low fields. They correspond to the cyclotron resonance on free charge carriers in the HgTe film. The minima at  $21 \text{ cm}^{-1}$  are located at higher fields than the minima at  $11.5 \text{ cm}^{-1}$ , which is in accordance with the linear dependence of the cyclotron resonance upon the magnetic field:  $\Omega_c \propto B$ . For the case of charge carriers with Dirac-like dispersion a nontrivial dependence of the cyclotron resonance could be expected:  $\Omega_c \propto \sqrt{B}$  (see section 4.3.6). However this case is realized only at high magnetic fields, when only few Landau levels are filled and the transitions between the Landau levels are observed separately. In the present case several transitions between the Landau levels are overlapping, which leads to a recovery of the classical behavior with  $\Omega_c \propto B$ .

The lower right panel of Fig. 4.4 demonstrates the transmission amplitude in the crossed polarizers geometry. The signal is zero without magnetic field, rises rapidly in low fields reaching a maximum value and decreases upon the further increase of the magnetic field. The emergence of the nonzero crossed signal is the manifestation of the dynamic Hall effect. Detailed analysis of the data including the phase shift shows that both the rotation of the polarization and the nonzero ellipticity of the radiation after passing through the sample are present in HgTe. For a rather clean sample, where the relaxation rate of the charge carriers is lower than the cyclotron frequency ( $1/\tau < \Omega_c$ ), the maximum in the crossed transmission signal also correspond to the position of the cyclotron resonance.

Upper panels in Fig. 4.4 show magnetic field dependence of the phase shift of the radiation after passing through the sample. The upper left panel (a) corresponds to the parallel polarizers geometry and the upper right panel (c) is for the crossed polarizers geometry. The phase shift is represented as a geometrical shift of the mirror of the spectrometer needed to compensate for the phase shift caused by the sample. This value corresponds to the change in the optical thickness of the sample. The phase shift in radians is then  $\Delta\varphi = 2\pi\Delta l/\lambda$ ,

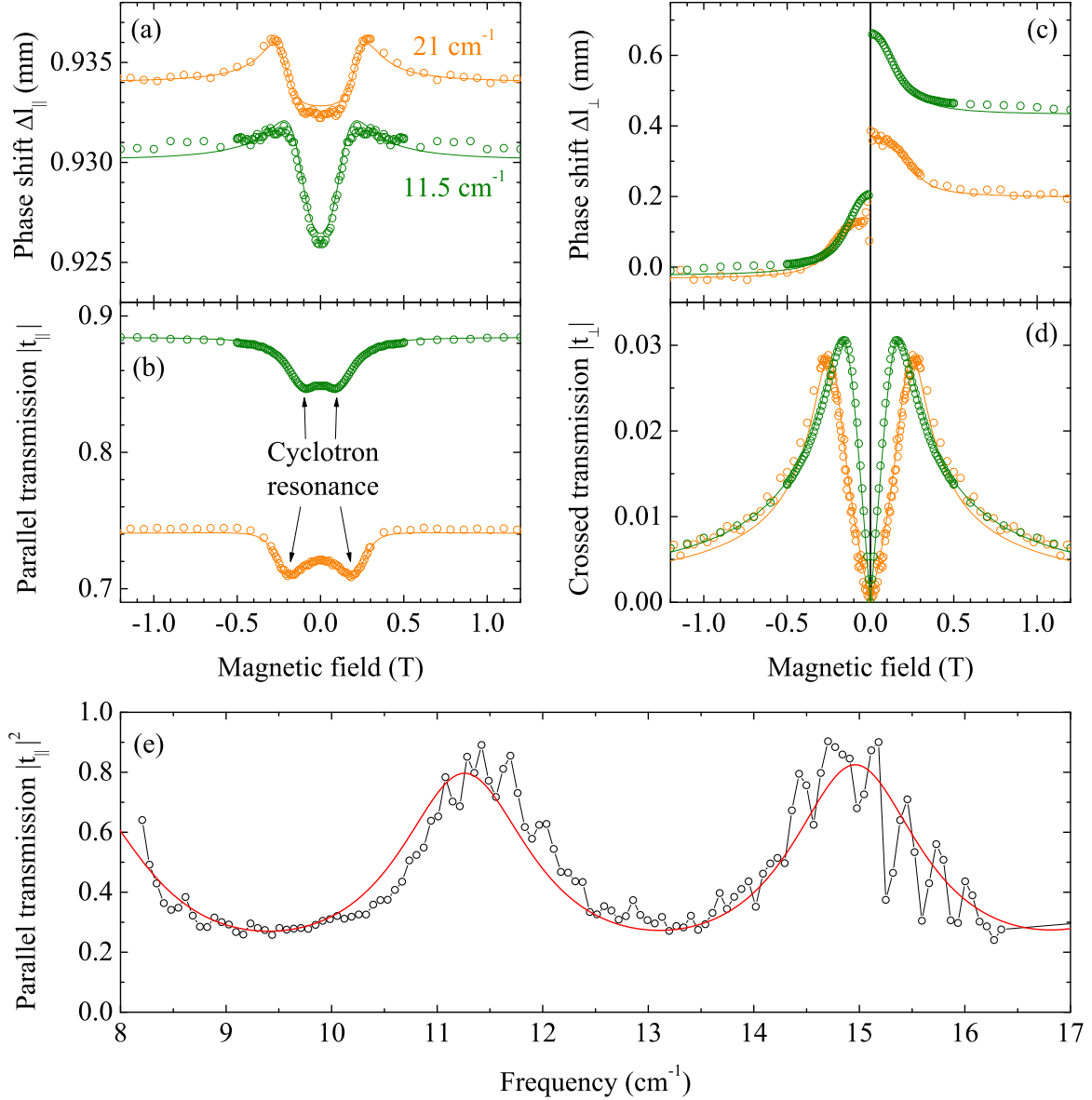


**Figure 4.4:** Magnetic field dependence of the transmission through 6.3 nm thin HgTe sample #1 after 45 seconds illumination time in the parallel polarizers geometry (a), (b) and in the crossed polarizers geometry (c), (d). The upper panels (a) and (c) show the phase shift measured as the displacement of the movable mirror of the spectrometer, the lower panels (b) and (d) show the transmission amplitude through the sample. The panel (e) demonstrates the frequency dependence of the transmission in zero external magnetic field. Green open circles are experimental data at 11.5  $\text{cm}^{-1}$ , orange open squares – at 21  $\text{cm}^{-1}$ , solid lines are fits using the Drude model as described in the text.

where  $\lambda$  is the wavelength of the radiation. Whereas the experimental data in the parallel geometry in the panel (a) show only relatively small changes, the data in the panel (c) for the crossed geometry reveal an abrupt jump at zero magnetic field. This is due to the fact that the crossed signal is changing sign when the magnetic field sweeps from positive to negative values, which corresponds to the change in the phase of exactly  $\pi$ , or the half wavelength  $\lambda/2$  as in Fig. 4.4(c).

Figure 4.4(e) demonstrates a typical spectrum in the parallel polarizers geometry in zero magnetic field. The deep oscillations are caused by a Fabry-Pérot-like multiple reflections within the transparent substrate, which in the particular case was 0.387 mm thick undoped GaAs. The values of the maxima in transmission are close to unity, demonstrating high transparency of the HgTe film. The decrease of their amplitude towards low frequencies is in accordance with the Drude-like behavior of the charge carriers, when their relaxation rate is located in the experimental frequency range.

### 4.3.3 Fitting the transmission using the Drude model

In order to analyze the magneto-optical data, the Drude model (sections 3.1–3.2) has been proved to provide an adequate description [29, 31, 36]. Within this model the sample of mercury telluride is modeled by an infinitely thin film with a two-dimensional conductivity  $\sigma_{2D}$ . In the case of nonzero magnetic field normal to the film (along the  $z$ -axis) the conductivity is a  $(2 \times 2)$  tensor with all components different from zero, see Eq. (3.6). The complex transmission coefficients for a two-dimensional conducting film on an isotropic dielectric substrate can be obtained analytically with the use of Eq. (2.11–2.13). From now on we will omit the thickness  $d$  of the conducting film and treat the conductivities and densities as two-dimensional quantities. Equations (2.12, 2.13) are given in the CGS system of units. In order to rewrite them in SI, one has to replace the impedance of vacuum  $4\pi/c$  by the corresponding SI value  $Z_0 = 1/(\epsilon_0 c) \approx 377 \Omega$ :

$$t_{\parallel} = \frac{2a_{xx}e^{-i\frac{\omega}{c}a}}{a_{xx}^2 + a_{xy}^2}; \quad t_{\perp} = \frac{2a_{xy}e^{-i\frac{\omega}{c}a}}{a_{xx}^2 + a_{xy}^2}, \quad (4.1)$$

$$a_{xx} = (1 + \sigma_{xx}Z_0)(\cos \beta - \frac{i}{\sqrt{\epsilon}} \sin \beta) + \cos \beta - i\sqrt{\epsilon} \sin \beta; \quad (4.2)$$

$$a_{xy} = \sigma_{xy}Z_0(\cos \beta - \frac{i}{\sqrt{\epsilon}} \sin \beta). \quad (4.3)$$

where  $a$  is the substrate thickness,  $\epsilon$  is the dielectric constant of the substrate,  $\omega = 2\pi f$  is the angular frequency of the radiation,  $\beta = \sqrt{\epsilon}a\omega/c$ .

The transmission coefficients can be measured as functions of the frequency and the magnetic field:  $t_{\parallel,\perp} = t_{\parallel,\perp}(f, B)$ . Normally, one variable is fixed during the measurements and the other is swept. We will call the measured set of data “(magnetic) scan”, if the frequency  $f$  was fixed and “spectrum (in field  $B$ )”, if the magnetic field was fixed at the value of  $B$ . Formally, a transmission coefficient is determined as a ratio of two complex amplitudes:  $t = E_{\text{smp}}/E_{\text{cal}}$ , where  $E_{\text{smp}}$  is measured with the sample in the beam and  $E_{\text{cal}}$  is measured without the sample. The sample is placed between the optical windows inside the magnet. The standing waves,

reflected from the windows, cause the measured coefficient  $t$  to deviate from the coefficient  $t^{\text{free}}$  that would be obtained in free space. For this reason the transmission coefficient, measured at a single point  $(f_0, B_0)$  according to the definition, cannot be directly analyzed using equations for the case of free space.

In order to overcome this problem, the next idea can be used. The deviation, caused by the standing waves oscillates around zero as a function of the frequency, see Fig. 4.4(e). One can measure the spectrum  $t(f, 0)$  at  $B = 0$  and fit it using the model for free space. The value of the fitting function  $t^{\text{fit}}(f_0, 0)$  is supposed to be a good approximation for  $t^{\text{free}}(f_0, 0)$ . The transmission values in the field scan  $t(f_0, B)$  at  $f_0$  should be divided by the complex number  $a = t(f_0, 0)/t^{\text{fit}}(f_0, 0)$ . After this “correction” the dependence  $t(f_0, B)/a$  is assumed to be a good approximation for  $t^{\text{free}}(f_0, B)$ , since they are matched at least at  $B = 0$ . In other words, the ratio  $t(f_0, B)/t^{\text{free}}(f_0, B)$  is assumed to be independent on the magnetic field  $B$  and  $t^{\text{free}}(f_0, 0)$  is estimated from the fit of the spectrum  $t(f, 0)$ . Instead of the matching at a single point  $(f_0, 0)$ , one can choose  $a$  that minimizes the norm

$$\|t(f_0, B) - at^{\text{fit}}(f_0, B)\|^2 = \sum_{B_k} \left( |t(f_0, B_k) - at^{\text{fit}}(f_0, B_k)|^2 \right).$$

The idea can be realized numerically as follows. Suppose the transmission coefficients  $t_{\parallel, \perp}^{\text{exp}}$  have been measured as a spectrum in zero field and a scan at a fixed frequency  $f_0$ . Let us denote as  $t_{\parallel, \perp}^{\text{th}}$  the theoretical values, calculated using Eqs. (2.11–2.13) for some Drude parameters  $(\sigma, \tau, m)$ . Then we minimize the expression for the residual error

$$\begin{aligned} r(\sigma, \tau, m, \varepsilon, a_{\parallel}, a_{\perp}) = & \beta_0 \sum_{f_k} \left( |t_{\parallel}^{\text{exp}}(f_k, 0) - t_{\parallel}^{\text{th}}(f_k, 0)|^2 \right) + \\ & + \beta_{\parallel} \sum_{B_k} \left( |t_{\parallel}^{\text{exp}}(f_0, B_k) - a_{\parallel} t_{\parallel}^{\text{th}}(f_0, B_k)|^2 \right) + \beta_{\perp} \sum_{B_k} \left( |t_{\perp}^{\text{exp}}(f_0, B_k) - a_{\perp} t_{\perp}^{\text{th}}(f_0, B_k)|^2 \right) \end{aligned} \quad (4.4)$$

by varying the Drude parameters  $(\sigma, \tau, m)$ , the substrate dielectric constant  $\varepsilon$  and two complex scaling coefficients  $a_{\parallel, \perp}$ . The coefficients  $\beta_{0, \parallel, \perp}$  allow to adjust the weight of the spectrum and the scans in the residual  $r$ . Note that the spectrum must be measured according to the definition  $t = E_{\text{smp}}/E_{\text{cal}}$ , while in the scans the calibration measurement of  $E_{\text{cal}}$  is not required (if the signal of BWO does not depend on the magnetic field). One can include scans, measured at several frequencies, and spectra, measured at different magnetic fields, by adding corresponding terms in Eq. (4.4).

It is possible to minimize the residual (4.4) even if the complex phases  $\arg(t^{\text{exp}})$  have not been measured. In the samples with a high mobility the cyclotron resonance reveals as the distinct peaks and dips in the absolute values of the transmission coefficients, see Fig. 4.4. Any peak can be characterized by its position, amplitude and width. The Drude parameters  $(\sigma, \tau, m)$  are determined by the shape of the cyclotron resonance (see section 3.3 for details). The dielectric constant of the substrate  $\varepsilon$  is well defined by the oscillations in the zero-field spectrum. Thus the fitting procedure remains stable, if we use the absolute values  $|t|$  instead of the complex ones. However the knowledge of the complex phase can help to correct the transmission coefficient before the fitting.



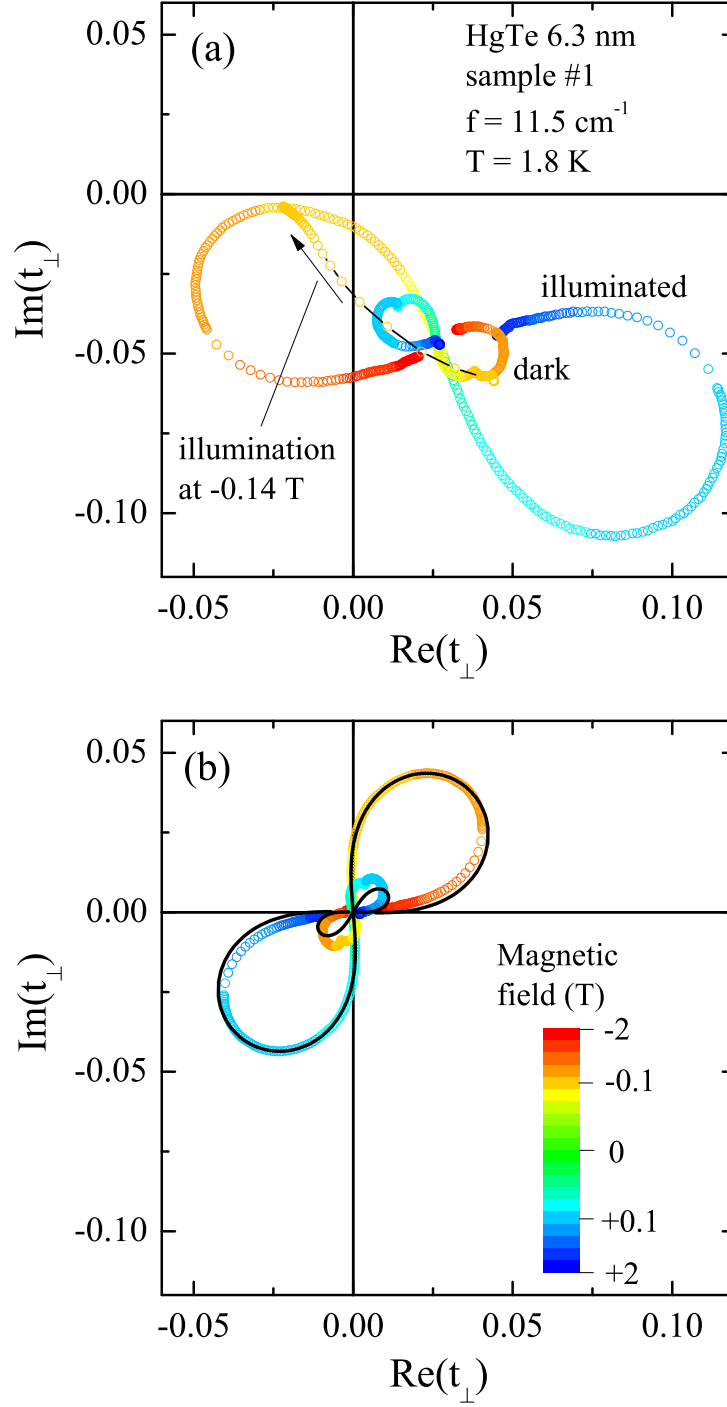


**Figure 4.5:** Crossed transmission  $t_{\perp}(B)$  through the sample #1 at  $11.5 \text{ cm}^{-1}$  on a complex plane as a parametric plot with the magnetic field as a parameter. (a) – The complex data is reconstructed from the experimental amplitude and the phase shift. The inner eight-shaped curve corresponds to the dark sample and the outer one corresponds to the illuminated sample. Orange symbols demonstrate the illumination process taken at  $B = -0.14 \text{ T}$ . Note the change of the orientation of the lobes between the dark and the illuminated sample, corresponding to the change from the hole-like to the electron-like charge carriers. (b) – An antisymmetric part of  $t_{\perp}(B)$  (open circles) and corresponding fits within the Drude model (solid lines).

The linear polarization of electromagnetic radiation is strictly defined in case of an infinite plane wave only. In the ideal case the complex coefficient  $t_{\parallel}(B)$  is an even function of the magnetic field, and  $t_{\perp}(B)$  is an odd function. In the real experimental setup the beam is restricted by the size of the optical elements and by the superconducting magnet. These factors, along with imperfections of polarizers, lead to the depolarization of the optical beam, revealed as a deviation from the perfect symmetry in the experimental data. To reduce these external contributions, we take a symmetric part of the experimental complex coefficient  $t_{\parallel}$  as  $[t_{\parallel}(B) + t_{\parallel}(-B)]/2$  and an antisymmetric part of  $t_{\perp}$  as  $[t_{\perp}(B) - t_{\perp}(-B)]/2$ . Normally, the procedure results in a negligibly small correction for the parallel transmission coefficient.

On the contrary, the antisymmetrization of the crossed coefficient typically leads to a substantial correction of  $t_{\perp}$ . Open symbols in Fig. 4.5(a) show the raw complex  $t_{\perp} = |t_{\perp}| e^{ik\Delta l_{\perp}}$  as a parametric plot with the magnetic field as a hidden parameter (coded by color). Since the data has not been divided by a calibration measurement, the shape is arbitrarily scaled with respect to the origin (0, 0) and is rotated around it by some unknown angle. The eight-like shape of the curves can be described within the Drude model. An example of curves, calculated within the Drude model, is shown in Fig. 4.5(b) by solid lines. In zero field the crossed transmission is expected to turn into zero. However the raw experimental value  $|t_{\perp}(0)|$  is comparable to the amplitude at the resonant field  $|t_{\perp}(B_c)|$ . The problem is caused by the small absolute value of  $|t_{\perp}|$  that does not exceed  $\approx 0.05$  even in the resonance. A single polarizer suppresses the crossed component of the radiation to a comparable value. The incident wave passes several polarizers before transmitting through the sample. However the linear polarization becomes distorted on passing through the optical windows and the restricted volume of the magnet. We have no practical solution that would allow to suppress the depolarization and to obtain a perfectly antisymmetric crossed signal experimentally. Thus the only possibility to analyze the data is to use some sort of correction.

The value of  $|t_{\perp}(0)|$  characterizes how large is the distortion of the crossed signal. Figure 4.5(a) shows an example of the crossed data, in which the relative distortion is large (especially for the dark sample). Even in this case the shape of the curve on the complex plane seems to be preserved. In zeroth approximation we assume that the depolarization leads to a shift of the whole curve without changing its shape. The simplest correction of this distortion is the complex subtraction of the value in zero field:

$$t_{\perp}^{\text{corr}}(B) = t_{\perp}(B) - t_{\perp}(0). \quad (4.5)$$

After this transformation the corrected coefficient  $t_{\perp}^{\text{corr}}(B)$  remains slightly non-antisymmetric, as the lobes of the experimental eight-shaped curve are not perfectly equal. This smaller distortion can be a consequence of an admixture of the parallel component, which is symmetric in the magnetic field. Usually the polarizers in the crossed geometry are oriented to minimize  $|t_{\perp}(0)|$  in zero magnetic field. Generally, it does not guarantee that the parallel component, passing through the sample, is completely suppressed, since there might be some radiation, going around the sample. Both parasitic contributions can be removed by taking the antisymmetric part of the experimental crossed coefficient:

$$t_{\perp}^{\text{corr}}(B) = \frac{t_{\perp}(B) - t_{\perp}(-B)}{2}. \quad (4.6)$$

The symmetric part of the experimental crossed coefficient

$$t_{\perp}^{\text{err}}(B) = \frac{t_{\perp}(B) + t_{\perp}(-B)}{2} \quad (4.7)$$

can be analyzed to justify the validity of the assumptions. It is expected to be a linear combination of a constant signal and the parallel coefficient  $t_{\parallel}(B)$ :

$$t_{\perp}^{\text{err}}(B) = \alpha_1 + \alpha_2 t_{\parallel}(B), \quad (4.8)$$

where  $\alpha_{1,2}$  are constant complex coefficients. The first term is due to the radiation, going around the sample, and the second term is due to the radiation, passing through the sample. Thus the symmetric part  $t_{\perp}^{\text{err}}(B)$  must be constant far from the resonance, at  $B \gg B_c$ .

The residual error (4.4) contains the parallel spectrum  $t_{\parallel}^{\text{exp}}(f, 0)$  in “absolute units”, calibrated by a measurement without the sample. Due to the depolarization effects, measuring a calibrated crossed spectrum  $t_{\perp}^{\text{exp}}(f, B_0)$  is a big experimental challenge, especially in the case of a weak resonance. If the conductivity tensor is determined by the Drude model, then the connection between  $t_{\parallel}$  and  $t_{\perp}$  can be better demonstrated in the basis of circular polarizations. Let us define two circular polarization vectors  $S_{\pm} = (E_x, E_y, H_x, H_y)_{\pm}^T = (1, \pm i, \mp i, 1)^T$ . The designation  $t_{S_1 S_2}$  will denote the complex amplitude of the component  $S_2$  in the transmitted wave, if the incident wave contains only the component  $S_1$  with the amplitude 1. For the Drude model one can show the following connection between the circular and the linear transmission coefficients:

$$t_{++} = t_{\parallel} - i t_{\perp}; \quad t_{--} = t_{\parallel} + i t_{\perp}; \quad t_{+-} = t_{-+} = 0. \quad (4.9)$$

In the basis of linear polarizations, a single incident component results in a transmitted wave, in which both components are non-zero. Equation 4.9 shows that if a circular component is absent in the incident wave, then it is also absent in the transmitted wave. In order to write an explicit equation for the circular transmissions, we define the “circular” conductivities

$$\sigma_{\pm} = \sigma_{xx} \pm i \sigma_{xy} = \frac{\sigma_0}{1 - i \tau (\omega \pm \Omega)}. \quad (4.10)$$

Note that while both  $\sigma_{xx}(B)$  and  $\sigma_{xy}(B)$  have resonances at  $\pm B_c$ , the conductivities  $\sigma_{\pm}(B)$  have a resonance either in the positive, or in the negative magnetic field. We define the quantities, analogous to (4.2–4.3):

$$a_{\pm} = a_{xx} \pm i a_{xy} = (1 + \sigma_{\pm} Z_0) \left( \cos \beta - \frac{i}{\sqrt{\varepsilon}} \sin \beta \right) + \cos \beta - i \sqrt{\varepsilon} \sin \beta. \quad (4.11)$$

Then the circular transmission coefficients are given by

$$t_{++} = \frac{2e^{-i \frac{\omega}{c} a}}{a_{+}}; \quad t_{--} = \frac{2e^{-i \frac{\omega}{c} a}}{a_{-}}. \quad (4.12)$$

The equation for  $t_{++}(B)$  contains only  $\sigma_{+}(B)$  and  $t_{--}(B)$  is determined by  $\sigma_{-}(B)$ . Thus for the Drude carriers the cyclotron resonance in a circular polarization can be observed only for

one direction of the external magnetic field. If this condition is satisfied in experiments with the circular polarizations, then the uncalibrated crossed coefficient  $t_{\perp}^{\text{exp}}(B)$  can be rescaled into absolute units by minimizing the residual error (4.4).

In the absence of the standing waves, there would be no need in minimizing the residual (4.4). We would directly recalculate the experimental transmission coefficients into the conductivity tensor, using Eqs. (2.14–2.15). The fitting procedure contains an implicit assumption, that the effect of the standing waves can be reduced to a multiplication by a complex coefficient. The analysis within the framework of the matrix formalism, presented in section 2.2.3, shows that this assumption is wrong. The distortion of the shape of the cyclotron resonance leads to errors in determination of the Drude parameters. The errors increase with the amplitude of the parasitic oscillations in the zero-field spectrum. The conductivity  $\sigma_0$  and the density  $n$  turn out to be the most sensitive to the standing waves. A possible solution of the problem can be achieved by a combination of the spectroscopic experiments with transport measurements. The measurements of DC conductivity can be used for an independent determination of the charge density and the static  $\sigma_0$ .

#### 4.3.4 Drude parameters

In the scans shown in Figs. 4.3–4.4 only a single cyclotron resonance is observed. It is therefore reasonable to use only one type of charge carriers in the description. Besides, from the sign of the phase shifts it may be derived directly that the dominating carriers are negatively charged, i.e. they are electrons. The solid lines in Fig. 4.4 are model calculations according to Eqs. (2.11–2.13) superimposed with the data for 45 seconds illumination time. Good quality of these simultaneous fits of four data sets supports the validity of the approximation. However, as will be seen below, in several cases the data suggests the presence of a second type of carriers which in few cases may even dominate the scans.

The parameters of the electrons in HgTe as obtained from the fits are shown in Fig. 4.6. The upper left panel (a) demonstrates the dependence of the charge carriers density  $n$  against illumination time in the logarithmic scale. In order to accommodate the dark sample with the illumination time 0, it is formally denoted by the time of 0.1 seconds in the figure. The green circles are parameters for the sample #1 at  $11.5 \text{ cm}^{-1}$ , the orange diamonds are for the same sample at  $21 \text{ cm}^{-1}$  and the black squares are parameters of the sample #2 at  $28 \text{ cm}^{-1}$ . The change of the concentration of at least one order of magnitude is clearly achievable in the present experiment. As the illumination time is a parameter which is very specific for the particular setup and generally has limited meaning, in the following the charge carriers density  $n$  will be used in the plots as a tuning parameter.

The charge carrier relaxation rate  $1/2\pi\tau$  is shown in the upper right panel (b) of Fig. 4.6 as a function of the charge carrier density  $n$ . The fit values for the same sample #1 at two different frequencies of  $11.5 \text{ cm}^{-1}$  (green circles) and  $21 \text{ cm}^{-1}$  (orange diamonds) coincide rather well within the experimental accuracy (shown by error bars). An increase of the relaxation rate toward low carrier densities is well known in semiconductor physics and is may be explained by the decreasing screening of the random potential by the charge carriers. At low carrier densities the effective cyclotron mass becomes very small and the cyclotron resonances are not resolved anymore. In this case the determination of the parameters of the carriers becomes

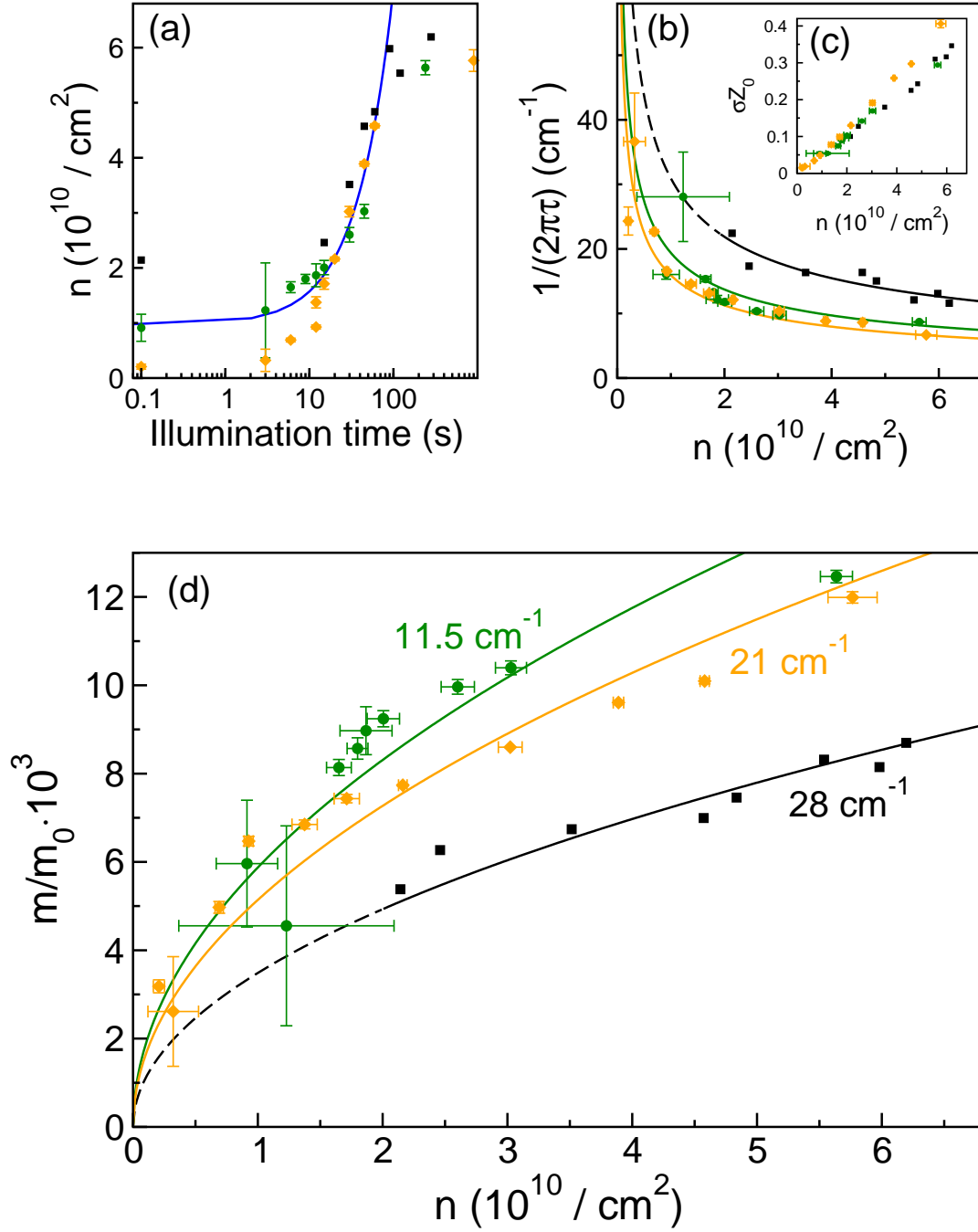


**Figure 4.6:** Fit parameters obtained from the complex transmission data in HgTe films. Black squares are parameters of the sample #2 measured at  $28 \text{ cm}^{-1}$ , green circles denote sample #1 measured at  $11.5 \text{ cm}^{-1}$  and orange diamonds are for the sample #1 at  $21 \text{ cm}^{-1}$ . Panel (a) shows the dependence of the charge carrier concentration (electrons) upon the illumination time. The data for the dark sample with no illumination is shown at  $0.1 \text{ s}$  in order to fit into the logarithmic scale. Solid line corresponds to a linear fit. Panel (b) demonstrates the relaxation rate  $1/2\pi\tau$  as a function of the carriers concentration  $n$ . Solid lines demonstrate the  $1/2\pi\tau \sim 1/\sqrt{n}$  behavior. The dimensionless 2D conductivity  $\sigma Z_0$  vs. concentration is presented in the inset (c). Here,  $Z_0 \approx 377 \text{ Ohm}$  is impedance of vacuum. The lower panel (d) demonstrate the dependence of the electron effective mass upon their concentration. The lines are square root fits of the experimental parameters.

unstable and results in large error bars. The black squares show the fit results for the sample #2 at  $28 \text{ cm}^{-1}$ . Here a systematic shift of the relaxation rate towards higher values compared to the sample #1 can be attributed to uncontrolled changes during the sample preparation.

The inset (c) in the upper right panel of Fig. 4.6 demonstrates almost linear dependence of the static conductivity  $\sigma_0$  on the charge carriers density  $n$ . The linear character of the curves and the fact that they closely coincide for both samples indicate that the mobility  $\mu$  of the charge carriers is constant across the samples and the density ranges. This is evident from the formula for the conductivity  $\sigma = ne\mu$ .

The concentration dependence of the effective electron mass in the HgTe films is shown in the panel (d) of Fig. 4.6. For both samples this dependence follows the square root law  $m_c \sim \sqrt{n}$ . Especially for the sample #1 (green circles and orange diamonds) the square root behavior can be observed in an extremely broad range of densities. The absolute values of the effective electron mass deviate only slightly for two frequencies,  $11.5 \text{ cm}^{-1}$  and  $21 \text{ cm}^{-1}$ . This may be an indication that the magnetic field dependence of the cyclotron frequency starts to deviate from the linear low-field regime and an influence of the high-field  $\Omega_c \propto \sqrt{B}$  regime is visible.

The square root behavior  $m_c \propto \sqrt{n_{2D}}$  is characteristic for the carriers with the Dirac-like dispersion relations  $E = \hbar v_F |k|$  as observed in graphene [46]. Here  $v_F = \text{const}$  is the Fermi velocity. From the expressions for the two-dimensional density  $n_{2D} = k_F^2/(4\pi)$  and quantum mechanical and classical definitions of the cyclotron frequency [18, 35]  $\omega_c = eBv_F/(\hbar k_F)$  and  $\omega_c = eB/m_c$ , respectively, one gets  $m_c = \hbar\sqrt{4\pi n_{2D}}/v_F$ . These estimates clearly support the behavior observed in Fig. 4.6(d) and they correlate well with the results at higher frequencies [38–40, 47, 48].

### 4.3.5 Hole contribution

The results presented above are clearly dominated by a single electron contribution. Therefore, the description using only one type of carriers has led to a reasonable interpretation of the data. As mentioned previously, in case where the electron contribution was small, additional details in the spectra could be detected. This can be interpreted as a contribution of a second type of carriers.

In few experiments with samples in the dark even the dominating character of the hole contribution could be observed. An example of such scans is presented in Fig. 4.5. In this figure only the transmission in crossed polarizers is shown as it is mostly sensitive to fine details of the carrier contributions. The data are given in the complex plane plot such as  $\text{Im}(t_\perp)$  is plotted as a function of  $\text{Re}(t_\perp)$  including the phase information (which should be compared to conventional presentation in Fig. 4.4). The panel (a) shows the raw complex coefficient  $t_\perp^{\text{exp}} = |t_\perp| e^{ik\Delta l_\perp}$  in arbitrary units, and the panel (b) shows the result of the fitting in the absolute units. In such a plot the magneto-optical response of the charge carriers demonstrates a characteristic figure: an eight-shaped curve. Importantly, the sign of the charge carriers is directly obtained as the orientation of the curve in the complex plane.

As a typical example, the black curve and yellow circles in Fig. 4.5(a) mark the position of  $t_\perp$  on the complex plane at  $B_{\text{light}} = -0.14 \text{ T}$ . It is clear, that the curve of the magneto-optical response in this case is inverted between the dark and the illuminated sample. In the dark

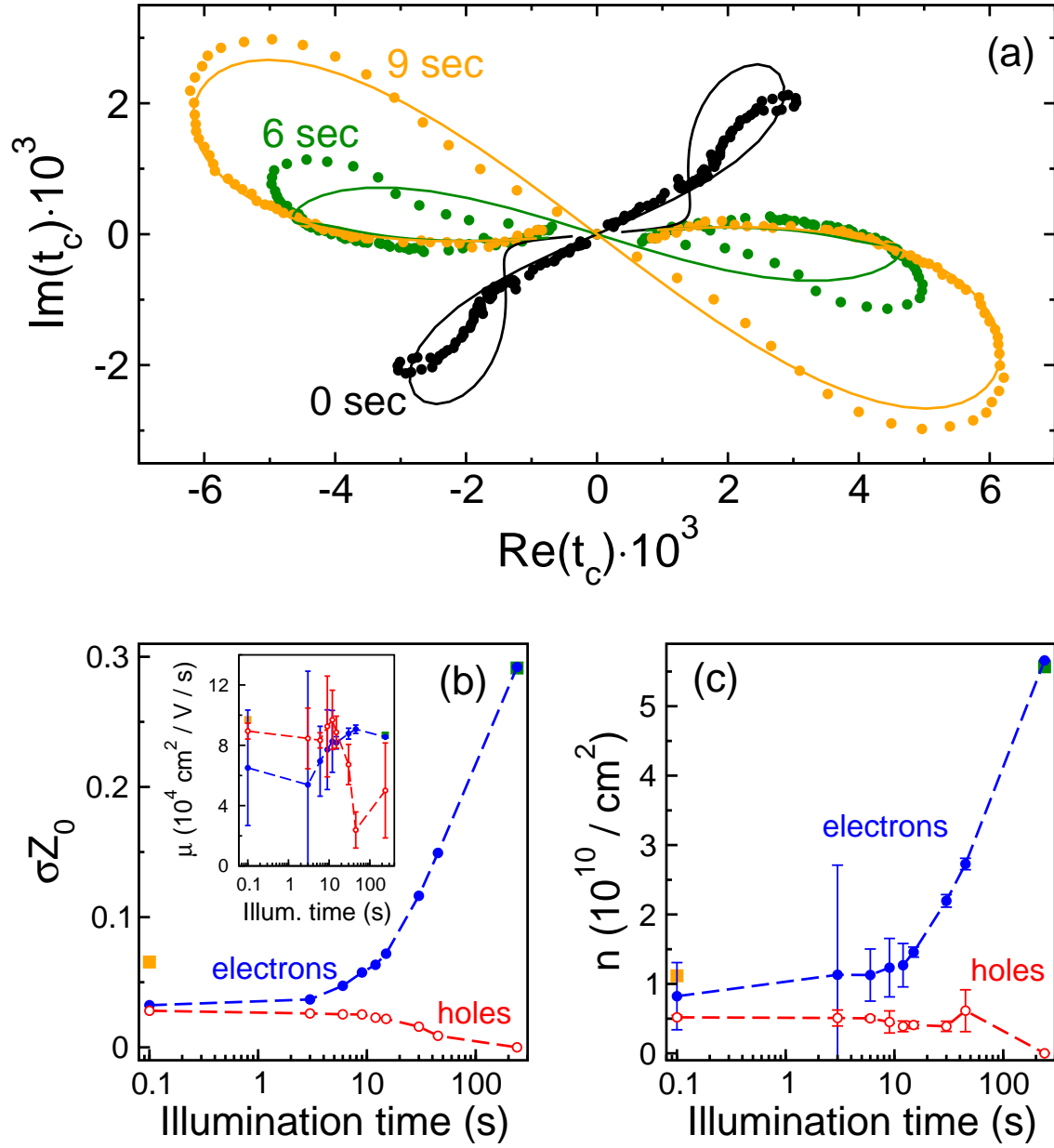


**Figure 4.7:** Panel (a) shows magnetic field dependence of transmission in crossed polarizers geometry for the sample #1 at  $11.5 \text{ cm}^{-1}$ . The data are the same as in Fig. 4.4, but represented in the polar plot form. Symbols are experimental results, lines are fits within the Drude model using two types of charge carriers. Strong deviations from the single carriers Drude model at low illumination times are clearly seen. The dimensionless conductivity  $\sigma Z_0$  and the carrier concentrations  $n$  as functions of illumination time obtained from the fits are shown in panels (b) and (c), respectively. Blue solid circles denote electrons, red open circles denote holes. The green and orange squares are fit parameters for electrons and holes as obtained from the data in Fig. 4.5. The inset in (b) shows the mobilities of holes and electrons.

case the sample shows a clear orientation of the hole contribution. After switching on the light illumination the amplitude  $t_{\perp}(B_{\text{light}})$  passes near the center of the eight-like shape and then shifts to the opposite lobe of the curve that corresponds to the illuminated sample. This behavior demonstrates the inversion from the hole to the electron contribution.

Solid lines in Fig. 4.5(b) demonstrate the results of the fitting to the measured data at fixed illumination time. The response on the electron side is well fitted by the simple model. On the hole side, only a qualitative fit may be obtained. In addition, the experimental curve shows some fine structure. This is an indication of the fact that further corrections to the hole response may be needed, e.g. inclusion of further charge carriers. However, possible additional contributions are weak and their parameters cannot be reliably extracted from the fits. Therefore, in the present discussion only two contributions to the magneto-optical response will be considered: electrons giving a main response and holes as a smaller correction.

The HgTe samples investigated in this work showed distinct memory effects. This resulted in the fact that the "dark" state of the sample could not be exactly reproduced. Possible reason for these observation is the existence of charge traps with hysteresis effects. Normally, in the dark state as obtained after cooling from room temperature and without light illumination, the contributions of holes and electrons were comparable. In this sense, clear visual separation as exemplified in Fig. 4.5 could be obtained only in the beginning of the experimental series. Another example of the spectra in the dark state is shown in Fig. 4.7(a) by black symbols. Here a more complicated picture compared to Fig. 4.5 is seen. Fortunately, the overall behavior of the experimental data could be reasonably described taking only two sorts of the charge carriers into account. The results of such fits are shown in Fig. 4.7(a) as solid lines demonstrating that even a complicated behavior may be qualitatively understood as a mixture of hole and electron contributions. The attempts to include more charge carriers into consideration did not lead to stable fits. As the response of the holes is weak, only few parameters like conductivity, density, and mobility could be determined unambiguously. The effective mass and the scattering rate of holes contribute to the mobility simultaneously as  $\mu = e\tau/m_{\text{eff}}$  and they could not be separated by the fitting procedure.

The static conductivity and the density of electrons and holes in HgTe in the approximation of two types of charge carriers are shown in Fig. 4.7(b, c). As expected, the parameters of the electrons in the two-carriers fits remain basically the same as in Fig. 4.6 (electrons only). Within the experimental accuracy the density of the holes remains independent of illumination indicating that mobile hole states are not affected by light.

An ideal Dirac cone is symmetric with respect to positive and negative directions in energy. If the Fermi level is above the Dirac point, the charge carriers are electron-like. If the Fermi level is below the Dirac point, the charge carriers will have the hole-like character. The Fermi level for the samples in the dark state is mostly determined by the preparation conditions and partly by the temperature/doping history of the sample. The samples have been fabricated with a goal to obtain the Fermi level very close to the Dirac point. After cooling in darkness, the terahertz response of the samples was usually dominated by electrons. The dispersion of the upper part of the cone was proven to be close to linear. The inability to investigate the lower part of the cone have led to the idea of making an *ex-situ* semitransparent gate to control the Fermi level (section 4.4).



### 4.3.6 Landau level FTIR spectroscopy

The terahertz analysis described above has been extended to the infrared frequency range [49, 50] (Fig. 4.8). These experiments have been performed on sample #3 with  $d = 6.6$  nm at  $T = 10$  K. The optical windows of the magnet were transparent for the visible light and the sample was constantly illuminated. The carrier density was estimated from the transmission intensity as  $n_{2D} = 7 \times 10^{10} \text{ cm}^{-2}$ . For magnetic fields  $B < 1$  T the cyclotron frequency is linear in field. In high magnetic fields  $B > 1$  T, the classical cyclotron resonance mode is split into transitions between single Landau levels. In addition, for magnetic fields above  $B \approx 4$  T, two modes with close-by frequencies are observed, which indicates that the initial twofold degeneracy of the Dirac cones is lifted in the high magnetic fields [51].

Characteristic gap in the data close to  $270 \text{ cm}^{-1}$  is due to the phonon absorption in GaAs substrate [52]. Close to  $150 \text{ cm}^{-1}$  the phonon absorption in the HgTe film [53, 54] and in the CdHgTe buffer layers [6] are seen. As the phonons in the layers with different Cd-doping are at close frequencies [53], they cannot be separated. In addition, because the HgTe film and the CdHgTe layers are close to each other, the electron gas interacts with CdHgTe phonons around  $150 \text{ cm}^{-1}$ . This interaction is seen as an effect of avoided crossing of cyclotron resonance frequency close to  $125 \text{ cm}^{-1}$  and  $170 \text{ cm}^{-1}$ .

For a simple qualitative explanation of the transitions between the Landau levels we will use the Bohr-Sommerfeld approximation. A more rigorous approach, based on a relativistic Hamiltonian, can be found in Ref. [51]. Here we will neglect the electron spin and treat one band with the energy dependence  $\varepsilon = \varepsilon(k)$ . Assume an external magnetic field  $B$  is applied in the direction, perpendicular to the film. Then the cyclotron motion of any electron is represented as a circular orbit both in  $\mathbf{r}$ - and  $\mathbf{k}$ -spaces. According to the Bohr-Sommerfeld approximation, the orbit in  $\mathbf{r}$ -space must satisfy

$$\oint \mathbf{p} \, d\mathbf{r} = \oint (\hbar \mathbf{k} - \frac{e}{c} \mathbf{A}) \, d\mathbf{r} = 2\pi\hbar(n + \gamma), \quad (4.13)$$

where  $\mathbf{p} = \hbar \mathbf{k} - e\mathbf{A}/c$  is a canonical momentum;  $\mathbf{A}$  is a vector-potential, satisfying  $\mathbf{B} = \nabla \times \mathbf{A}$ ;  $n \geq 0$  is an integer number;  $\gamma$  is a constant that can be determined using an accurate approach. The contour integral is taken along the closed orbit of the electron in  $\mathbf{r}$ -space. Equation (4.13) determines allowed energy levels for the electrons in the applied magnetic field. The cyclotron motion is characterized by the frequency  $\Omega$  that relates electron's position  $\mathbf{r}$  and momentum  $\hbar \mathbf{k}$  with their derivatives:

$$\mathbf{v} = \Omega \times \mathbf{r}; \quad \Omega \times \hbar \mathbf{k} = \frac{e}{c} \mathbf{v} \times \mathbf{B}.$$

These equations allow to determine the cyclotron frequency and connect the cyclotron radius with the absolute value of the wave vector  $\mathbf{k}$ :

$$\Omega = \frac{eBv}{\hbar k}; \quad r = \frac{\hbar k}{eB}. \quad (4.14)$$

Since the energy depends on the absolute value of the wave vector only, the group velocity  $\mathbf{v} = \frac{\partial \varepsilon(\mathbf{k})}{\partial (\hbar \mathbf{k})}$  is parallel to the wave vector  $\mathbf{k}$ . Thus the integral (4.13) can be calculated as

$$\oint (\hbar \mathbf{k} - \frac{e}{c} \mathbf{A}) \, d\mathbf{r} = 2\pi r \hbar k - \frac{e}{c} B \pi r^2. \quad (4.15)$$

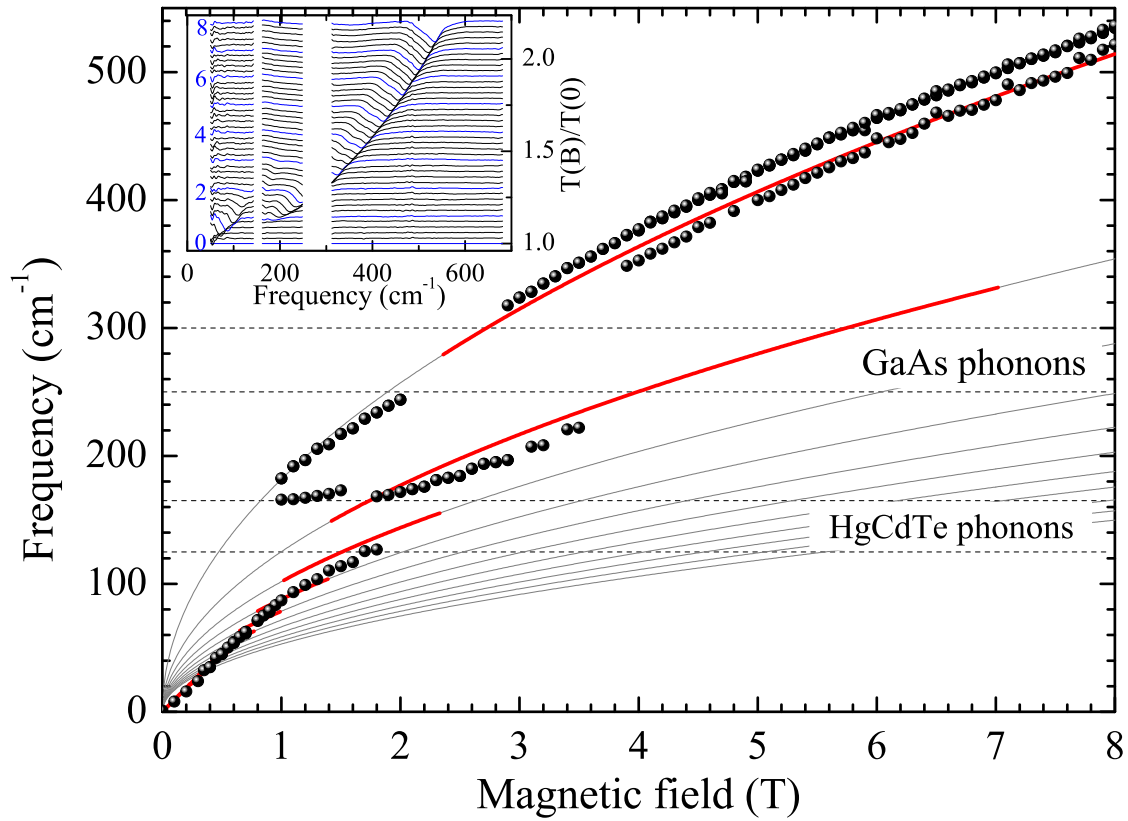


**Figure 4.8:** Far-infrared magneto-optical transmission spectra on the sample #3, obtained at 10 K. Black symbols – experimental absorption frequencies in the infrared transmission experiment. Solid gray lines show the energy difference  $\varepsilon_{n+1}(B) - \varepsilon_n(B)$ ,  $n = 0, 1, \dots, 10$  between the Landau levels. Red solid lines – calculated positions of the absorption frequencies as described in the text. The inset shows examples of the transmission spectra, normalized by the transmission in zero magnetic field. The curves are shifted for clarity.

Here the Stokes' theorem was used to obtain the second term. By combining Eqs. (4.13, 4.14, 4.15) one obtains the explicit expression for  $k_n$ :

$$k_n^2 = \frac{2eB}{c\hbar}(n + \gamma). \quad (4.16)$$

At low temperatures the Fermi-Dirac distribution degenerates into the Heaviside step-function. In zero magnetic field electrons occupy the states with the wave vectors lying inside the circle  $k < k_F$ . The electron density  $n_{2D}$  in this case is given by

$$n_{2D} = D \frac{k_F^2}{4\pi}, \quad (4.17)$$

where  $D = 1$ , if the spin is completely neglected, and  $D = 2$ , if we assume the spin degeneracy. When the magnetic field  $B$  is applied, the allowed electron levels are given by Eq. 4.16. Each new state  $|k_n\rangle$  can be approximately treated as a superposition of zero-field states  $|\mathbf{k}\rangle$  with the wave vectors  $|\mathbf{k}| \approx k_n$ . Since  $k_n^2 \propto n$ , the area of a ring between the levels  $n$  and  $n + 1$  is constant for any  $n$ . This reasoning illustrates, why the degeneracy of the Landau levels  $|k_n\rangle$  is independent on the number  $n$ . Formally, one can find the last occupied Landau level by resolving  $k_n = k_F$  that leads to

$$n = \frac{2\pi c\hbar}{DeB} n_{2D} - \gamma. \quad (4.18)$$

Since  $n$  must be integer, the resulting real number should be rounded to the next greater integer. If the level  $|n\rangle$  is partially filled, the electrons can transit from the level  $|n - 1\rangle$  or to the level  $|n + 1\rangle$ . The Bohr-Sommerfeld approximation is asymptotically accurate for large  $n \gg 1$ . According to Eq. 4.18, this limit is achieved in low magnetic fields. In this case a small change in  $B$  is enough to change the number of the last occupied Landau level. Thus the resonant energy can be approximately calculated as

$$\varepsilon_{n+1} - \varepsilon_n \approx \frac{\partial \varepsilon}{\partial n} = \frac{\partial \varepsilon}{\partial k} \frac{\partial k_n}{\partial n} = \frac{eB\varepsilon'}{c\hbar k_F}. \quad (4.19)$$

Equation 4.19 reproduces the results (3.23–3.24), obtained using the Boltzmann equation and the semi-classical equations of motion. In low magnetic fields the resonating levels switch in such a way, that the cyclotron frequency linearly increases with  $B$ , and the effective mass is determined by  $\varepsilon'(k_F)$ . In higher fields a small change in  $B$  does not necessarily change the number of the last level. If the energy dispersion is parabolic, then the Landau levels are equidistant and they are separated by the cyclotron energy  $\hbar eB/(mc)$ . Then even in the high fields the cyclotron frequency linearly increases with  $B$ .

In the case of the HgTe film with the critical thickness we expect the linear relation between the energy and the wave vector:

$$\varepsilon = \hbar v_F k. \quad (4.20)$$

According to Eq. 4.16, the energy of the Landau level  $n$  in this case takes the form

$$\varepsilon_n = v_F \sqrt{\frac{2e\hbar B}{c}}(n + \gamma). \quad (4.21)$$

In Ref. [55] the energy levels induced by the magnetic field were calculated by the method of Luttinger and Kohn (LK) [56], taking into account the large effects of band-to-band transitions, which are not included in the present consideration. The resulting expression for  $\varepsilon_n$  in LK method coincide with  $\varepsilon_n$ , calculated using Eq. 4.21 with  $\gamma = 0$ .

The linear dependence (4.19) is changed by separate transitions between the Landau levels in high magnetic fields. In figure 4.8 the low field behavior can be observed below 1 T, and the separate transitions reveal above 1 T. The gray curves show the frequencies, corresponding to transitions between the levels  $\varepsilon_n$  and  $\varepsilon_{n+1}$ , where  $n = 0, 1, \dots, 10$  and the energy is determined by Eq. 4.21 with  $n_{2D} = 8.5 \times 10^{10} \text{ cm}^{-2}$ ,  $v_F = 1.2 \times 10^8 \text{ cm/s}$ ,  $\gamma = 1/2$ . The red curves mark the transitions from the level  $n - 1$  and to the level  $n + 1$ , where  $n$  is determined by Eq. 4.18 with  $D = 1$ . The chosen set of parameters allows to achieve a semi-quantitative agreement between the experimental points and the red curves. However we cannot directly attribute these values to the properties of the band structure. The Bohr-Sommerfeld approximation is accurate only in small magnetic fields, when the number of the last occupied Landau level is large:  $n \gg 1$ . In high magnetic fields, when only a few Landau levels are occupied by electrons, the small gap in the band structure and Zeeman's splitting affect the positions of the resonances [51]. Thus the Bohr-Sommerfeld approximation serves as only a qualitative explanation for the high-field behavior.

If we stay within the model, defined by the linear dispersion (4.20), we can still determine the parameters of the band structure from the low-field data. The slope  $\partial\Omega/\partial B$  allows to determine the cyclotron mass as  $m_c = 0.01m_0$ . The electron density can be estimated by fitting the shape of the cyclotron resonance within the Drude model (section 4.3.3), which gives the value  $n_{2D} = 7 \times 10^{10} \text{ cm}^{-2}$ . Taking into account the spin degeneracy ( $D = 2$ ), we obtain the Fermi velocity as

$$v_F = \frac{\hbar}{m_c} \sqrt{\frac{4\pi n_{2D}}{D}} = 7.7 \times 10^7 \text{ cm/s}. \quad (4.22)$$

This value of the Fermi velocity is in a good agreement with the results of analogous experiments ( $v_F = 7.2 \times 10^7 \text{ cm/s}$ ) [37, 39] and of capacitance spectroscopy experiments ( $v_F = 8.2 \times 10^7 \text{ cm/s}$ ) [57].

### 4.3.7 Conclusion

Terahertz properties of the mercury telluride thin films with critical thickness are investigated. Using optical doping by visible light illumination, the charge carrier concentration could be modified by more than one order of magnitude. In some cases, using light as a parameter may switch the qualitative electrodynamic response from hole-like to the electron-like. Especially towards low electron density the cyclotron mass shows a square root dependence upon the charge concentration. This can be interpreted as a clear proof of a linear dispersion relations, i.e. Dirac type carriers.

## 4.4 Samples with Mylar gates

### 4.4.1 Preparation of gates

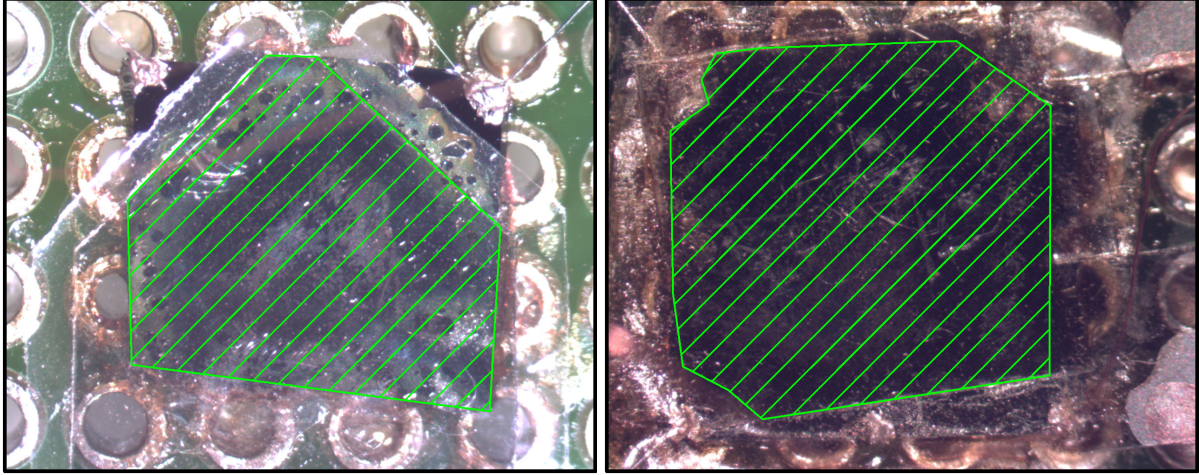


**Figure 4.9:** HgTe sample #1 (left image) with film thickness  $d = 6.6$  nm and sample #2 (right image) with  $d = 6.3$  nm. The green hatched area marks the semitransparent gate. Sample #1 has  $18.9 \text{ mm}^2$  gate area, sample #2 –  $24.8 \text{ mm}^2$ .

Mercury telluride quantum wells have been grown on (013) oriented GaAs substrates by molecular beam epitaxy as described in section 4.2. The results on two samples with thickness close to critical are presented: sample #1 with  $d = 6.3$  nm and sample #2 with  $d = 6.6$  nm. The gate on both samples has been prepared *ex-situ* using a mylar film with  $d = 6 \text{ }\mu\text{m}$  as an insulating barrier and a semi-transparent metalized film as a gate (Ti,  $R = 600 \text{ }\Omega/\square$ ). In the experiment the gate conductivity is seen as magnetic field independent and frequency independent contribution to  $\sigma_{xx}$ . No measurable effect of the gate on the Hall conductivity has been observed, which agrees well with the low mobility of the gate carriers.

Figure 4.9 shows the images of the samples. The semitransparent gates are made *ex-situ* as follows. First, a  $6 \text{ }\mu\text{m}$  thin Mylar foil is glued on the sample using “BF” glue (a phenol formaldehyde polyvinyl vinylite-based compound). Then, a Ti-coated Mylar foil is glued on the top of the isolating layer with the metalized side towards the sample. The sheet resistance of the metalized foil is around  $600 \text{ }\Omega/\square$ . Two contacts are made to both HgTe film and the gate to increase the reliability. The area of the gated region is measured on the images of the sample and is shown as a green hatched polygon in Fig. 4.9. The capacity between the gate and the HgTe film is measured using a high precision electrometer at effective frequencies between 1 and 10 Hz. The sample #2, which was prepared first, has  $A = 24.8 \text{ mm}^2$  area and  $C = 35.4 \text{ pF}$  capacitance. The parameters of the sample #1 are  $A = 18.9 \text{ mm}^2$  area and  $C = 59.5 \text{ pF}$  capacitance.

Knowledge of the capacitance allows to estimate the surface density of induced charge carriers  $n$  per unit of the applied gate voltage  $U$ . From  $Q = CU$  we have  $Q/(eAU) = n/U = C/(eA)$ . Here,  $e = 1.6 \times 10^{-19} \text{ C}$  is electron’s charge. For the sample #1 we have  $n/U \simeq 2 \times 10^9 \text{ cm}^{-2} \cdot \text{V}^{-1}$ , and  $n/U \simeq 9 \times 10^8 \text{ cm}^{-2} \cdot \text{V}^{-1}$  for sample #2. These values are

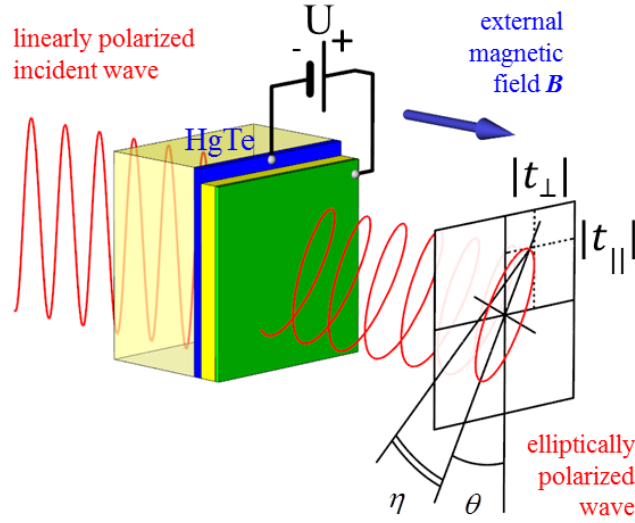


**Figure 4.10:** Schematic view of the magneto-optical experiment to measure the Faraday rotation  $\theta$  and ellipticity  $\eta$ . The definitions of both angles are depicted in the output polarization ellipse, assuming a linear incident polarization. The external magnetic field is applied in the Faraday geometry, i.e.  $\mathbf{B} \parallel \mathbf{k}$ . Complex transmission in parallel ( $t_{\parallel}$ ) and in crossed ( $t_{\perp}$ ) polarizers are measured which provide a full description of the transmission matrix.

close to the ideal expectation  $n/U = C/(eA) = \varepsilon\varepsilon_0/(ed) = 3 \times 10^9 \text{ cm}^{-2} \cdot \text{V}^{-1}$ , obtained in the plane capacitor approximation and neglecting the thicknesses of the glue layers. Here  $\varepsilon = 3.25$  is the static dielectric constant of Mylar and  $d = 6 \text{ }\mu\text{m}$  is the thickness of the insulating foil. Taking  $U_{\text{max}} = 500 \text{ V}$  as a maximal gate voltage, available in our setup, we get  $n = 10 \times 10^{11} \text{ cm}^{-2}$  for the sample #1 and  $n = 4.5 \times 10^{11} \text{ cm}^{-2}$  for the sample #2 as an upper limit of the change of the charge carrier density.

#### 4.4.2 Drude parameters

Drude parameters has been obtained from analysis of transmission coefficients, measured with the Mach-Zehnder interferometer. The main measurement mode was to fix the frequency of the generated radiation and to measure both the transmission amplitude and the phase difference of the transmitted signal as a function of the applied magnetic field and the gate voltage. Throughout section 4.4 transmission data are presented in the form of Faraday rotation angles  $\theta$  and  $\eta$ , see Fig. 4.10. These quantities allow a simple geometric interpretation in the case of the elliptical polarization and they are not as specific as the raw transmission coefficients. In order to determine both Faraday rotation angle  $\theta$  and ellipticity angle  $\eta$  two measurements are performed: one with the analyzer setting the same as the incident polarization (parallel polarizers geometry) and one with the analyzer rotated by  $90^\circ$  (crossed polarizers geometry). The Faraday angles are then calculated as

$$\theta = \frac{1}{2} \arctan \left( \frac{2|t_{\perp}||t_{\parallel}|\cos(\varphi_{\parallel} - \varphi_{\perp})}{|t_{\perp}|^2 - |t_{\parallel}|^2} \right); \quad (4.23)$$

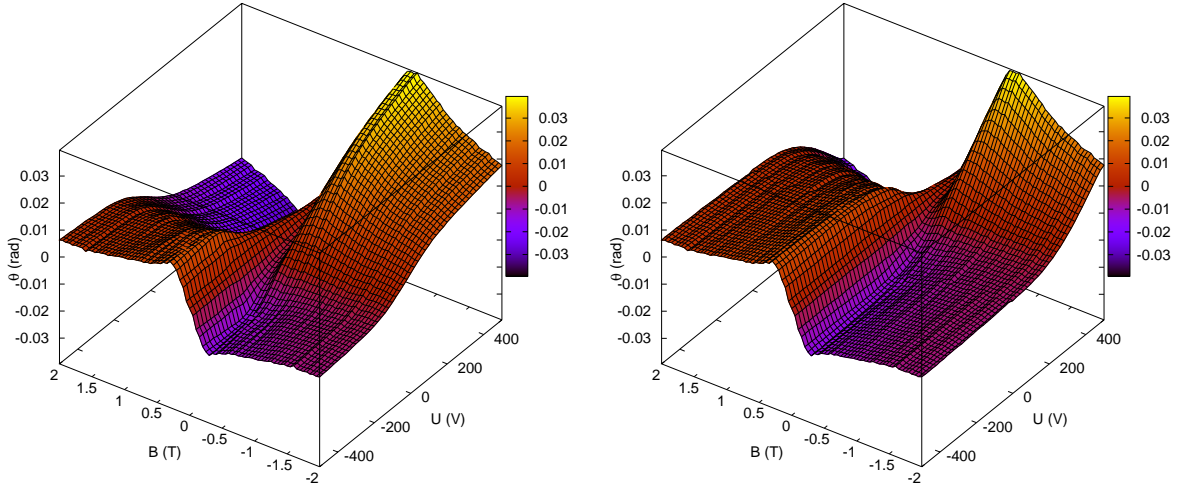


**Figure 4.11:** Faraday rotation angle  $\theta$  as a function of the applied magnetic field  $B$  and the gate voltage  $U$  for the sample #2. The left panel shows the data for increasing gate voltages, the right panel – for decreasing gate voltages.

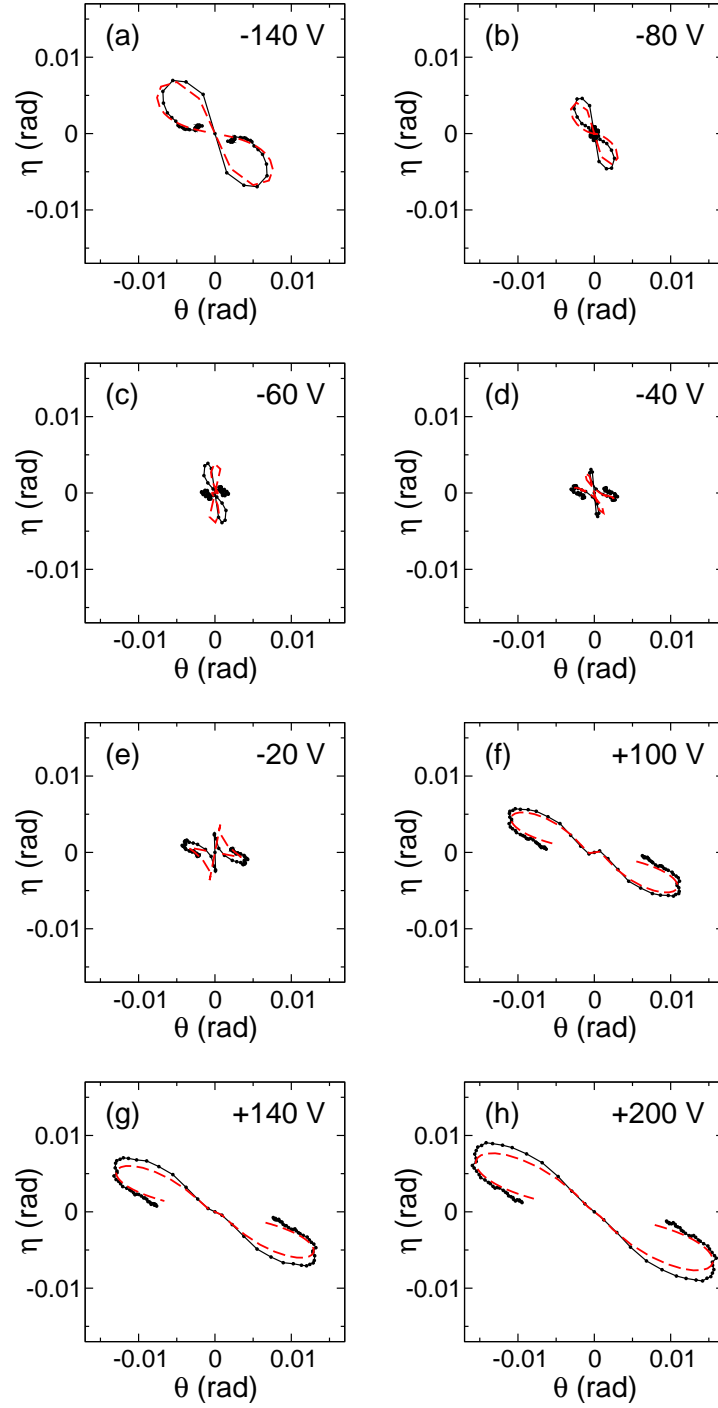
$$\eta = \frac{1}{2} \arcsin \left( \frac{2|t_{\perp}||t_{\parallel}|\sin(\varphi_{\parallel} - \varphi_{\perp})}{|t_{\perp}|^2 + |t_{\parallel}|^2} \right). \quad (4.24)$$

Figure 4.11 shows the overview of the Faraday angle  $\theta$  measured on the sample #2. The left panel presents the results for increasing gate voltages, the right panel – for decreasing gate voltages. The presence of the gate voltage hysteresis complicates the analysis of the data, and it is hard to avoid for the Mylar gates. One possible solution is to use some intrinsic parameter, for example the charge carrier density instead of the gate voltage. Such analysis is presented below, where the charge density is determined from the experimental data by the fits within the Drude model.

The main features in Fig. 4.11 are the cyclotron resonances, seen as peaks in the Faraday angle  $\theta$  at low magnetic fields  $< 0.5$  T. The resonances in  $\theta(B)$  are antisymmetric with respect to the field. The fact that the positive and negative peaks interchange with each other as the gate voltage is swept shows the change of the sign of the dominant charge carriers in the sample. At the intermediate gate voltages a double peak structure can be seen, with both positive and negative small peaks on one side from zero magnetic field. This feature points towards the presence of both hole-like and electron-like charge carriers at the same time. Such a semi-metallic behavior could be not only due to the intrinsic features of the band structure of the HgTe films, but also due to the inhomogeneity of the *ex-situ* gate. In the data analysis within the Drude model we have used two charge carriers with opposite signs to fit the region of the intermediate gate voltages.

Figure 4.12 shows the examples of Drude fits for the sample #1. The data is presented in the form of the Faraday rotation angle  $\theta$  and the ellipticity angle  $\eta$  and is plotted in the  $\theta\eta$ -plane. The external magnetic field is the hidden parameter of the curves. The experimental data is shown by black solid symbols, joined by the solid lines, and the theoretical Drude curves are shown by red dashed lines. The cyclotron resonance is seen as the lobes of the





**Figure 4.12:** Faraday rotation  $\theta$  and ellipticity  $\eta$  plotted in the  $\theta\eta$ -plane as a function of the external magnetic field  $-2\text{ T} \leq B \leq +2\text{ T}$  for the sample #1. A continuous transition from the hole-like charge carriers (panel (a),  $-140\text{ V}$  gate voltage) to the electron-like carriers (panel (h),  $200\text{ V}$ ) is seen as an inversion of the eight-shaped curve. Black symbols with solid lines are experimental data, red dashed lines are fits within two carriers Drude model.



curve with both angles approaching zero as the magnetic field goes to zero or to infinity. The magnetic field is positive for one lobe and is negative for the other. In the hole-like region of gate voltages the curve has a distinct eight-like shape, see Fig. 4.12(a). As the gate voltage increases, the curve shrinks (panel (b)). At some gate voltage, another eight-like shaped curve emerges, superimposed with the first curve (panel (c)). In the narrow range of gate voltages both the hole-like and electron-like responses coexist with the hole-like response shrinking and the electron-like growing (panels (d)–(e)). At even higher gate voltages the electron-like curve dominates, but the hole-like response is still visible as a kink around zero magnetic field (panels (f)–(g)). Finally, only a single eight-like shaped curve is present in the electron region of the gate voltages (panel (h)). The polarity of the magnetic field in panel (h) is reversed with respect to the hole-like curve in panel (a).

The parameters of the charge carriers, resulted from the analysis of the data within the Drude model, are shown in Fig. 4.13. The left panels show the data for the sample #1, the right panels – for the sample #2. The upper panels (a) and (b) show the charge densities of holes  $p$  (open triangles) and of electrons  $n$  (solid triangles) as a function of the film voltage. The up and down triangles correspond to the increasing and decreasing voltage, respectively. The gate voltage hysteresis is clearly visible. In order to workaround this complication, the density of the charge carriers ( $n$  or  $p$ ) was chosen as an independent parameter with all other parameters being the function of it. It is desirable to obtain the properties of electrons and holes independently, therefore all other parameters of charge carriers are plotted as functions of respective charge densities:  $p$  for the properties of the holes and  $n$  for the properties of electrons. It should be noted that for the integral properties like the Faraday angles the total charge density ( $p - n$ ) is more appropriate, as it characterizes the sample as a whole. Such total charge densities are shown in Fig. 4.13 as solid black lines for the increasing voltages and as dashed gray lines for the decreasing voltages. The panels (c) and (d) show the density dependence of the dimensionless two-dimensional static conductivity  $\sigma Z_0$ , where  $Z_0 = 1/(\epsilon_0 c) \approx 377 \text{ Ohm}$  is the impedance of free space and  $\sigma = ne^2\tau/m$ . First, it is noticeable that the data for increasing and decreasing gate voltages coincide almost perfectly, justifying the choice of the density as the independent variable. The curves are almost linear, indicating that the mobility of the carriers  $\mu = \sigma/(en) = e\tau/m$  is roughly constant across the investigated density range. The experimentally determined mobility is shown in panels (e) and (f). It is indeed approximately constant with some increase towards low carrier densities. This increase of  $\mu$  is mostly not due to the increase of the relaxation time  $\tau$ , but due to the decrease of the cyclotron mass  $m$ , which is shown in panels (g) and (h). The cyclotron mass data is more noisy than other parameters, especially at low charge densities. The cyclotron mass is mostly responsible for the position  $B_c$  of the cyclotron resonance peak. At low densities these cyclotron peaks become quite weak and they are hard to separate in positive and negative magnetic fields. Contrary to the conductivity and mobility data, the cyclotron mass still shows some discrepancy between the increasing and decreasing gate voltages. While the difference for the sample #1 is almost within the experimental uncertainty level, the difference for the sample #2 grows up to 30–40 % at low densities. These complications lead to the increasing experimental error in the low-density range. On the other hand, the direct determination of the cyclotron mass is quite valuable. The transport measurement are only able to determine the mass indirectly, for example from the temperature dependence of the amplitude of the Shubnikov-de-Haas

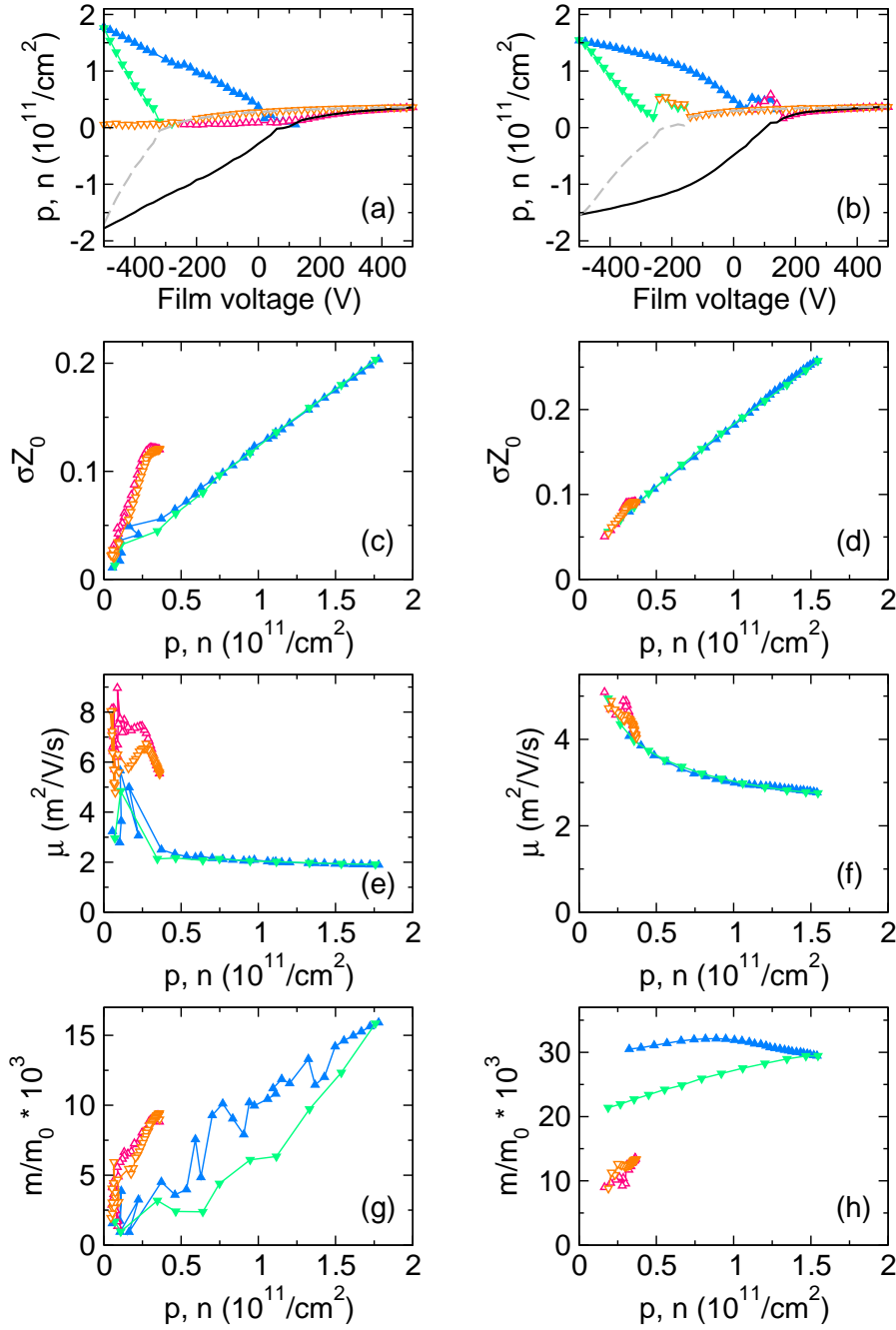


**Figure 4.13:** Drude fit parameters of the charge carriers for the sample #1 (left panels (a), (c), (e) and (g)) and the sample #2 (right panels (b), (d), (f) and (h)). Blue solid up triangles are for the electron properties in increasing film voltage, red open up triangles denote the holes properties in increasing voltage, green down triangles show the properties of the electrons in decreasing voltage and the orange open down triangles stand for the properties of the holes in decreasing voltage. The upper panels (a) and (b) show the film voltage dependence of the holes  $p$  and electrons  $n$  density (the film voltage is connected to the gate voltage as  $V = -U$ ). The black solid and dashed gray lines show the total charge density ( $p - n$ ) for increasing and decreasing film voltages, respectively. The panels (c) and (d) demonstrate the dimensionless 2D-conductivity  $\sigma Z_0$  as a function of the respective charge density  $p$  or  $n$ . The dependence of the mobility  $\mu$  on the density is shown in panels (e) and (f). The panels (g) and (h) represent the charge density dependence of the cyclotron mass  $m$  normalized to the free electron mass  $m_0$ .

oscillations.

### 4.4.3 Band structure reconstruction

The cyclotron mass data in Fig. 4.13(g, h) shows a qualitative difference between the samples #1 and #2. Namely, while the mass of electrons for the sample #1 is decreasing towards zero at low densities, the electron mass in the sample #2 is only slightly decreasing towards some finite value. These features allow to suggest that the electron band dispersion in the sample #1 is mostly linear whereas the dispersion in the sample #2 is dominated by the quadratic term. With all the data at hand it is possible to reconstruct at least a part of the band structure of the investigated samples under the assumption of the isotropic band dispersion  $E = E(|\mathbf{k}|)$ . Indeed, the charge carrier density in the isotropic two-dimensional case is  $n = \pi k^2 D / (2\pi)^2$ , where  $k$  is the Fermi wave vector and  $D$  is the degeneracy of the states. We are assuming spin degenerate nature of charge carriers in our samples, so  $D = 2$ . This allows us to obtain the Fermi wave vector  $k$  directly from the experimental density  $n$ :  $k = \sqrt{2\pi n}$ . From the definition of the cyclotron mass (Eq. 3.23) we obtain

$$\frac{\partial E}{\partial k} = \frac{\hbar^2 k}{m}. \quad (4.25)$$

Figure 4.14 shows the consecutive steps, needed to obtain the experimental band structure. The left panels show the data for the sample #1 and the right panels show the data for the sample #2. The upper panels (a) and (b) show the inverse cyclotron mass normalized to the free electron mass as a function of Fermi wave vector  $k$ . The middle panels (c) and (d) demonstrate the derivative  $\frac{\partial E}{\partial k}$ . The band structure dispersion  $E(k)$  can be obtained by a numerical integration of the experimental curves in (c) and (d). The result of the integration is shown in the lower panels (e) and (f). The dispersions of holes in both samples are linear in  $k$ . They were fitted with linear functions, shown in panels (e) and (f) by solid red and orange lines for increasing and decreasing film voltages, respectively. The dispersion of the electron-like charge carriers in the sample #1 is also close to linear with some small non-monotonic deviations, see Fig. 4.14(e). The blue and green solid lines are purely linear fits of the experimental dispersions, showing a rather good agreement. On the contrary, the sample #2 demonstrates a monotonic positive curvature of the electron-like dispersion curves. For this reason, the fits (blue and green lines in panel (f)) include both linear and quadratic terms. Here, for increasing film voltages (blue solid up triangles and blue line in panel (f)) the quadratic term is dominant in the dispersion curve, whereas for decreasing film voltages (green solid down triangles and green line in panel (f)) both linear and quadratic terms contribute roughly equal to the total dispersion relation. Such a difference between two samples might be understood taking the different HgTe film thicknesses into account. The mercury telluride film in the sample #1 has a thickness of 6.6 nm, which is assumed to be closer to the critical film thickness  $d_c$ , at which the gap is zero and a pure linear dispersion is realized. The film in the sample #2 is thinner (6.3 nm) and the gap is assumed to be positive, revealing the quadratic dispersion of the electrons. This picture lacks an explanation for the linear dispersion of holes in the sample #2.

The integration procedure leaves an arbitrary additive constant in the dispersion relation. Here the constants are chosen in such a way that all linear fits in the panel (e) and both the

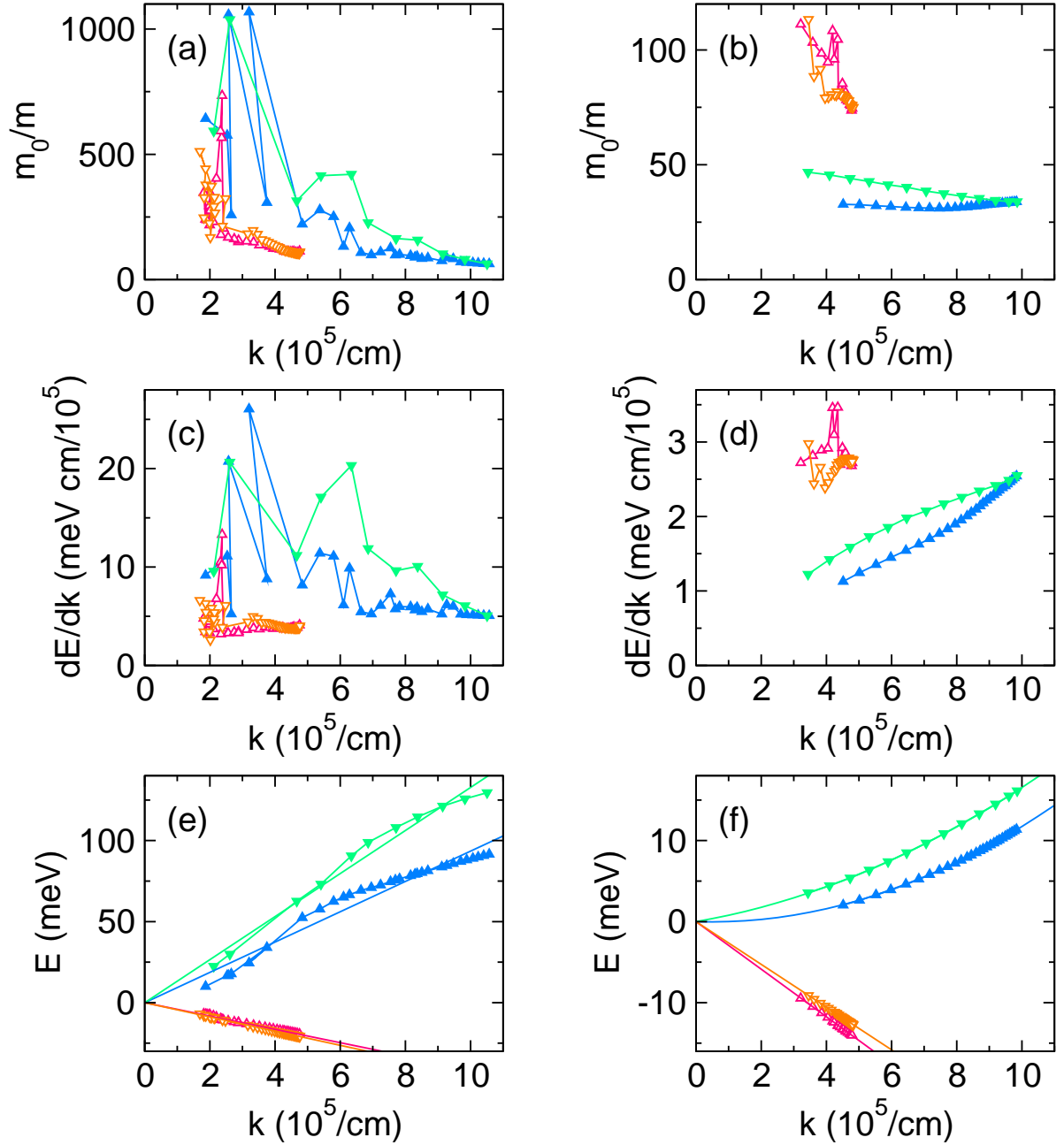


**Figure 4.14:** Experimental determination of the band structure of thin HgTe films. The left panels (a), (c) and (e) show the data for the sample #1, the right panels (b), (d) and (f) are for the sample #2. The upper panels (a) and (b) show the inverse cyclotron mass, normalized by the free electron mass, as a function of the Fermi wave vector  $k$ . The middle panels (c) and (d) show the derivative  $\frac{\partial E}{\partial k}$ , derived from the cyclotron mass data. The lower panels (e) and (f) show the reconstructed band dispersions. The solid blue up triangles are for the electrons in increasing film voltages, the solid green down triangles show the properties of the electrons in decreasing film voltages. The open red up triangles denote the holes in increasing film voltages and the open orange down triangles demonstrate the properties of the holes in decreasing film voltages. The solid lines in panel (e) are linear fits of the experimental dispersion. The red and orange lines in panel (f) are linear fits of the dispersion of the holes and blue and green lines in panel (f) are fits of the electronic part of the band structure, containing both linear and quadratic terms.

linear and quadratic fits in the panel (f) cross at zero energy and zero wave vector. Such a crossing is expected for the linear dispersion, which is probably the case for sample #1, see panel (e). As for the sample #2 (panel (f)) with the noticeable quadratic term in the electronic part of the band diagram, one can expect the presence of a nonzero gap. In this case further experiments, for example involving elevated temperatures, are needed to establish a reliable experimental value of the gap.

#### 4.4.4 Universal Faraday rotation

Thus far we have analyzed the spectroscopic data within the semi-classical picture. In this section we focus on a phenomenon that directly demonstrates the quantum nature of the charge carriers. In the dynamical regime the unusual character of the quantum Hall effect in systems with Dirac cones can be shown [28, 30, 31, 58] to lead to universal values of the Faraday and Kerr rotation with  $\theta_F = \alpha \approx 1/137$  and  $\theta_K = \pi/2$ , respectively. Such predictions have been recently confirmed experimentally in graphene [59], where the Faraday angle is additionally doubled as two Dirac cones exist in the Brillouin zone. Very recently [60, 61], several groups announced the observation of the quantized Faraday and Kerr rotation from the surface states of bismuth compounds. Compared to thick strained films with three-dimensional (3D) carriers, in HgTe wells with critical thickness a two-dimensional electron gas is realized. In this case the quantized Faraday rotation is directly connected to the quantization of the dynamic Hall conductivity [62].

Explicit equations to calculate the conductivity tensor from the measured transmission are given by Eq. 2.15. In these calculations the effect of GaAs substrate and of Ti gate are taken into account exactly, i.e. pure two-dimensional conductivity of the layer “HgTe+gate” is obtained. The measured Faraday rotation and ellipticity are still partly influenced by the properties of the substrate and the gate. Where appropriate, specific values of these angles will be given. The frequency of the THz radiation in the transmission experiments is chosen to minimize the influence of the substrate.

The most important result is demonstrated in Fig. 4.15. Here, the experimental Faraday rotation  $\theta$  (lower panel) and ellipticity  $\eta$  (upper panel) are shown for the sample #1. The peaks in the data at around  $B \approx 0.5$  T are the cyclotron resonances in the two-dimensional electron system. The sign change of the Faraday angle and ellipticity between negative and positive gate voltages corresponds to the transition from the hole-like to the electron-like carriers, respectively. In high magnetic fields far above the cyclotron resonance [64], classical Faraday rotation and ellipticity are expected to fade out as  $\theta \propto 1/B$ ,  $\eta \propto 1/B^2$ . Remarkably, in Fig. 4.15 the experimental value of the Faraday rotation for zero and negative gate voltages saturates at fields above 1 T and stays constant within the experimental accuracy up to the highest experimental field (7 T). Similar broad steps in the quantum Hall resistivity have been recently observed in HgTe wells and attributed to heavy holes valleys reservoir effects [65]. The step in Faraday rotation reveals a universal value close to the fine structure constant  $\alpha = \frac{Z_0}{2} \frac{e^2}{h}$ , indicated in Fig. 4.15 by dashed lines. Dash-dotted line gives the value which takes into account the properties of the substrate and gate exactly [63], and assuming  $\sigma_{xy} = e^2/h$ ,  $\sigma_{xx} = 0$ . The difference between both values of Faraday rotation and the experimental data are within the uncertainties of the experiment.

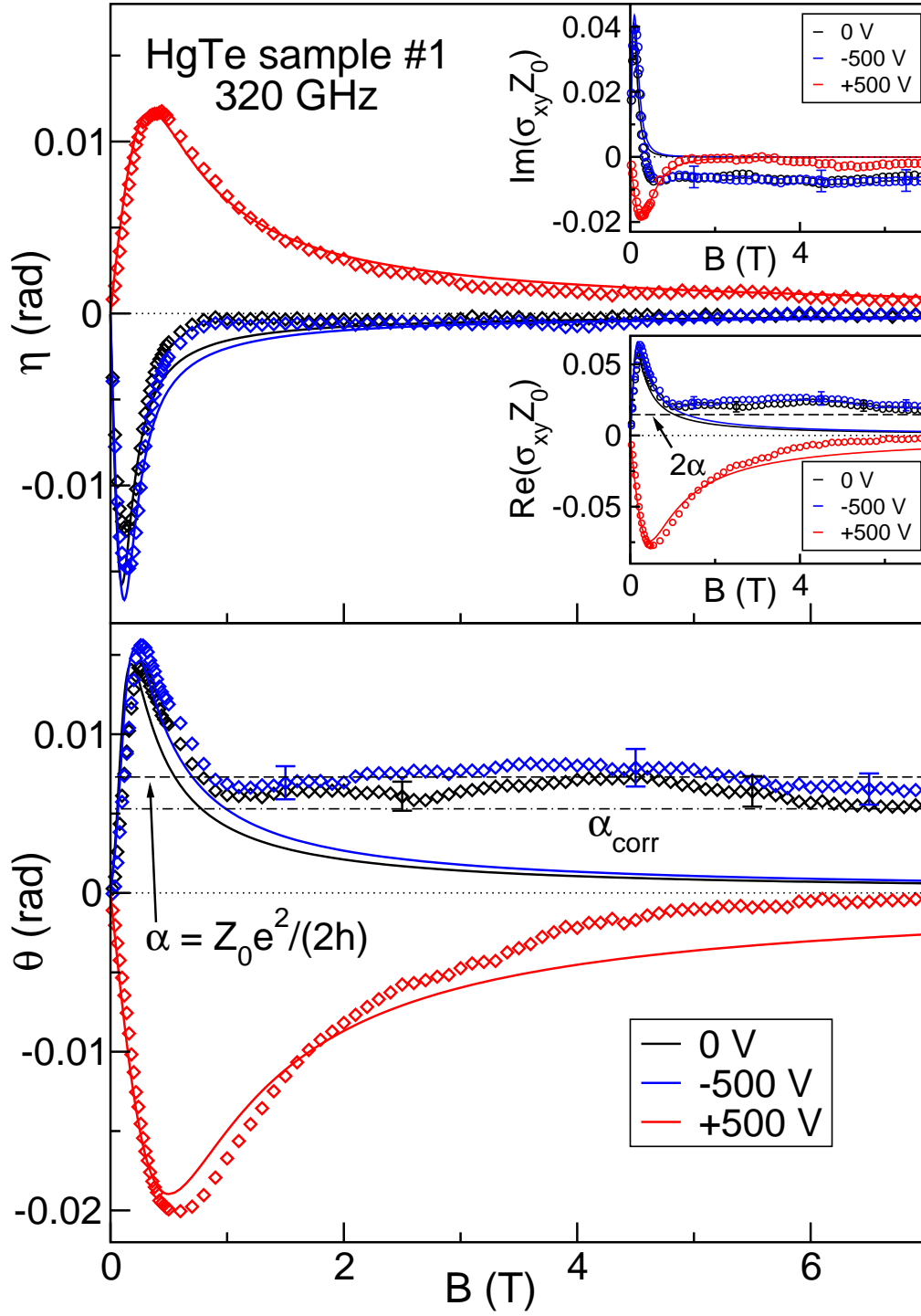


**Figure 4.15:** Magnetic field dependence of the Faraday rotation  $\theta$  (lower panel) and ellipticity  $\eta$  (upper panel) for the sample #1 for three characteristic gate voltages. Experimental data are shown by solid symbols and the lines are fits within the Drude model [29, 31]. Dashed line shows a “pure” universal value of Faraday rotation  $\alpha \approx 1/137$  rad. Dash-dotted line gives the real value of the rotation  $\alpha_{\text{corr}}$  taking into account the influence of the substrate and gate, and assuming  $\sigma_{xy} = e^2/h$ . The inset shows the off-diagonal conductivity  $\sigma_{xy}$  as directly obtained from the spectra using exact expressions for magneto-optical transmission [63].

**Table 4.1:** Drude parameters of the charge carriers in HgTe sample #1 as obtained from the fits of magneto-optical conductivity: density  $n_{2D}$ , effective mass  $m/m_0$ , and mobility  $\mu$ . The gate voltage  $-500$  V corresponds to hole carriers, and  $+500$  V to electrons, respectively.  $m_0$  is the free electron mass.

Gate (V)	$n_{2D}(\text{cm}^{-2})$	$m/m_0$	$\mu (\text{cm}^2/(\text{V}\cdot\text{s}))$
-500 V	$(3.3 \pm 0.5) \times 10^{10}$	$(7.5 \pm 1) \times 10^{-3}$	$(6.6 \pm 1.0) \times 10^4$
+500 V	$(1.4 \pm 0.3) \times 10^{11}$	$(9.2 \pm 1) \times 10^{-3}$	$(2.0 \pm 0.2) \times 10^4$

In order to demonstrate the discrepancy between the experimental data and classical cyclotron resonance, the fits within Drude model are shown as solid lines in Fig. 4.15. The Faraday rotation  $\theta$  and the Faraday ellipticity  $\eta$  of the electron-like carriers at positive gate voltage are well fitted within the classical response (red lines and symbols). The ellipticity at zero and negative gate voltages also follows the classical Drude model quite well. Remarkably, the experimental Faraday rotation in this region of the gate voltages behaves very distinctly from the predictions of the model. The model curves tend towards zero rather quickly at fields above 1 T (blue and black lines). Contrary, the experimental data shows abrupt deviation from the classical calculations at these fields, saturating at approximately constant level.

From the transmission spectra in zero magnetic field and at zero gate voltage the exact value of the refractive index of the substrate (optical thickness) is determined experimentally [45]. With this parameter the transmission in both parallel and crossed geometries can be recalculated into the complex magneto-optical conductivity of mercury telluride [63] without additional assumptions. The diagonal conductivity  $\sigma_{xx}$  is mostly responsible for the parallel transmission in our experiments and for the dissipation in DC transport measurements. The off-diagonal conductivity  $\sigma_{xy}$  is related to the transmission in the crossed geometry and for the quantum Hall plateaus in the DC experiments.  $\sigma_{xy}$  is especially relevant for the emergence of the universal Faraday rotation  $\alpha$  and it is plotted in the inset of Fig. 4.15. The data are shown in a dimensionless form by multiplying the conductivity  $\sigma$  with the impedance of vacuum  $Z_0 \approx 377 \text{ Ohm}$ .

The upper inset in Fig. 4.15 shows the imaginary part of  $\sigma_{xy}$ , which appears at nonzero frequencies only. The real part of  $\sigma_{xy}$  is shown in the lower inset. It also demonstrates the deviation from the classical Drude behavior and saturates at the level slightly above the universal value of  $Z_0 \frac{e^2}{h} = 2\alpha$ . We attribute this deviation to the uncertainties of the experiment.

From the Drude fits of the dynamic conductivity of the sample #1 in the vicinity of cyclotron resonance the parameters of the charge carriers could be calculated which are given in Tab. 4.1. Much lower mobility of the electrons ( $+500$  V) compared to holes ( $-500$  V) is probably the reason that no quantized Faraday effect could be observed for positive voltages. High Dirac-hole mobility in HgTe wells can be explained by screening of their scattering by heavy holes [66].

At a fixed frequency of the incident radiation  $f = 320 \text{ GHz}$  and at  $T = 1.8 \text{ K}$  there are two external parameters which can be tuned: magnetic field and gate voltage. A good overview

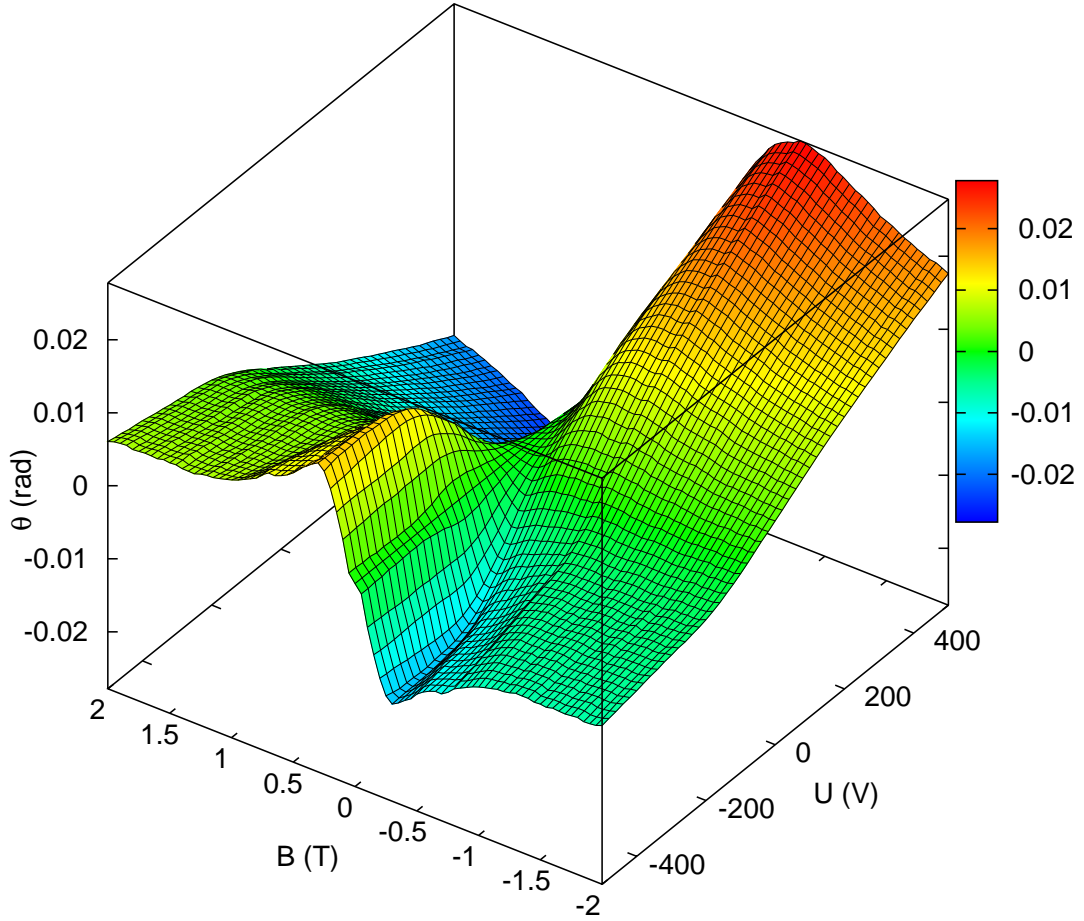


**Figure 4.16:** Faraday rotation  $\theta$  of the HgTe quantum well #1 as function of gate voltage and magnetic field. The values of  $\theta$  are colour-coded for clarity. The data are given for the increasing gate voltage from -500 V to +500 V as applied to the gate electrode. The maximum and minimum of  $\theta$  at low magnetic fields are the manifestations of the cyclotron resonance. The inversion from maximum to minimum reflects the transition from the hole-like charge carriers at negative gate voltages to the electron-like charge carriers at positive voltages.



of the experimental data set obtained by changing both parameters is provided by Fig. 4.16. Here, the color coded height represents the Faraday rotation  $\theta$  as a function of magnetic field  $-2 \text{ T} < B < 2 \text{ T}$  and of gate voltage  $-500 \text{ V} < U < 500 \text{ V}$  in the direction of increasing voltage. The data shown in Fig. 4.15 are cuts of the parametric surface in Fig. 4.16 at fixed gate voltages. The cyclotron resonance peaks in Fig. 4.15 are also seen in Fig. 4.16. However, now it is possible to see the continuous evolution of the cyclotron resonances with the gate voltage. The positive peak at positive magnetic fields and gate voltage of  $-500 \text{ V}$  gradually disappears and transforms into a negative peak at  $+500 \text{ V}$ . This is a manifestation of the transition from the hole-like carriers at negative gate voltages to the electron-like carriers at the positive gates.

The plateau in Faraday rotation close to the universal value  $\theta = \alpha$ , was reproduced in the measurements on the sample #2. Eight contacts have been prepared around the edges of the sample #2, which allowed to measure DC longitudinal and transverse resistivities  $R_{xx}$  and  $R_{xy}$ . These data are shown in the upper inset of Fig. 4.17. The black curve is the longitudinal resistivity  $R_{xx}$ , the red curve represents the transverse resistivity  $R_{xy}$ . The pronounced plateau at fields between 0.75 and 1.5 T is clearly seen in the  $R_{xy}$  data. The value of the transverse resistivity at the plateau is around 25.8 k $\Omega$ . The DC data correspond well to the universal value of the Faraday rotation  $\theta = \alpha$ . Indeed, in the limit of small absorption by thin film [64] we may write:  $\theta \sim t_{\perp}/t_{\parallel} \sim t_{\perp} \sim Z_0/2R_{xy}$ , which leads to  $\theta = \alpha$  for  $R_{xy} = h/e^2$ . Direct correspondence between the quantum Hall effect and quantized Faraday rotation is well known in ordinary 2D electron gases [62].

The magneto-optical conductivity of the sample #2 is shown in Fig. 4.17. The imaginary part in the upper panel reveals no plateau neither at the positive nor at the negative gate voltages. The real part of the conductivity, shown in the lower panel, demonstrates a clear plateau at fields above 1 T at zero and negative gate voltages. The value of this plateau equals to  $\sigma_{xy}Z_0 = 2\alpha = Z_0e^2/h$  and it corresponds well to the DC data shown by green line. In the electron-like doping regime at the positive gate voltages no such plateau is observed in magnetic fields below 2 T.

In conclusion, using polarization- and phase-sensitive terahertz transmission spectroscopy, HgTe quantum wells with critical thickness have been investigated. In external magnetic fields a universal value of the Faraday rotation close to the fine structure constant  $\theta_F = \alpha \approx 1/137$  is observed for hole-like carriers. Dynamic Hall conductivity is directly calculated from the experiment and it reveals a universal value  $\sigma_{xy} = e^2/h$ . The universal steps in the dynamical conductivity and Faraday angle remain robust in a broad range of external magnetic fields and gate voltages. On the electronic side of the gate voltages a classical magneto-optical behavior is observed. It can be attributed to much lower mobility of the negatively charged carriers. The observation of the quantization at frequencies above 300 GHz in the HgTe/CdHgTe quantum wells makes these systems a very promising object for the study of the dynamic quantum Hall effect. As we will see in section 5, the QHE is suppressed at lower frequencies in GaAs/AlGaAs heterojunctions. Further experiments are needed to understand these properties of the dynamic Hall conductivity in two-dimensional systems.

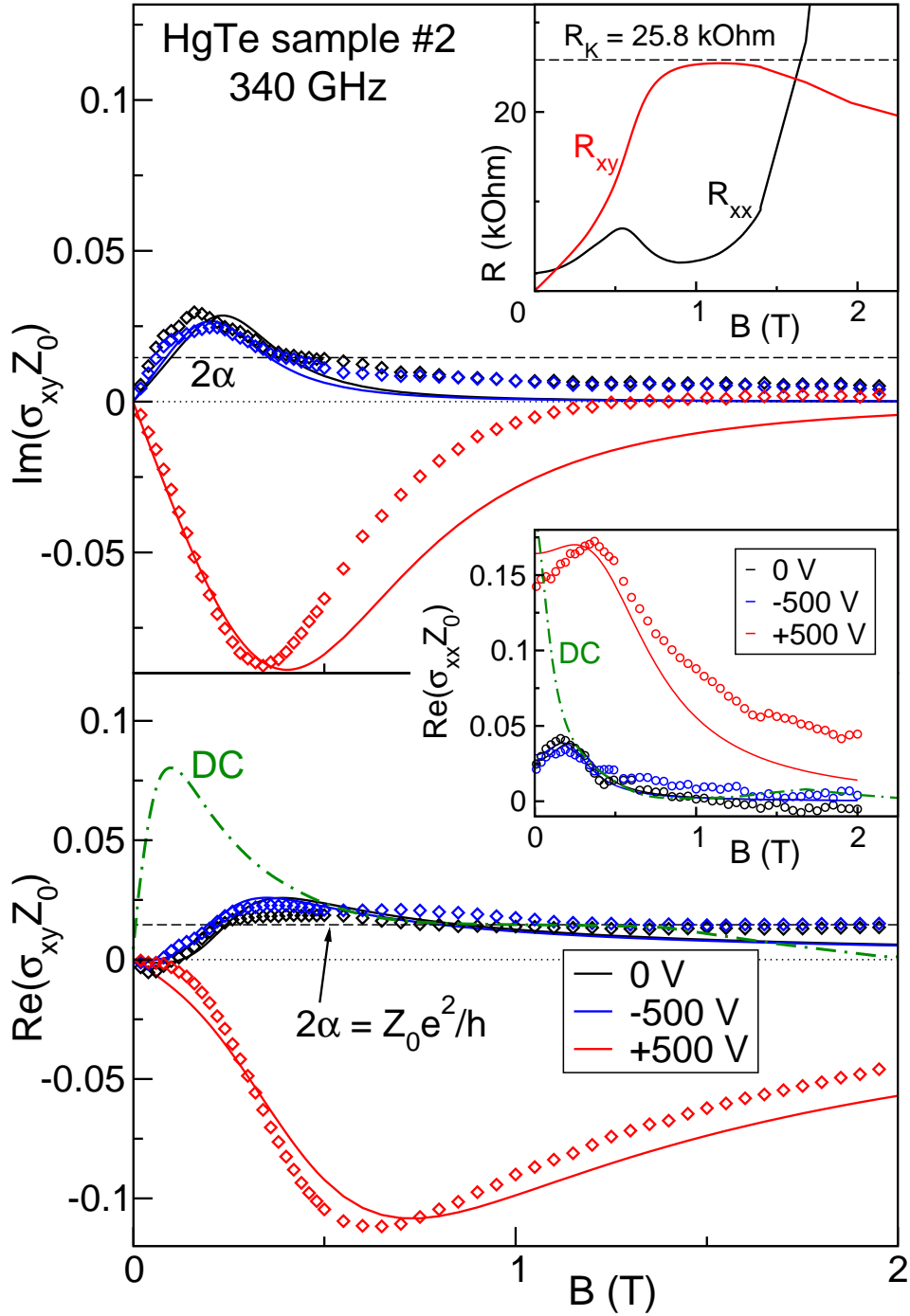


**Figure 4.17:** Magnetic field dependence of the off-diagonal conductivity  $\sigma_{xy}$  for the sample #2 at different gate voltages. Symbols represent experimental data, lines are fits using the Drude model. Green dash-dotted line shows the conductivity calculated from the DC data. Black dashed lines show the universal value of conductivity  $2\alpha$ . Upper inset shows the DC longitudinal and Hall resistivity measured on the same sample. The divergence of  $R_{xx}$  in high magnetic fields is due to a field-induced transition to the insulating state. Lower inset shows the diagonal dynamic conductivity  $\sigma_{xx}$  with the Drude fit and DC data represented as solid and dash-dotted lines, respectively. The maximum in  $\sigma_{xx}$  close to 0.2 T corresponds to the cyclotron resonance.

# 5 Dynamic QHE in GaAs/AlGaAs heterojunctions

## 5.1 Introduction to the dynamic quantum Hall effect

The discovery of the integer quantum Hall effect (IQHE) [67] has attracted much interest in scientific community. A vast majority of experimental and theoretical investigations is devoted to the study of the QHE at frequencies below 100 Hz, and in this range the phenomenon of Hall quantization has been studied very extensively. Only a few experimental attempts have been made in determining the highest frequency, at which the quantum plateaus are still observable. As the frequency increases up to GHz range, standard contact techniques become inapplicable. In this case, the high-frequency Hall conductivity can be studied by means of interaction of electromagnetic waves with a two-dimensional electron gas (2DEG). Kuchar *et al.* [8] used a crossed waveguide setup to observe Hall quantization at 33 GHz, Galchenkov *et al.* [9] used a circular waveguide to study evolution of the Hall plateaus in 24–70 GHz range. Further frequency increase can be achieved in quasi-optical spectrometers, suitable for measurements in the range 100–1000 GHz. In the case of a thin conducting film the Hall conductivity is directly connected to the Faraday rotation angle [62]. Recent experimental works [59, 61, 68, 69] on observation of the quantized Faraday rotation in novel materials have inspired a development of theories of a non-linear Hall response [70, 71]. On the other hand, a linear high-frequency Hall response is far from being completely understood for the systems with parabolic electron bands (AlGaAs, Si, Ge). Experimentally, the Hall effect in THz range was observed in GaAs/AlGaAs heterojunctions [72, 73] and Ge quantum wells [74]. The high-frequency data in Refs. [72–74] do not demonstrate quantum plateaus that would be comparable with corresponding DC data. In Ref. [73] the experiment was conducted at two frequencies (2.52 and 3.14 THz), using an optically pumped molecular gas laser. In Refs. [72, 74] the Hall conductivity was measured with a use of time-domain spectroscopy (TDS). Although in principle, TDS allows to obtain the Hall conductivity at fixed frequencies, the authors present the data, averaged over a wide spectral range. Due to this averaging, information about the frequency dependence of the Hall conductivity is lost. Thus, the question, how the static QHE transforms into dynamic one, remained unresolved.

In order to study the evolution of quantum Hall plateaus with frequency, we carried out a series of experiments on MBE-grown GaAs/AlGaAs heterojunctions, one of the most suitable system to investigate the DC QHE. We were able to reproduce the results of the crossed-waveguide method [8, 9] and to observe a plateau at 69 GHz. Above 100 GHz the plateaus are replaced by oscillations in the Hall conductivity, which disappear completely as the frequency is approaching 1 THz.

**Table 5.1:** Parameters of GaAs/AlGaAs heterostructures at  $T = 1.9$  K.  $n_{2D}$ : density,  $\mu$ : mobility,  $\tau$ : relaxation time,  $m$ : cyclotron mass, size: dimensions of the substrate. The superscripts DC and THz denote the quantities, independently obtained in contact and spectroscopic experiments respectively.

	Sample #1	Sample #2
$n_{2D}^{\text{DC}} (\text{cm}^{-2})$	$(2.3 \pm 0.2) \times 10^{11}$	$(3.6 \pm 0.3) \times 10^{11}$
$n_{2D}^{\text{THz}} (\text{cm}^{-2})$	$(2.4 \pm 0.2) \times 10^{11}$	$(3.9 \pm 0.8) \times 10^{11}$
$\mu^{\text{DC}} (\text{cm}^2/(\text{V}\cdot\text{s}))$	$(1.0 \pm 0.1) \times 10^5$	$(3.2 \pm 0.5) \times 10^5$
$\mu^{\text{THz}} (\text{cm}^2/(\text{V}\cdot\text{s}))$	$(1.1 \pm 0.1) \times 10^5$	$(2.5 \pm 0.5) \times 10^5$
$\tau$ (ps)	$4.5 \pm 0.5$	$10 \pm 2$
$m/m_0$	$0.070 \pm 0.001$	$0.070 \pm 0.002$
Size ( $\text{mm}^3$ )	$10 \times 10 \times 0.660$	$5 \times 5 \times 0.367$

## 5.2 Samples

The presented experimental data have been obtained on two GaAs/AlGaAs heterojunctions, grown by molecular beam epitaxy, see Fig. 5.1(a). Characteristic parameters of the samples, obtained in DC and spectroscopic experiments at 1.9 K, are given in Tab. 5.1. The sample #1 (marked as C0456) has a reduced silicon delta doping level in comparison with the sample #2 (marked as K035), which led to a lower electron density and a shorter relaxation time. Larger dimensions of the sample #1 allowed to extend spectroscopic measurements below 100 GHz. Insulating GaAs, used as a substrate, is transparent for the radiation in the full range of the spectrometer. The substrate is characterized by a dielectric constant  $\varepsilon = 12$  with a negligible frequency dependence. Indium electrical contacts, placed in corners and centers of sides, were prepared on each sample by baking at 400 °C in a reducing atmosphere (Ar+4%H). All spectroscopic experiments were accompanied by simultaneous measurements of resistances  $R_{xx}$  and  $R_{xy}$  using lock-in techniques, see Fig. 5.1(b). Typical values of the applied current were  $I \approx 1 \mu\text{A}$ . During the experiments the sample was placed into a superconducting magnet with optical windows, made of 50  $\mu\text{m}$  Mylar films. The windows were covered by black paper in order to block visible light and avoid photoconductivity effects; cooling down from the room temperature was also performed in the darkness. The sample volume was filled with liquid helium and pumped to maintain the temperature of the sample at 1.9 K.

## 5.3 DC measurements

When the DC QHE is the subject of a study, the experiments are normally carried out on samples in a form of the Hall bar or the Corbino disk [7]. These shapes are designed to min-

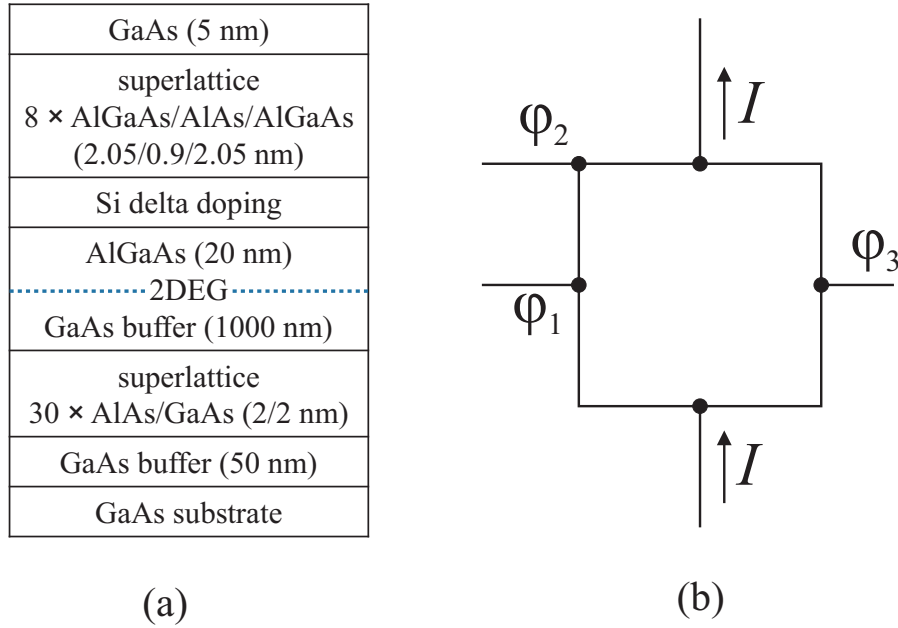


**Figure 5.1:** (a) – Detailed structure of GaAs/AlGaAs heterojunctions. The aluminum fraction in  $Al_xGa_{1-x}As$  is  $x = 31.35\%$ . The samples #1 and #2 differ by the amount of silicon in the doping layer. (b) – scheme of DC measurements. The longitudinal resistance is calculated as  $R_{xx} = (\varphi_1 - \varphi_2)/I$  and the Hall resistance is calculated as  $R_{xy} = (\varphi_1 - \varphi_3)/I$ .

imize the geometric errors in the estimation of components of the resistivity (conductivity) tensor. In our case the main goal of the study is the determination of the high-frequency conductivity, and the accuracy of the DC measurements is less important. In order to compare THz and DC data, obtained in exactly the same conditions, transmission coefficients were measured simultaneously with the resistances  $R_{xx}$  and  $R_{xy}$ . The scheme of electric contacts is shown in Fig. 5.1(b). This configuration allows to measure the voltages  $V_{xx}$  and  $V_{xy}$  simultaneously, with no need to redirect the driving current  $I$ . The resistances serve as a good indicator of the state of the sample, they allow to control the charge density that can change slightly after a heating-cooling cycle. Knowledge of  $R_{xx}$  in zero magnetic field allows to estimate the electron mobility  $\mu^{DC}$ . For this purpose it must be recalculated into the two-dimensional resistivity  $\rho_{xx}$ . We will treat a numerical solution to find the coefficient that relates these two quantities. At the same time we will obtain the distribution of the electric potential in zero field and estimate the error, caused by the finite size of the contacts.

The Maxwell's equations

$$\text{rot } \mathbf{H} = \frac{4\pi}{c} \mathbf{j} + \frac{1}{c} \frac{\partial \mathbf{D}}{\partial t}; \quad \text{div } \mathbf{D} = 4\pi\rho,$$

combined together, result in the continuity equation for the electric current density:

$$\text{div } \mathbf{j} + \frac{\partial \rho}{\partial t} = 0. \quad (5.1)$$

In a linear medium with a constant isotropic conductivity  $\sigma$  the current density and the electric field are parallel. In a static case all time derivatives turn into zero. For the electric potential

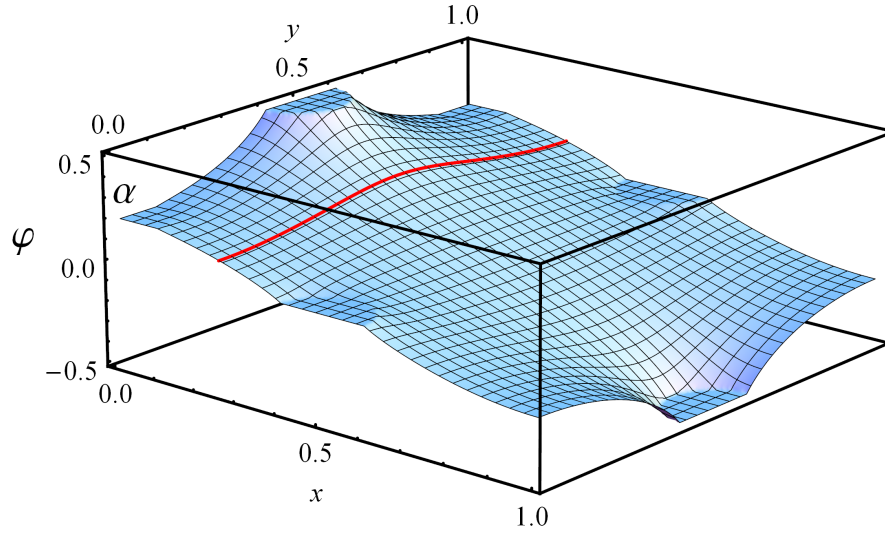


**Figure 5.2:** The calculated distribution of the electric potential  $\varphi$  inside a  $1 \times 1 \text{ cm}^2$  square sample. A potential difference of 1 V is applied to the semicircular contacts of radius 0.1 cm. The value of the potential at the corner is denoted as  $\alpha$ .

$\varphi$ , determined by  $\nabla\varphi = -\mathbf{E}$ , we obtain Laplace's equation:

$$\Delta\varphi = 0. \quad (5.2)$$

Thus the electric potential is a harmonic function inside the area of a sample. We treat a square sample  $[0, 1] \times [0, 1]$  in the  $xy$ -plane. The solution of Laplace's equation (5.2) is determined by the boundary conditions. In the absence of an external magnetic field the off-diagonal conductivity  $\sigma_{xy}$  vanishes and the corresponding boundary condition is given by

$$\frac{\partial\varphi}{\partial\boldsymbol{\nu}} = 0,$$

where  $\boldsymbol{\nu}$  is a vector, normal to the boundary. On a square  $[0, 1] \times [0, 1]$  the problem can be solved analytically for the case of point contacts [75]. We will use the numerical finite difference method to analyze the case of contacts of a finite size. We define a discrete function  $\varphi_{i,j} = \varphi(hi, hj)$ , where  $h$  is the size of the discrete mesh. Laplace's equation (5.2) transforms into the system of linear equations for the discrete case:

$$4\varphi_{i,j} - \varphi_{i,j+1} - \varphi_{i,j-1} - \varphi_{i+1,j} - \varphi_{i-1,j} = 0 \quad (5.3)$$

Electric contacts of an arbitrary shape can be modeled by applying the conditions

$$\varphi_{i,j} = \varphi_{\text{contact}}; \quad \varphi_{i,j} = \varphi_{i',j'}^{\text{neighbor}}$$

at the boundary nodes of the current and voltage contacts, respectively. The results of the calculation on a  $200 \times 200$  mesh are presented in Fig. 5.2. Eight contacts, having the shape of a semicircle (or a quadrant) with the radius 0.1, are placed in the centers of the opposite sides

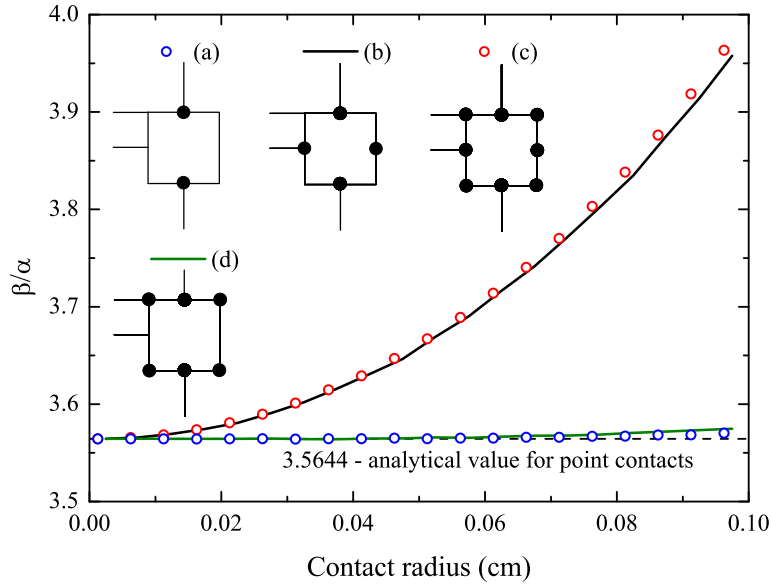


**Figure 5.3:** The calculated correction coefficient in Eq. 5.4 as a function of the contact radius for different configurations (a–d). Black dashed line shows the analytical value for point contacts.

and in the corners of the square. The total current through the sample can be calculated as an integral along any line that is not passing through a contact (red line in Fig. 5.2):

$$I = \int j_x dl = \int_0^1 \sigma_{xx} \frac{\partial \varphi(x_0, y)}{\partial x} dy.$$

Since the numerical mesh has equal steps in  $x$  and  $y$ -directions, the integral can be rewritten as a sum:

$$I = \frac{1}{\rho_{xx}} \sum_{j=1}^n (\varphi_{n_0+1,j} - \varphi_{n_0,j}) = \frac{\beta}{\rho_{xx}}.$$

Here  $n$  is the number of mesh points along one dimension. In the DC experiments the voltage was measured between the points  $(0, 0)$  and  $(1/2, 0)$ . Thus the resistance obtained experimentally is equal to

$$R_{\text{exp}} = \frac{U_{\text{exp}}}{I} = \frac{\alpha}{\beta/\rho_{xx}}, \quad (5.4)$$

where  $\alpha = \varphi(0, 0)$ . Therefore, the two-dimensional resistivity should be calculated as

$$\rho_{xx} = \frac{\beta}{\alpha} R_{\text{exp}} = \frac{\sum_{j=1}^n (\varphi_{i_0+1,j} - \varphi_{i_0,j})}{\varphi_{0,0}} R_{\text{exp}}.$$

The correction coefficient  $\beta/\alpha$  is shown in Fig. 5.3 as a function of the contact radius for different configurations of the contacts. Black solid circles in schemes (a–d) depict contacts with the finite radius. For  $r < 0.01$  the results of the numerical calculation are close to

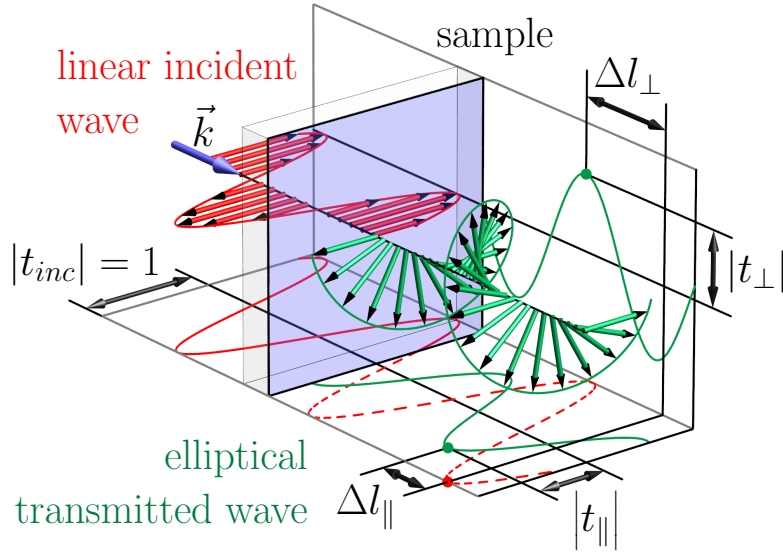


**Figure 5.4:** Transmission spectroscopy of a two-dimensional electron gas. The linearly polarized incident wave becomes elliptically polarized, upon passing through the electron gas in magnetic field. Using a polarizer (not shown), we measure the transmission amplitudes of the linear components along the initial ( $t_{\parallel}$ ) and perpendicular ( $t_{\perp}$ ) directions. A second reference beam, schematically shown by the red dashed line, is used to determine the phase shift  $\Delta l$ , produced by the sample. The knowledge of two complex transmission coefficients  $t_{\parallel} = |t_{\parallel}| e^{ik\Delta l_{\parallel}}$  and  $t_{\perp} = |t_{\perp}| e^{ik\Delta l_{\perp}}$  is sufficient to calculate the high-frequency complex Hall conductivity without additional model assumptions.

the analytical value  $\beta/\alpha = 3.5644$  for point contacts [75]. In the absence of two middle voltage contacts (a, d) the coefficient  $\beta/\alpha$  is practically independent on the contact radius. Therefore configuration (d) is preferable, as it allows a simultaneous measurement of  $V_{xx}$  and  $V_{xy}$ . In experiments presented below the samples have been prepared with eight contacts (c) to increase reliability. The numerical method treated in this section can be used to analyze DC data, obtained on samples with a gate that covers only a part of the surface.

## 5.4 THz experiments

The high-frequency Hall conductivity of the two-dimensional electron gas was measured in the range 69–1100 GHz using the two-beam Mach-Zehnder interferometer (section 2.2.1). Upon passing through the sample, the linearly polarized wave becomes elliptically polarized, see Fig. 5.4. First, a linear component with the same polarization as in the incident wave is filtered by a wire-grid polarizer. The intensity of this component with the sample in the beam, divided by the intensity without the sample, gives the absolute value of a complex parallel transmission  $|t_{\parallel}|^2$ . The phase shift  $\Delta l_{\parallel}$  is measured with the aid of a reference beam to obtain the complex parallel coefficient as  $t_{\parallel} = |t_{\parallel}| e^{ik\Delta l_{\parallel}}$ , where  $k = \omega/c$  is the wave vector. After that, the polarizer is rotated by  $90^\circ$  and the procedure is repeated to obtain a complex crossed transmission coefficient  $t_{\perp} = |t_{\perp}| e^{ik\Delta l_{\perp}}$ . In order to obtain the Hall conductivity as a function of magnetic field, the transmission coefficients are measured at fixed frequencies



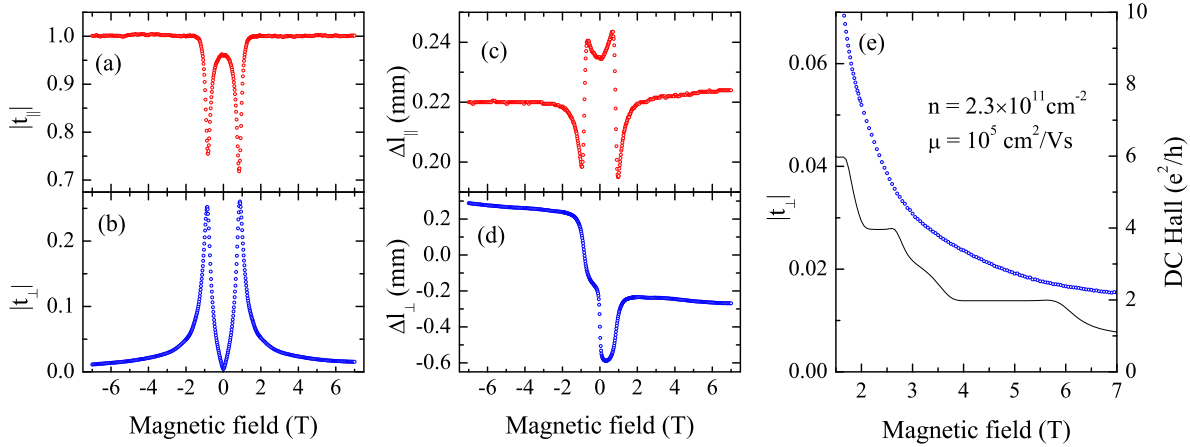


**Figure 5.5:** Field dependence of the transmission coefficients for the sample #1 at 332 GHz. Cyclotron resonance is observed at  $\pm 0.83$  T as a dip in the parallel amplitude (a) and a peak in the crossed amplitude (b). The sign change of the external magnetic field does not affect the parallel transmission ( $t_{\parallel}(B) = t_{\parallel}(-B)$ ), while the complex crossed coefficient changes sign ( $t_{\perp}(B) = -t_{\perp}(-B)$ ). As a result, the parallel phase shift, generated by the sample, is an even function of magnetic field (c), and the values of the crossed phase shift differ by half a wavelength (d). The panel (e) shows  $|t_{\perp}|$  near a wide plateau in DC Hall conductance.

(Fig. 5.5). The frequency, generated by a BWO, is controlled by an accelerating voltage  $V$  and can be set to any value in a certain range. The dependency of a generating power on  $V$  is strongly oscillatory. In order to achieve a better signal-to-noise ratio, we used the frequencies, at which the generating power reaches a local maximum. Another aspect, which affects the choice of the frequency, is the thickness of the substrate. Acting as a Fabry-Pérot resonator, a dielectric slab produces regular oscillations in the transmission spectra (see the upper inset in Fig. 5.6). The frequencies  $f_z$ , at which transmission is maximal, are determined by the relation  $\sqrt{\epsilon}ka = \pi z$ , where  $z$  is an integer. In the framework of the matrix formalism (section 2.1), the substrate is described by a transfer matrix  $M$  that connects electromagnetic (EM) fields at the opposite surfaces. At frequencies  $f_z$  the transfer matrix of a nonabsorbing dielectric slab degenerates into an identity matrix:  $M = (-1)^z I$ . At these frequencies the substrate “disappears”, as it simply replicates the EM field at its surfaces. In the transmission coefficients the substrate causes only a phase shift that is equal to the thickness and a sign change, if  $z$  is odd. For the sample #1 ( $\epsilon = 12$ ,  $a = 0.66$  mm) the frequencies  $f_z$  are multiples of 67 GHz. Measuring at one of the transmission maxima allows to obtain a higher useful signal, other things being equal. For this reason, most of the measurements at fixed frequencies  $f$  were carried out at  $f \approx f_z$ .

## 5.5 Data processing

Knowing the two complex coefficients  $t_{\parallel}$  and  $t_{\perp}$ , one can calculate the complex Hall conductivity at frequency  $\omega$  as (see sections 2.1.2, 4.3.3)

$$\sigma_{xy} = \frac{2\sqrt{\epsilon}e^{-ika}t_{\perp}}{Z_0(t_{\parallel}^2 + t_{\perp}^2)(\sqrt{\epsilon}\cos\beta - i\sin\beta)}, \quad (5.5)$$

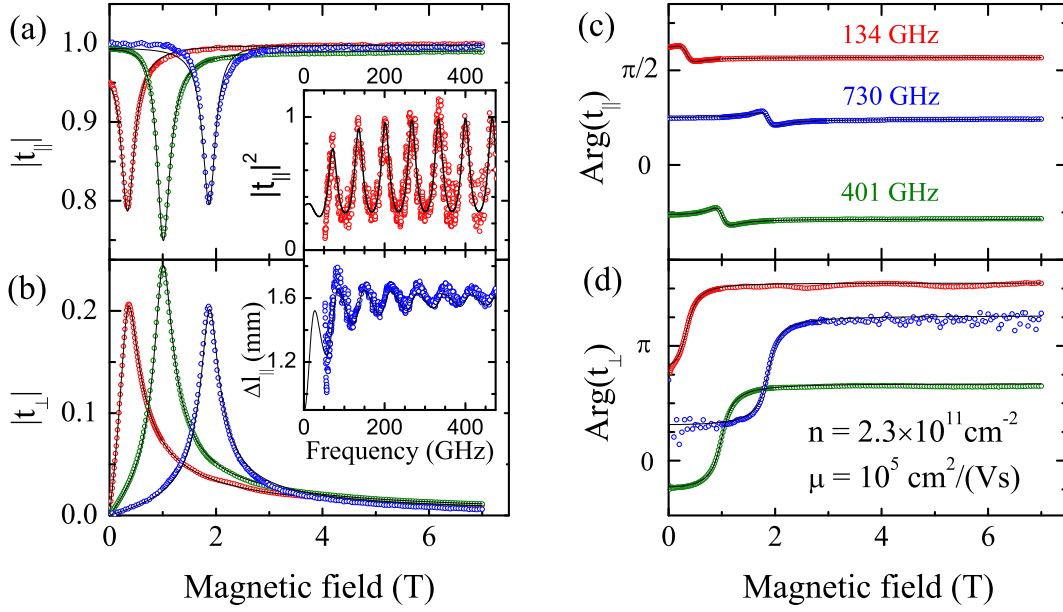


**Figure 5.6:** Symmetrized transmission coefficients for the sample #1 at frequencies 134 (red), 401 (green) and 730 GHz (blue) as a function of external magnetic field. Parallel transmission in zero field is shown as a function of frequency in the insets. Black solid lines represent the classical Drude fits.

where  $a$  is the substrate thickness,  $\varepsilon$  is a dielectric constant of the substrate,  $\beta = \sqrt{\varepsilon}ka$ ,  $Z_0 \approx 377 \Omega$  is the impedance of free space. Before using Eq. (5.5) directly, let us analyze the case, when  $\omega$  is close to one of the transmission maxima and magnetic field  $B$  is much higher than the cyclotron resonance (CR) field  $B_c$ . The vicinity of a maximum corresponds to the value of  $\beta = \pi z$ , where  $z$  is an integer. If the condition  $B \gg B_c$  is satisfied, then the crossed signal is small and the absorption in 2DEG is negligible:  $|t_\perp| \ll |t_\parallel| \simeq 1$ , see Fig. 5.5(a, b). In this case we can simplify Eq. (5.5) to

$$|\sigma_{xy}| = \frac{2}{Z_0} |t_\perp|.$$

Therefore, far from the cyclotron resonance the plot of directly measured quantity  $|t_\perp(B)|$  represents the absolute value of the Hall conductivity  $|\sigma_{xy}|$ , measured in units of  $2/Z_0$ . Figure 5.5(e) shows the curve  $|t_\perp(B)|$ , measured at 332 GHz, together with the DC Hall conductance. The  $y$ -scales in Fig. 5.5(e) are intentionally mismatched, in order to avoid overlapping data and to clearly demonstrate the absence of any sign of a quantum plateau in the high-frequency Hall conductivity. As mentioned above, the DC and THz curves were obtained simultaneously in the same experiment, to exclude heating of 2DEG by the THz wave as a possible explanation of the disappearance of quantization [69].

Figure 5.6 shows an example of (anti)symmetrized transmission data together with the classical Drude fitting curves (see section 4.3.3). The fitting procedure allows to estimate the effective cyclotron mass  $m$ , the relaxation time  $\tau$ , and the electron density  $n_{2D}^{\text{THz}}$  in 2DEG. We define the quantity  $\mu^{\text{THz}} = e\tau/m$  that can be compared with the mobility  $\mu^{\text{DC}}$ , obtained from the DC measurements of  $R_{xx}$ . The electron density is another parameter that is obtained in

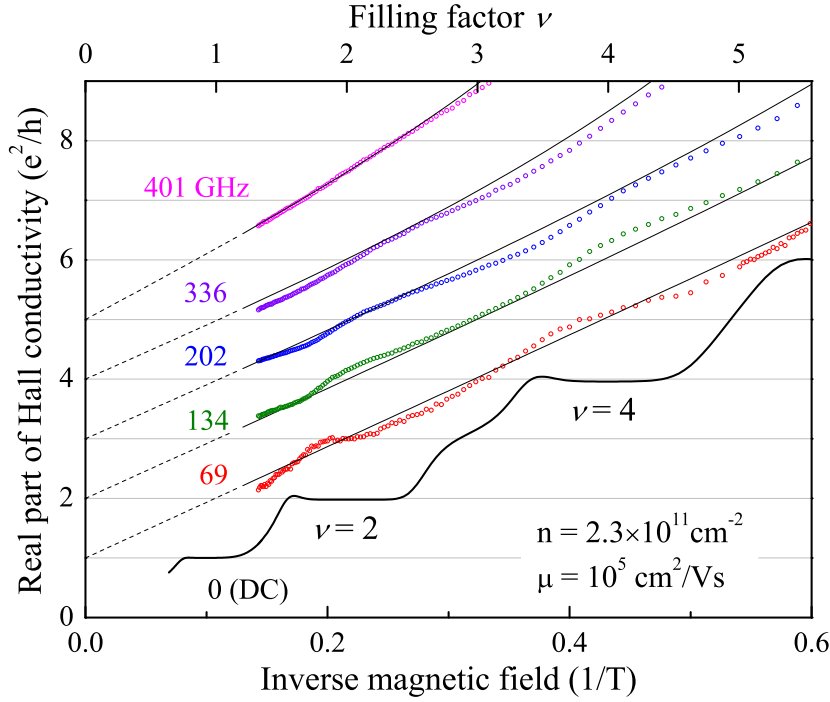


**Figure 5.7:** Evolution of the Hall conductivity with increasing frequency for the sample #1. DC conductivity, shown by the black solid line, exhibits plateaus near the even filling factors  $\nu$ . High-frequency curves are shifted by  $e^2/h$  for clarity. At 69 GHz (red) the real part of  $\sigma_{xy}$  has a narrow plateau only around  $\nu = 2$ . Further increasing of the frequency leads to the smearing of the plateau and to the suppression of quantum deviations from classical Drude behavior, shown by thin black curves.

DC and THz experiments independently. Both the density and the mobility are found to be in a good agreement, as it can be seen in Tab 5.1.

## 5.6 Real part of the high-frequency Hall conductivity

In order to trace the evolution of quantum plateaus with increasing frequency, we plot the real part of the Hall conductivity in the sample #1 as a function of inverse magnetic field in Fig. 5.7. The DC conductance, shown by the black curve, demonstrates wide plateaus at even filling factors  $\nu$ . In a separate experiment, the DC measurement was extended up to 14 T. It was found, that the plateau at  $\nu = 1$  is also resolved. The overall behavior of the high-frequency data is well described by the classical Drude theory [17], shown by thin black curves. At frequencies below 250 GHz the cyclotron resonance is located in low magnetic fields, thus the fitting curves in Fig. 5.7 are close to a straight line  $\text{Re } \sigma_{xy} \propto B^{-1} \propto \nu$ . At 69 GHz (red symbols) a plateau at  $\nu = 2$  can be detected in the experimental conductivity. The width of this plateau is about 30% of that in the DC data. There is no interval with constant  $\text{Re } \sigma_{xy}(B)$  at 134 GHz (green symbols), even the slope  $\partial \sigma_{xy} / \partial \nu$  does not tend to zero at  $\nu = 2$ . At 134 GHz the filling of the second Landau level reveals as a slight quantum deviation from the classical curve  $\text{Re } \sigma_{\text{Drude}}(B)$ . At higher frequencies the amplitude of the

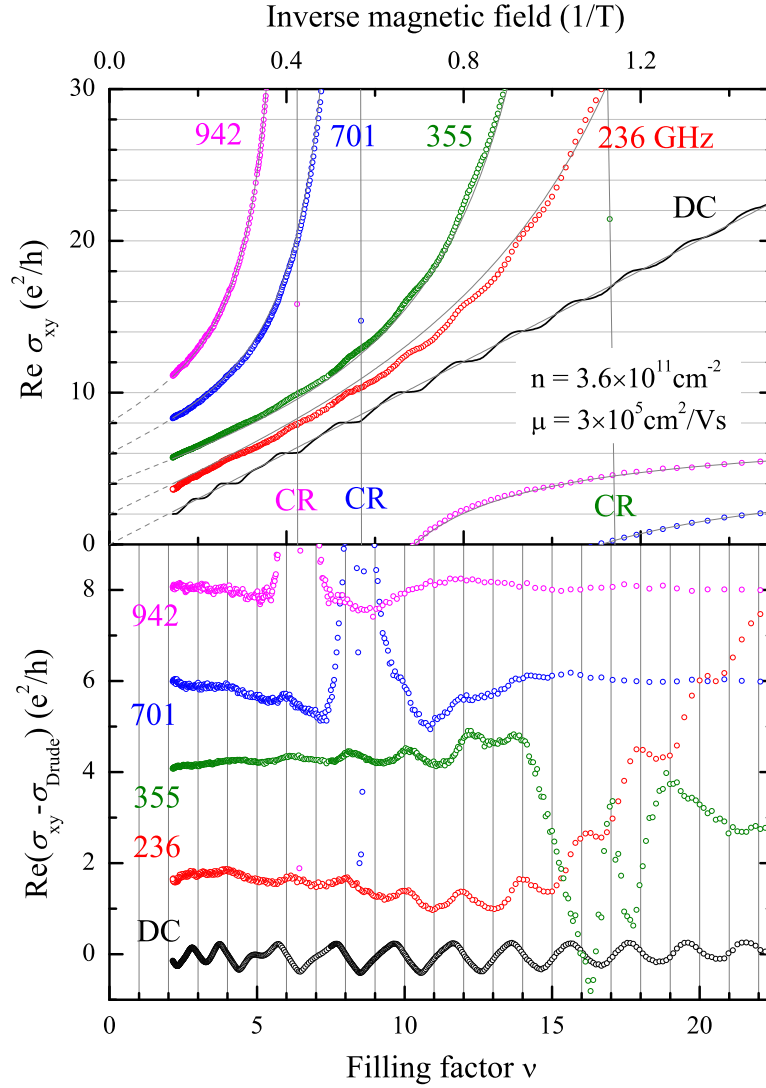


**Figure 5.8:** The upper panel shows the Hall conductivity for the sample #2 at different frequencies as a function of inverse magnetic field. Positions of the cyclotron resonance are denoted by “CR”. Solid gray lines are classical Drude fits. The difference between the experimental data and the classical fits is shown in the lower panel. For clarity, the data sets are shifted by  $2e^2/h$  in both panels.

quantum deviation decreases. At 401 GHz (magenta symbols) no signs of the initial plateau can be detected visually on the plot. The position of the quantum feature in  $\text{Re } \sigma_{xy}(B)$  can be determined by tracking the minimum of the slope that shifts to lower magnetic fields with increasing frequency. Plateaus at higher filling factors are smeared out already at 69 GHz and disappear in a similar way.

In comparison with the sample #1, the sample #2 has a higher electron mobility and an electron density (see Tab. 5.1). Evolution of the real part of  $\sigma_{xy}$  for the sample #2 is shown in Fig. 5.8. Similarly to the sample #1, the cyclotron resonance in high-frequency Hall conductivity can be approximated by classical Drude fits (upper panel in Fig. 5.8). Quantum oscillations, corresponding to the filling of Landau levels, can be detected in the high-field re-

gion as well. While the oscillations attenuate with increasing filling factor  $\nu$  in the sample #1, a maximal amplitude of the quantum deviations in the sample #2 is achieved at filling factors  $\nu > 10$ . It can be best seen in the lower panel of Fig. 5.8, where the difference between the experimental conductivity and the classical Drude fit is plotted. The large discrepancy close to the resonance field  $B \approx B_c$  is due to the large value of the optical conductivity (approaching  $100 e^2/h$ ) along with the steep slope  $\partial\sigma_{xy}/\partial\nu$ . Although no flat plateaus can be detected in the high-frequency  $\sigma_{xy}$ , the quantum deviations at 236 GHz near  $\nu = 14$  are comparable with the quantum deviations in the DC conductance. According to the relation  $\Omega_c \propto B \propto 1/\nu_c$ , the cyclotron resonance shifts to lower  $\nu$  as the radiation frequency increases. The lower panel in Fig. 5.8 demonstrates that the quantum oscillations become attenuated to the right of the CR ( $\nu > \nu_c$ ), where the radiation frequency exceeds the cyclotron gap ( $\omega > \Omega_c$ ).

## 5.7 Imaginary part of the high-frequency Hall conductivity

While the Hall conductivity is a real number in the static case, it becomes a complex number with a nonzero imaginary part at finite frequencies. Figure 5.9 shows the experimentally obtained  $\sigma_{xy}(\nu)$  (symbols) at 134 and 202 GHz together with Drude fits (solid curves) for the sample #1. Figures 5.9(a, c) show  $\sigma_{xy}$  on a complex plane as a parametric plot with the filling factor  $\nu$  as a parameter. The sweep of magnetic field from 7 to 0 T corresponds to the change of  $\nu$  from 1.32 to  $\infty$ . In this representation the classical theory produces a circle-like curve, depicted in the insets by black solid lines. The higher the frequency, the closer the shape to a perfect circle, centered on the imaginary axis and passing through the origin of coordinates. The resonance behavior of experimental conductivity is well described by the classical Drude theory. However, when only a few Landau levels are occupied,  $\sigma_{xy}$  demonstrates substantial deviations from the classical curve, see Fig. 5.9(a, c). Due to experimental limitations, the complex argument of  $\sigma_{xy}(\nu)$  is determined up to an unknown constant value, which can be estimated by comparison with the Drude fit. In figure 5.9 this value is chosen to match the theoretical and experimental curves near  $\nu = 10$ , where the quantum deviations are faded out. In this case the imaginary part of the quantum correction appears to be positive nearly everywhere and the imaginary part of  $\sigma_{xy}$  tends to preserve its original sign. As discussed above, in the real part of  $\sigma_{xy}$  the deviations can be regarded as remnants of the DC Hall plateaus. Figures 5.9(b, d) show the real part of the difference  $\sigma_{xy} - \sigma_{\text{Drude}}$ , depicted by green symbols on the same scale as the imaginary part. These plots demonstrate, that the quantum oscillations have similar amplitudes in the real and imaginary parts and that their phases are shifted by  $\approx \pi/2$ . The broken periodicity below  $\nu = 2$  is probably due to the presence of the quantum plateau at  $\nu = 1$ , which is the only odd plateau that is resolved in this sample (Fig. 5.7).

## 5.8 Review of theoretical models

The most striking feature of the QHE at zero frequency is the exact quantization of the Hall resistance  $R_{xy}$ , which is a macroscopic property of a whole sample, directly obtained in DC

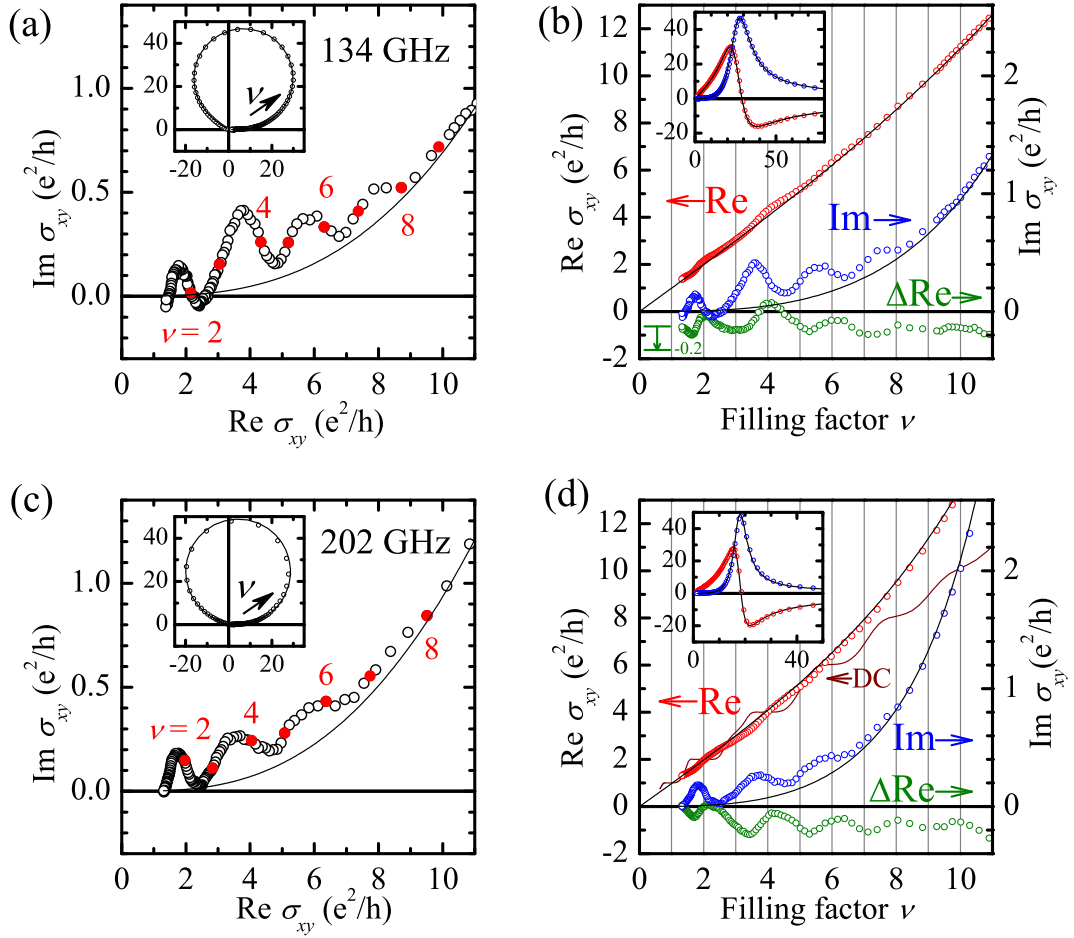


**Figure 5.9:** The complex Hall conductivity  $\sigma_{xy}$  in the sample #1 at 134 GHz (a, b) and at 202 GHz (c, d). The main panels show the high field part and the insets show the full range 0–7 T of the applied magnetic field. The panels (a, c) show  $\sigma_{xy}$  on a complex plane as a parametric plot with the filling factor  $\nu$  as a parameter. The integer values of  $\nu$  are indicated by red symbols. The overall resonance behavior, shown in the insets, is well described by the Drude model (black solid lines). In the low- $\nu$  limit, where QHE is observed in DC, the imaginary part of  $\sigma_{xy}$  demonstrates substantial periodic deviations from the classical curve (b, d). This deviations are comparable to the deviations in the real part, shown by green symbols on the same scale.

experiments. This fact alone does not prove that  $\sigma_{xy}$  is also exactly quantized [76], because local inhomogeneities of the two-dimensional gas are always present in a real sample. Unlike the contact techniques, the spectroscopic experiments test  $\sigma_{xy}$  directly. Experiments at 30 GHz [76] demonstrated that plateaus of non-zero width are also present in  $\sigma_{xy}$ . As shown above, the plateaus in  $\sigma_{xy}$  disappear at higher frequencies. For our samples the critical frequency lies near 100 GHz. Above this frequency the two-dimensional electron gas loses its QHE features and the Hall conductivity follows the classical Drude behavior.

Although the IQHE has been extensively studied theoretically, only a few works addressed the Hall conductivity in the high-frequency regime [10]. When calculating Hall conductivity in a linear approximation, a common approach is to apply a linear perturbation theory (Kubo formalism) to a model system.

The theoretical models of the IQHE consider non-interacting fermions in a strong magnetic field, placed in some model potential, which simulates presence of impurities and constraints of a sample. Depending on the chosen potential, the analysis of such models can be done analytically or numerically.

In Refs. [10, 11] the high-frequency Hall conductivity was calculated using numerical method of exact diagonalization. In order to model the disorder, the authors treated randomly distributed Gaussian scatterers with the potential

$$V(\mathbf{r}) = \pm \frac{u}{2\pi d^2} \exp\left(-\frac{|\mathbf{r} - \mathbf{R}|^2}{2d^2}\right),$$

where the parameter  $d$  is comparable to the magnetic length  $\sqrt{\hbar/eB}$ . As calculated within this model,  $\sigma_{xy}(\omega)$  was found to retain the Hall plateaus in the THz range. In Ref. [72] these model results were referred to justify the procedure of averaging  $\sigma_{xy}(\omega, \nu)$  over a range of frequencies from 0.5 to 1.2 THz. The resulting averaged  $\tilde{\sigma}_{xy}(\nu)$  has a plateau-like feature of vanishing width in comparison with a wide plateau in DC. This experimental fact, reported in Ref. [72], indicates that the plateaus actually smear out below 1.2 THz. Therefore, the procedure of averaging appears to be inappropriate, since it only masks the disappearance of the Hall plateaus.

In earlier works the high-frequency Hall conductivity was treated analytically in two opposite limits: for scatterers with  $\delta$ -potential [13] and for a slowly varying potential of impurities [12]. In Ref. [13] the Hall conductivity was obtained within the  $\delta$ -impurity model [77] as a function of electron density  $n$ . At finite frequencies the dependence  $\text{Re } \sigma_{xy}(n)$  is predicted to have a single-dip or a double-dip structure instead of a flat plateau at DC. A monotonic dependence  $\text{Re } \sigma_{xy}(n)$  is achieved only if both negative and positive  $\delta$ -impurities are present in the calculation and the Landau level broadening exceeds the cyclotron energy. The last condition is probably not fulfilled in our samples, while the experimental high-frequency  $\text{Re } \sigma_{xy}(B)$  is monotonic in the vicinity of the DC plateaus. Unfortunately, the imaginary part of  $\sigma_{xy}$  was not treated in Ref. [13] and no explicit estimation was given for the critical frequency, at which the plateaus are destroyed. However the consideration can be extended to cover these questions. In particular, the critical frequency  $f_0$  turns out to be close to the half-width  $\Gamma/(4\pi\hbar)$  of the corresponding broadened Landau level [78]. If we assume that the level broadening is caused by the scattering on short-range ionized impurities, then the width can be estimated as [79]:

$$\Gamma = \hbar \sqrt{\frac{2\Omega_c}{\pi\tau}}. \quad (5.6)$$

Since the cyclotron frequency  $\Omega_c = eB/m$  increases with magnetic field, the plateaus at small filling factors are expected to retain at higher radiation frequencies. Using the parameters in Tab. 5.1 for the sample #1, we obtain the critical frequency as  $f_0 = 47\sqrt{B}$  GHz. For the plateaus at  $\nu = 2$  and  $\nu = 4$  the estimated critical frequencies are 102 and 72 GHz respectively. In agreement with this estimation, we have experimentally observed the plateau  $\nu = 2$  at 69 GHz. The plateau at  $\nu = 4$  is not resolved, as the corresponding critical frequency of 72 GHz is close to the radiation frequency. The plateaus at  $\nu > 4$  are already absent at  $f \geq 69$  GHz, since they occur at even lower magnetic fields in  $R_{xy}$ . Due to the longer relaxation time in sample #2 (Tab. 5.1) the estimated Landau level width is smaller and the critical

frequency is lower, than in sample #1. For this reason no plateaus in the high-frequency conductivity could be observed in sample #2. If we try to apply Eq. (5.6) to the case of CdHgTe films [80] and to the graphene [59], we obtain the critical frequencies 1 THz and  $\approx 3$  THz respectively. These higher values are formally achieved due to the smaller effective masses and the shorter relaxation times in the CdHgTe wells and in the graphene. The direct application of Eq. (5.6) to the systems with the strongly non-parabolic dispersion is questionable. However it is possible that the observation of the quantized Faraday rotation in these materials at higher frequencies is indeed connected to the larger width of Landau levels.

In Ref. [12] the Hall conductivity was calculated using the drift approximation [81, 82]. In the limit of very high frequencies  $\sigma_{xy}(\nu)$  was found to tend to the classical straight line with a small quantum correction:

$$\sigma_{xy}(\nu) = \nu e^2/h + \delta\sigma_{xy}(\nu).$$

As calculated within this model, the term  $\delta\sigma_{xy}$  has zero imaginary part, while our experimental  $\delta\sigma_{xy}$  has both real and imaginary parts of a similar amplitude. The calculation for intermediate frequencies results in  $\sigma_{xy}$  with a non-zero imaginary part. However in this case the dependency  $\text{Re } \sigma_{xy}(\nu)$  is not monotonic. Thus the shape of smeared quantum plateaus is not described by this approach even qualitatively. The critical frequency calculated in the drift approximation is connected to the level broadening, similarly to the case of  $\delta$ -potential treated above.

To conclude, none of the three theoretical models provides a satisfactory description for the shape of plateaus in the high-frequency Hall conductivity. The numerical method of exact diagonalization predicts persistence of the plateaus in the THz range. Within this model, a decrease in the disorder leads to a decreasing width  $\Gamma$  of Landau levels and to a more distinct quantization in  $\sigma_{xy}$ . In opposite to this, the analytical methods predict a destruction of the plateaus at frequencies  $f > \Gamma/h$ . Within these models a stronger disorder allows to observe the quantum plateaus at higher frequencies. The experimental data presented here and in Refs. [59, 73, 76, 80] seem to support the result of the analytical methods. An ultimate understanding requires further systematic experimental studies on samples with significantly different electron mobilities and cyclotron masses.

## 5.9 Summary

The dynamic IQHE was studied using the CW THz spectroscopy in the range 69–1100 GHz. A clear frequency dependence of the quantum deviations from the classical Drude model was observed. The disappearance of the QHE plateaus takes place around 100 GHz. Only small quantum corrections are observed above this frequency. Some theoretical models describe this phenomenon qualitatively, whereas some other models even predict persistence of the plateaus in the high-frequency range. The results of this work present an important cornerstone on the way towards complete understanding of the IQHE.



## 6 Dzyaloshinskii-Moriya electromagnon in dysprosium manganite

Thus far we have dealt with two-dimensional electron systems in an external magnetic field. In this chapter we are going to treat a bulk insulator  $\text{DyMnO}_3$ . Although it might be treated as an example of a completely different system from a separate area of research (physics of magnets and multiferroics), one can find direct analogies between these systems. In both cases the considered phenomena take place at low temperatures, where the stochastic motion in matter is suppressed and even weak microscopic interactions can determine macroscopic properties of a sample. Just as in  $\text{HgTe/CdHgTe}$  quantum wells, the spin-orbit coupling plays an important role in  $\text{DyMnO}_3$ : because of this interaction  $\text{DyMnO}_3$  acquires ferroelectric properties. Like in the experiments on the dynamic Hall effect, the most interesting results have been obtained by measuring rotation of the polarization plane. In this chapter we will have an opportunity to use the rather cumbersome  $4 \times 4$  matrix formalism in all its strength: in the case of a tilted cut of an anisotropic crystal with non-zero magnetoelectric susceptibility tensors, the formalism provides a rather elegant and concise solution.

### 6.1 Introduction to electromagnons

Electric and magnetic field control of the propagation and the polarization state of terahertz radiation is one of the prerequisites for continuous progress of modern electronics. A number of recent developments in this direction have been achieved using multiferroics, i.e. materials simultaneously revealing electric and magnetic ordering [83–87]. Several multiferroics provide not only a direct coupling between static electric and magnetic properties but also give a possibility to modify dynamic susceptibilities by external fields. Application of a static magnetic field to the multiferroic materials leads to dichroism in the terahertz range [88, 89] or even to more complex effects like controlled chirality [90] or directional dichroism [91–93]. Electric control of terahertz radiation is more difficult to realize and it has been recently demonstrated in Raman scattering experiments [94].

Dynamical properties of several multiferroic materials in the terahertz range are governed by novel magnetoelectric modes called electromagnons [95–98]. Electromagnons may be defined as collective excitations of the magnetic structure which are coupled to the electric dipole moment. They may be regarded as a mixture of magnons and phonons. In orthorhombic rare earth manganites  $\text{RMnO}_3$  one generally observes several electromagnons in the terahertz and subterahertz range. A strong high frequency mode around 2–3 THz is well understood on the basis of a symmetric Heisenberg exchange (HE) coupling [99, 100] as a zone edge magnon which can be excited by electric component of the electromagnetic radiation. A second intens-

ive mode existing at 0.5–1 THz has been explained using the same mechanism but including a Brillouin zone folding due to modulation of the magnetic cycloid [100, 101]. In the sub-terahertz frequency range a series of weaker modes is observed in optical [96, 102] and neutron scattering experiments [103]. These modes are explained as the magnetic eigenmodes of the spin cycloid in RMnO<sub>3</sub>. Some of these modes may get an electrical dipole activity due to the relativistic Dzyaloshinskii-Moriya (DM) mechanism. Dynamic contributions due to this mechanism have been investigated both experimentally and theoretically [102, 104–107]. In spite of its weakness, the DM interaction is a promising mechanism especially in application to spiral magnets as it connects static spontaneous polarization and magnetic structure [104, 108]. This mechanism is responsible for the switching of ferroelectric polarization by magnetic field and for the control of magnetic structure by electric voltage in spiral magnets [87]. It may be expected that in the frequency range where the dynamics is governed by the DM mechanism, the terahertz light will be controlled by electric field as well. In present experiments this idea is utilized for two purposes: to obtain a direct evidence of dynamical magnetoelectric coupling within the DM electromagnon and to demonstrate a possibility to control the polarization of terahertz light by applying static electric fields.

## 6.2 Dzyaloshinskii-Moriya electromagnon in dysprosium manganite

DyMnO<sub>3</sub> is a multiferroic manganite with orthorhombic structure. The high-temperature paramagnetic state in this material transfers into an incommensurate antiferromagnetic structure below  $T_N \approx 39$  K. At lower temperatures a second phase transition into a ferroelectric phase takes place at  $T_c \approx 19$  K. By analogy to TbMnO<sub>3</sub> this phase is most probably a cycloidal antiferromagnet [109] with an incommensurate propagation vector. Below the transition to the cycloidal state DyMnO<sub>3</sub> reveals a static electric polarization which is aligned along the *c*-axis (*Pbnm* crystallographic setting is used throughout this chapter). This polarization is well described by the DM coupling which leads to a simple expression [108]:

$$\mathbf{P}_0 \propto \delta_{j \rightarrow j+1} \times (\mathbf{S}_j \times \mathbf{S}_{j+1}). \quad (6.1)$$

Here  $\mathbf{S}_j$  and  $\mathbf{S}_{j+1}$  are the neighbor Mn<sup>3+</sup> spins within *ab*-planes and  $\delta_{j \rightarrow j+1}$  is the vector connecting them, see Fig. 6.1(a). The spin cycloid breaks the space inversion symmetry and has two possible rotation directions of the spins ( $\odot$  and  $\ominus$ ). According to Eq. (6.1), the sign of the static polarization is opposite in these two cases, see Fig. 6.1(a). Therefore, the antiferromagnetic domains are simultaneously ferroelectric domains, and the orientation of the spin cycloid is also affected by an external electric field.

The idea of the present experiment is based on the DM coupling between static and dynamic properties in DyMnO<sub>3</sub>. A schematic picture of the cycloidal magnetic structure in DyMnO<sub>3</sub> is shown in Fig. 6.1(a). Because of an incommensurate character of the cycloid, the solution of the dynamic equations for this structure reveals three eigenmodes. For the present experiment only one mode is the most promising. Within this mode magnetization and electric polarization oscillate along the *b* and *a* axes, respectively (DM electromagnon in Fig. 6.1(a)).

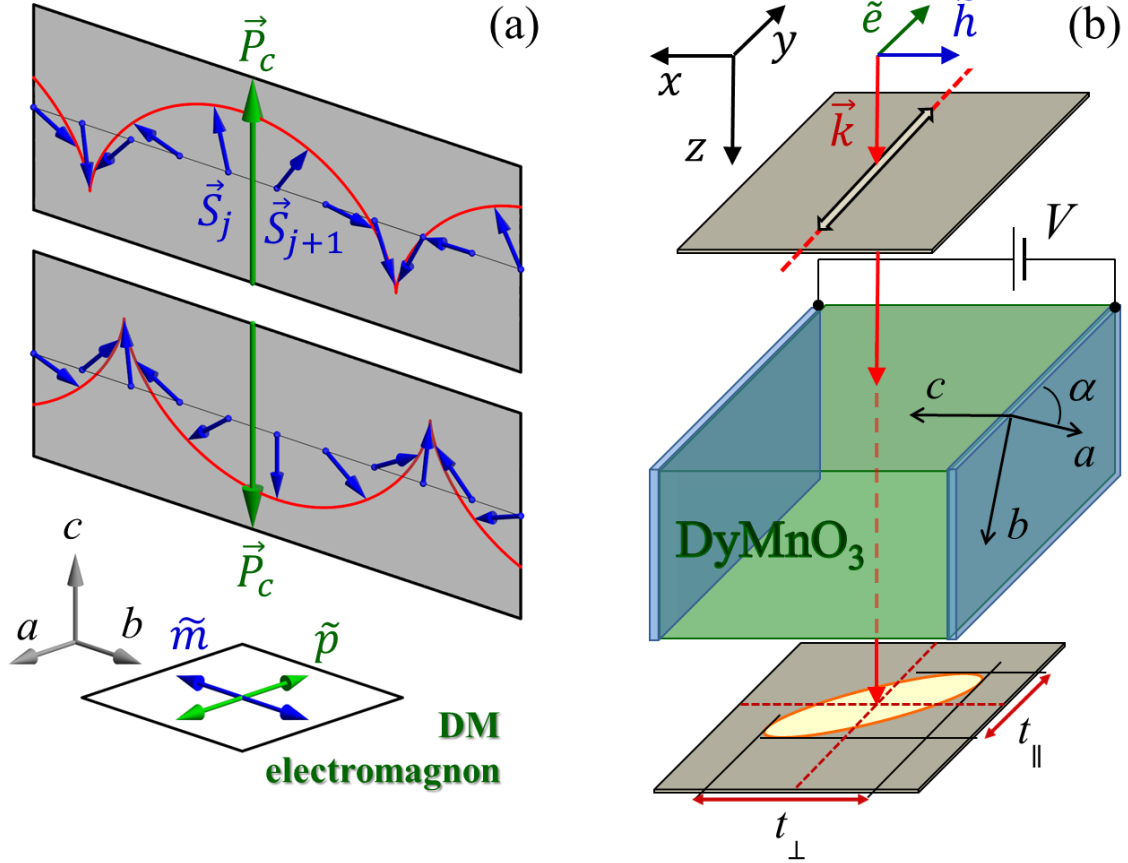


**Figure 6.1:** Experiment to observe electrically controlled dynamic magnetoelectric effect. (a) – schematic representation of the magnetic  $bc$ -cycloid and the static electric polarization (green arrows) in  $\text{DyMnO}_3$ . Shown are two possible domains with opposite orientations of the cycloid and the polarization. Bottom diagram indicates oscillations of electric and magnetic moments for magneto-electrically active mode (DM electromagnon). (b) – geometry of the  $\text{DyMnO}_3$  crystal and of the experimental apparatus to separate waves of different polarizations.

Therefore, this mode can be excited either via electric channel by  $e\|a$  and via magnetic channel by  $h\|b$ . Moreover, these two channels are not independent. The electric excitation drives also the magnetic moment and vice versa. This cross coupling is manifested in the existence of the nonzero dynamic magnetoelectric susceptibility  $\chi_{ab}^{me}$ . In the crystallographic coordinate system  $abc$  the susceptibility matrix for  $\text{DyMnO}_3$  has a simple form:

$$\begin{pmatrix} D_a \\ D_b \\ D_c \\ B_a \\ B_b \\ B_c \end{pmatrix} = \begin{pmatrix} \varepsilon_a & 0 & 0 & 0 & i\chi_{ab} & 0 \\ 0 & \varepsilon_b & 0 & 0 & 0 & 0 \\ 0 & 0 & \varepsilon_c & 0 & 0 & 0 \\ 0 & 0 & 0 & \mu_a & 0 & 0 \\ -i\chi_{ab} & 0 & 0 & 0 & \mu_b & 0 \\ 0 & 0 & 0 & 0 & 0 & \mu_c \end{pmatrix} \begin{pmatrix} E_a \\ E_b \\ E_c \\ H_a \\ H_b \\ H_c \end{pmatrix}. \quad (6.2)$$

The main experimental difficulty to observe the dynamic magnetoelectric effect in  $\text{DyMnO}_3$  is that it cannot be detected in an experiment with an  $ab$ -plane cut crystal. In such geometry the ac fields of the incident wave are either  $e\|b$  and  $h\|a$  and do not excite the electromagnon at all, or they are  $e\|a$  and  $h\|b$  and, therefore, they both excite the electromagnon at the same time. The existence of the magnetoelectric effect in such geometry does not lead to an emergence of a wave with the perpendicular polarization but only slightly changes the absorption of light. In order to overcome this difficulty, the sample with tilted axes has to be used. The geometry of such an experiment is shown in Fig. 6.1(b). In the following arguments we assume incident wave with electric field component  $e\|ab$ -plane of the crystal which excite the DM electromagnon via electric channel. This geometry is equivalent to  $e\perp c$  in Fig. 6.1(b) and contains both components of the electric field  $e\|a$  and  $e\|b$ . Because the DM electromagnon has nonzero magnetoelectric component  $\chi_{ab}^{me}$ , an ac magnetic field  $h\|b$  will be induced by this excitation. This electromagnetic field corresponds to a wave with polarization perpendicular to the incident wave with  $h\|c$ . Thus, an appearance of a signal in crossed polarizers is a characteristic of a nonzero magnetoelectric susceptibility. These qualitative arguments are supported by rigorous calculations within the  $4 \times 4$  matrix formalism. Let us denote as  $M_{6 \times 6}^{abc}$  the square matrix in Eq. 6.2 that is combined of  $3 \times 3$  submatrixes, representing the susceptibility tensors in the crystallographic system. Then in the laboratory coordinate system  $xyz$  the tensors are represented by the matrix  $M_{6 \times 6}^{xyz} = V_{6 \times 6}^{-1} M_{6 \times 6}^{abc} V_{6 \times 6}$ , where

$$V_{6 \times 6} = \begin{pmatrix} V_{3 \times 3} & 0 \\ 0 & V_{3 \times 3} \end{pmatrix}; \quad V_{3 \times 3} = \begin{pmatrix} 0 & \cos \alpha & \sin \alpha \\ 0 & -\sin \alpha & \cos \alpha \\ 1 & 0 & 0 \end{pmatrix}. \quad (6.3)$$

The matrix  $V_{3 \times 3}$  with  $\alpha \approx \pi/4$  describes the rotation of the crystallographic axes with respect to the laboratory coordinate system. Thus  $M_{6 \times 6}^{xyz}$  is the permittivity matrix in Eq. 2.1, which coefficients are used to calculate the  $4 \times 4$  matrix in Eq. 2.4. The values of dielectric permittivities  $\varepsilon_{a,b,c}$  and magnetic permeabilities  $\mu_{a,b,c}$  have been obtained in transmission experiments with normally cut samples [110]. The matrix equations (2.4–2.5) have been solved numerically to obtain the coefficient  $\chi_{ab}^{me}$ . In agreement with the qualitative arguments, a non-zero crossed component emerges only for  $\chi_{ab}^{me} \neq 0$  and in a linear approximation  $t_{\perp} \propto \chi_{ab}^{me}$ .

We note that within the present experiment the existence of DM electromagnon which can be excited at the center of the Brillouin zone is crucial. As shown in the rigorous solution [110, 111], the electrically and magnetoelectrically active mode can be represented as a symmetric superposition of two magnons with wavevectors  $\mathbf{q} = +\mathbf{Q}$  and  $\mathbf{q} = -\mathbf{Q}$ . Here  $\mathbf{Q}$  is the modulation vector of the magnetic cycloid [99]. The symmetric mode represents an electromagnon which have nonzero dynamic polarization along the  $x$  axis and, therefore, can be excited by electromagnetic wave with  $e \parallel a$ .

In case of (although much stronger) Heisenberg electromagnons [99, 100] which are excited as a zone edge magnons, the present experiment would not work. For the zone edge electromagnon the neighbor spins oscillate out-of-phase, which cancels the resulting magnetic moment. Although this mode reveals a strong electric contribution, the magnetic and magnetoelectric susceptibilities are zero. As will be shown in more detail below (Fig. 6.4), the dynamic magnetoelectric effects observed in  $\text{DyMnO}_3$  are indeed centered around the weak DM electromagnon at 210 GHz and they are absent around the strong Heisenberg electromagnon around 550 GHz.

The remaining point is the requirement of an electrical poling of  $\text{DyMnO}_3$  crystal. Without poling, two types of domains coexist in the sample, see Fig. 6.1(a). The domains with the opposite ( $\odot$  or  $\ominus$ ) rotation of the spin cycloid reveal the opposite sign of the magnetoelectric susceptibility, canceling the effect. In order to avoid the signal compensation from different domains, during a cooling a static electric field  $\mathbf{E}$  was applied to the sample along the  $c$ -axis. Such poling orients the majority of the domains along one direction.

### 6.3 Complex correction of crossed transmission

The crossed transmitted component, caused by the sample, has the maximal amplitude near 210 GHz. Even in this case its absolute value is comparable to the parasitic depolarizing effects of the optical windows, imperfections of polarizers, etc. In order to remove the side contributions, we have used the method of complex subtraction that was treated in section 4.3.3, Eq. 4.5. Figure 6.2 shows the raw crossed coefficient  $t_{\perp}$  on a complex plane as a parametric plot with temperature as a hidden parameter. The data is taken at 210 GHz on cooling down from 40 K to 3 K. Red and blue solid circles correspond to cooling in a static electric field along  $c$ -axis. Gray open and solid circles represent the data in the absence of the polarizing field. Above  $T_c = 19$  K the crossed amplitude  $t_{\perp}$  is not affected by applied voltage and all the curves coincide. Below  $T_c$  the sample is in a ferroelectric state with two possible orientations of domains. The domains of the opposite sign are expected to rotate the polarization plane in the opposite directions. In agreement with this picture, the curves, corresponding to the sample polarized by  $\pm 250$  V, separate below  $T_c$ . The curves, obtained in the absence of poling voltage, also demonstrate some discrepancy in the ferroelectric state, which is about 20% of the difference ( $t_{\perp}(+250) - t_{\perp}(-250)$ ). This fact can be interpreted as an indication of memory effects: if a single-domain sample is heated above  $T_c$ , then after cooling in zero field the domains of the same sign will slightly prevail in the ferroelectric state. We assume that a fully compensated sample with equal amounts of the opposite domains

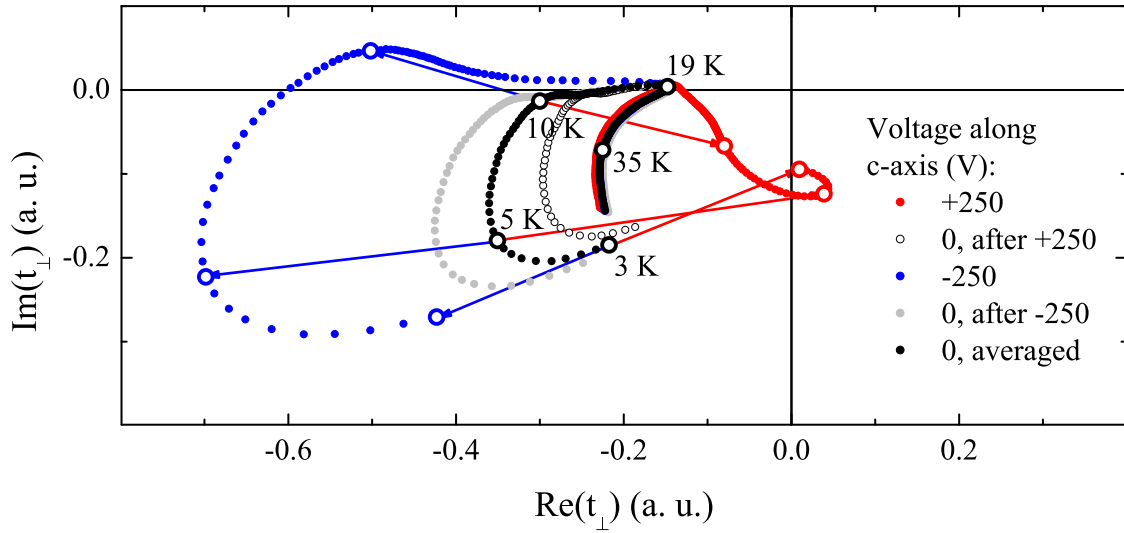


**Figure 6.2:** Raw crossed coefficient  $t_{\perp}$  on a complex plane as a parametric plot with temperature as a hidden parameter. The data is taken at 210 GHz with the incident linear polarization  $e \parallel c$ . Above  $T_c = 19$  K the coefficient  $t_{\perp}$  is not affected by applied voltage and all the curves coincide. Below  $T_c$  the curves separate. The complex difference  $t_{\perp}(V) - t_{\perp}(0)$  is shown by arrows for temperatures 10, 5 and 3 K. Note the opposite direction and the equal length of the arrows to positive and negative voltage.

would result in a crossed coefficient equal to

$$t_{\perp}^0 = \frac{t_{\perp}(+0) + t_{\perp}(-0)}{2}, \quad (6.4)$$

where  $\pm 0$  denotes cooling in zero field after positive and negative voltage, respectively. The value  $t_{\perp}^0$ , shown by black symbols in Fig. 6.2, was used as a reference to correct the experimental crossed coefficient as

$$t_{\perp}^{\text{corr}}(T) = t_{\perp}(T) - t_{\perp}^0(T). \quad (6.5)$$

Examples of  $t_{\perp}^{\text{corr}}(T)$  are shown in Fig. 6.2 for temperatures 10, 5 and 3 K by arrows. The opposite direction and the equal absolute value for the opposite polarizations is in agreement with the expected relation  $\chi_{ab} \propto P_0$ . From now on  $t_{\perp}$  will denote corrected values of the crossed amplitude and the index “corr” will be omitted.

## 6.4 Direct observation of dynamic magnetoelectric susceptibility

Figure 6.3(a) shows a typical result of the experiment in crossed polarizers geometry. We note that crossed polarizers separate the incident polarization from the induced one. Immediately upon the onset of the ferroelectric phase, distinct polarization rotation is observed with the sign of the signal correlating with the sign of the static field (Fig. 6.3(a)). Here we plot the clockwise rotation of the polarization as a positive signal and the counterclockwise rotation

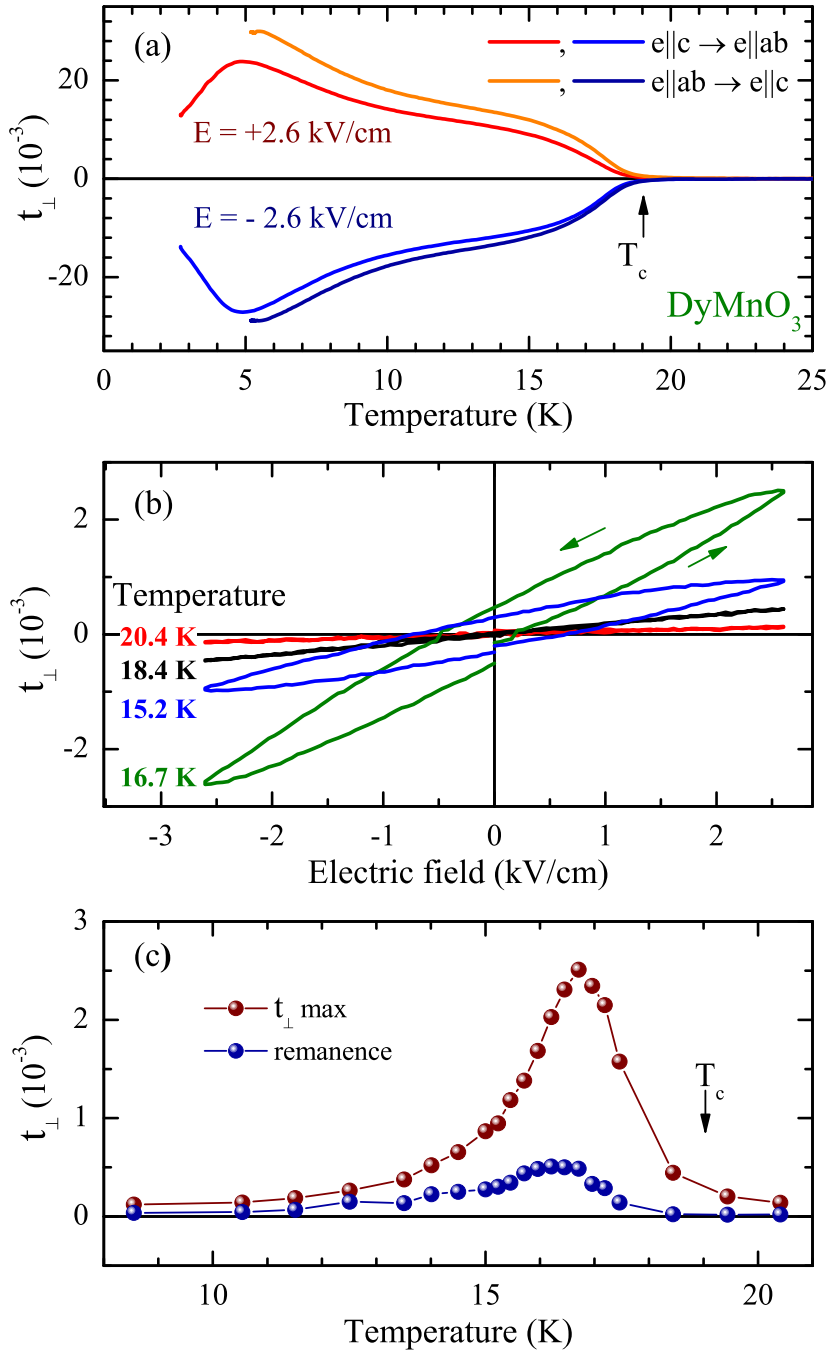


**Figure 6.3:** Controlling of terahertz light by static electric field in  $\text{DyMnO}_3$ . (a) – transmitted terahertz signal in  $\text{DyMnO}_3$  at  $\nu = 210$  GHz in crossed polarizers for different polarizations and poling electric fields (field-cooling). The geometry of the experiment is given in Fig. 6.1(b). The notation  $e\parallel ab$  is equivalent to  $e\perp c$  in Fig. 6.1(b). Positive and negative sign of  $t_{\perp}$  reflects clockwise and counterclockwise polarization rotation, respectively. Arrow indicates the phase transition to the ferroelectric phase. (b) – electric voltage dependencies of the transmission in crossed polarizers for various temperatures and for the zero-field cooled (ZFC) sample. (c) – maximum available signal in crossed polarizers and the remanence signal as a function of temperature in ZFC case. Symbols – experiment, lines are to guide the eye.

as a negative signal. Equivalently, the positive and negative sign of  $t_{\perp}$  reflects the  $180^{\circ}$  phase difference between the experimental signal for different sign of the static electric field. These results demonstrate the validity of the qualitative arguments given above.

Another important result is shown in Figs. 6.3(b, c). Here, not far from the phase transition into the ordered state, the ferroelectric domains may be switched by a moderate static field. Due to the direct coupling of static and dynamic properties, the sign of the magnetoelectric susceptibility is switched as well. Therefore, in this range we can directly influence the signal  $t_{\perp}$  and the polarization rotation of the terahertz radiation by the static electric field.

A significant difference between the experiments in Figs. 6.3(a, c) is that a field-cooling experiment is performed in the first case and a zero-field-cooled experiment in the second case. Because in the field-cooled case the sample is cooled starting from the paraelectric state, it is much easier to align the ferroelectric domains by the static field. In the zero-field-cooled sample at low temperatures the coercive field is strong and the static electric field cannot reorient the domains. The reorientation of the domains takes place close to the ferroelectric transition only, which explains the maxima observed in Figs. 6.3(c). Finally, we note that the effects in Figs. 6.3(a, b) are due to the same microscopic mechanism, but a direct switching of polarization in Fig. 6.3(b) is more relevant from the point of view of possible applications.

In order to prove the proposed mechanism of the polarization rotation, a series of spectroscopic experiments has been carried out. The terahertz dynamics in our frequency range is dominated by a strong electromagnon at about 550 GHz ( $18 \text{ cm}^{-1}$ ). This electromagnon is responsible for a relatively low transmission in the geometry with  $e \parallel a$ , seen as blue symbols in Fig. 6.4(a). This excitation most probably originates from the symmetric Heisenberg exchange mechanism [99, 100, 112] and it does not contribute to the magnetoelectric effects.

In the transmission spectra  $e \parallel a$  another weaker excitation can be seen close to 210 GHz. This mode is observed both in the geometry  $e \parallel a$  (Fig. 6.4(a), red curve) as well as in the perpendicular geometry  $e \parallel c$ , Fig. 6.4(c). In the latter geometry the sample is more transparent as the main absorption mechanism due to the Heisenberg exchange with the component  $e \parallel a$  is absent. In close analogy to a similar spectral analysis [105] in  $\text{TbMnO}_3$ , the mode at 210 GHz can be attributed to the zone-center eigenmode of the cycloidal structure. This mode gets its intensity predominantly due to the Dzyaloshinskii-Moriya mechanism. Because the static electric polarization is governed by the same mechanism, static and dynamic properties are strongly correlated for the 210 GHz mode. As discussed above, this connection is the basic mechanism to produce electrically controlled rotation of the terahertz polarization.

The mode of the cycloidal spin structure at 210 GHz reveals nonzero electric  $\chi_a^e$ , magnetic  $\chi_b^m$ , and magnetoelectric  $\chi_{ab}^{me}$  susceptibilities [110]. This mode can be excited by both, an  $ac$  electric field  $e \parallel a$  and  $ac$  magnetic field  $h \parallel b$  and can be therefore called a DM electromagnon. In agreement with these arguments, the rotation of the polarization is the strongest close to 210 GHz and fades away on both sides of the resonance. This result is shown in Fig. 6.4(a) with black squares. Green solid line represents the result of calculations of the transmission in crossed polarizers assuming Lorentz line shape of the DM electromagnon at 210 GHz. Tiny oscillations in this curve reflect the Fabry-Pérot resonances on the sample surfaces. In order to obtain the magnetoelectric susceptibility directly from the measured transmission, the complex transmission matrix has been inverted numerically. The frequency dependence of a resulting magnetoelectric susceptibility in  $\text{DyMnO}_3$  is shown in Fig. 6.4(b) by black symbols.



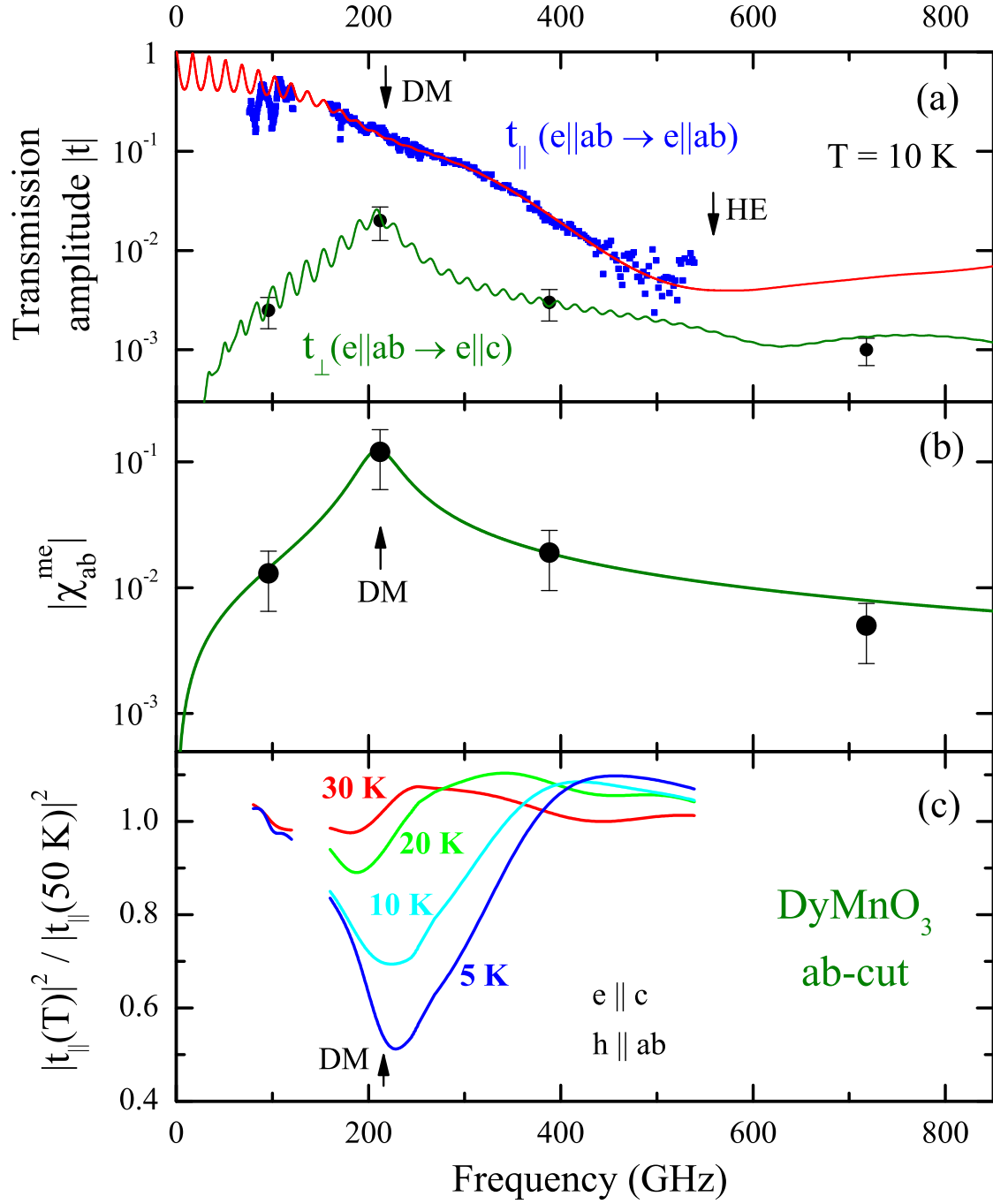


**Figure 6.4:** Electromagnons in  $\text{DyMnO}_3$ . (a) – transmission spectra of  $\text{DyMnO}_3$  in parallel (blue symbols) and crossed (black symbols) polarizers. The transmission is dominated by the Heisenberg electromagnon at 550 GHz (marked as HE). Much weaker Dzyaloshinskii-Moriya electromagnon (marked as DM) at 210 GHz is responsible for the observed dynamic magnetoelectric effect and for nonzero signal in crossed polarizers. Symbols – experiment, lines are fits according to Fresnel optical equations. (b) – magnetoelectric susceptibility as obtained from the spectra in (a). (c) – transmission in parallel polarizers and in the transparent geometry with  $e \parallel c$  showing the magnetically excited DM electromagnon.

In spite of the complexity of the data treatment, a nonzero signal in crossed polarizers is to a leading term directly proportional to  $\chi_{ab}^{me}$ . This explains a qualitative similarity of the frequency dependencies of  $t_{\perp}(\nu)$  and  $\chi_{ab}^{me}(\nu)$  in Fig. 6.4(a, b).

From the Lorentzian fits in Fig. 6.4 the intensities of the DM electromagnon are obtained as follows: electric contribution  $\Delta\varepsilon_a = 1.7 \pm 0.3$ , from Fig. 6.4(a); magnetic contribution  $\Delta\mu_b = 0.010 \pm 0.002$ , from Fig. 6.4(c); magnetoelectric contribution:  $\Delta\chi_{ab}^{me} = 0.03 \pm 0.01$ , from Fig. 6.4(b). We see that the universality condition is not fulfilled in  $\text{DyMnO}_3$ :  $\sqrt{\Delta\varepsilon_a \Delta\mu_b} = 0.13 > \chi_{ab}^{me}$ . This disagreement most probably indicates that a large part of the DM electromagnon spectral weight is provided by the Heisenberg exchange mechanism. Indeed, a theoretical estimate of the electric contribution [99] gives the value  $\Delta\varepsilon_a \approx 0.2$  substantially smaller than the experimental result.

In orthorhombic rare earth manganites ( $\text{RMnO}_3$ ,  $R = \text{Dy, Tb, Eu:Y}$ ) strong zone edge electromagnons in the terahertz spectra are due to symmetric Heisenberg exchange mechanism. However, their properties do not correlate with the behavior of the static electric polarization, because the latter is due to antisymmetric Dzyaloshinskii-Moriya coupling. On the contrary, in the present experiments the static and dynamic properties are controlled by the same DM mechanism, which explains the observed voltage control of the terahertz radiation.

Finally, the observed results differ from such well-known effect like electro-optical modulation [113] (Pockels effect). Several arguments support this statement: i) The frequency dependence of the observed magnetoelectric signal follows the Lorentzian line shape of the DM electromagnon. ii) The observed signal qualitatively follows the ferroelectric polarization (Fig. 6.3(a)) and disappears in the unpoled sample at low temperatures (Fig. 6.3(c)). iii) Cooling down with applied voltage that is twice smaller results in the same crossed amplitude. This smaller voltage is still sufficient to pole the sample completely and the effect does not depend on the magnitude of the static electric field.

## 6.5 Conclusion

In conclusion, dynamic magnetoelectric effect based on DM electromagnon in  $\text{DyMnO}_3$  was investigated. Because of the off-diagonal elements of the magnetoelectric susceptibility a polarization plane rotation of the transmitted radiation is observed. The amplitude and the direction of the polarization rotation can be controlled and switched by static electric voltage. From the spectral analysis a full set of magnetic, electric, and magnetoelectric susceptibilities of the DM electromagnon in  $\text{DyMnO}_3$  is obtained.

## 7 Summary and outlook

This work presents a spectroscopic study of several low-temperature phenomena in the far-IR range. The most important results have been obtained in those experiments, in which the interaction of THz radiation with the sample under study leads to rotation of the polarization plane. Since the typical rotation angles are small (several milliradians), they need to be separated from side contributions. Two key requirements must be satisfied for this separation. First, the effect of rotation must be “switchable”: one needs a possibility to suppress or reverse the rotation, caused by the sample, without any change in the surrounding objects that can affect the propagation of radiation. In experiments with two-dimensional electron gases in an external magnetic field the Faraday rotation changes its sign upon reversing the magnetic field. In experiments with dysprosium manganite the sign of rotation was connected to the orientation of ferroelectric domains and could be switched by a static electric field. The second requirement is an ability to measure the complex phase of the transmitted wave. Analysis of transmission data suggests that the effect of the sample and the side contribution add up as complex numbers. Thus in order to recover the effect of the sample, both the real and imaginary parts of the transmission coefficient must be measured (or, equally, both the amplitude and the phase).

Measurements of rotation of the polarization plane in dysprosium manganite allowed a direct observation of the dynamic magnetoelectric effect. It has been known that static antiferromagnetic and ferroelectric orders are coupled in this material below 19 K. Theoretical consideration of excitations showed existence of a mode, in which the net electric moment oscillates along the  $a$ -axis and the magnetic moment oscillates along the  $b$ -axis. In a specially cut sample, an excitation of this mode leads to the rotation of the polarization plane, the rotation angle being proportional to the dynamic magnetoelectric susceptibility  $\chi_{ab}$ . The sign of  $\chi_{ab}$  is determined by the orientation of the ferroelectric domain (parallel or antiparallel to  $c$ -axis). In the vicinity of the critical temperature the orientation of domains can be switched by a moderate static electric field. These properties allowed to demonstrate an interesting concept: a possibility to control the THz radiation by electric voltage using the electromagnon. Much stronger magnetoelectric effects have been recently demonstrated in similar experiments with samarium ferborate [114–116].

Properties of the mercury telluride thin films with critical thickness have been investigated in the terahertz and far-IR ranges. The control of the charge density proved to be an extremely useful tool in this study. It allows to shift the Fermi level and to scan the band structure of the two-dimensional electron systems. The charge density could be controlled in two ways: using a semitransparent gate and using illumination by visible light. Since the ability to shift the Fermi level is a great advantage by itself, let us summarize the disadvantages of both methods that turned out in the experiments. An obvious drawback of illumination is the need to warm up the sample to restore the initial Fermi level. After a cooling the Fermi level takes some ran-

dom value. Thus in order to reproduce a measurement, one needs an accompanying transport experiment for setting the same state of the sample. It remains unclear, how homogeneous is the charge density in the large ( $5 \times 5 \text{ mm}^2$ ) samples after illumination, this question needs further investigations.

A semitransparent gate reduces the transmission coefficients, decreasing the signal to noise ratio. To obtain the Drude parameters of the system, one has to introduce another unknown variable  $\sigma_{\text{gate}}$ , making the fitting procedure less defined. Although the preparation of a gate may seem a simple and straightforward task, it turns out to be challenging in the case of large MBE-grown samples and low temperatures. Normally a working MBE-grown gate undergoes an electrical breakdown after one heating from helium to room temperature. The Mylar gates, used in the presented experiments, preserve their insulating properties during the thermal cycling, but they destroy the sample mechanically instead. The Mylar gates are hard to be made homogeneous and they demonstrate large hysteresis effects, caused by polarization of the insulator. Further complications with the gated samples occur, when one tries to carry out accompanying transport measurements. In order to make a contact, one needs a region of the sample that is not covered by the gate. This uncovered region affects the DC resistances, limiting the transport measurements by a single zero voltage. Thus a semi-transparent gate that does not cover the whole sample becomes a disadvantage in the case, when the main goal is to compare static conductivities with dynamic ones.

In HgTe films with the critical thickness the charge carrier concentration could be modified by more than one order of magnitude using optical doping by visible light illumination. In some cases, using light as a parameter may switch the qualitative electrodynamic response from hole-like to the electron-like. For the electrons, the cyclotron mass shows a square root dependence upon the charge concentration. This can be interpreted as a clear proof of a linear dispersion relations, i.e. Dirac type carriers. The use of semitransparent gates allowed to directly obtain the band structure of a two-dimensional Dirac semi-metal from the doping dependence of the cyclotron resonance. A linear Dirac-like dispersion on the hole side of the band structure and detectable quadratic corrections for the electrons have been observed. This procedure to obtain the band structure is especially useful for thin films where protective layers impede such standard techniques as angular resolved photoemission spectroscopy. Finally, the dynamic quantum Hall effect has been demonstrated on holes at frequencies above 300 GHz. This observation led to the idea to investigate the dynamic QHE in GaAs/AlGaAs heterojunctions.

The dynamic Hall conductivity of GaAs/AlGaAs heterojunctions has been studied in the range 70–1100 GHz. The spectroscopic experiments were accompanied by simultaneous transport measurements of static resistances in the van der Pauw geometry. Such setup allowed the most direct comparison of static and dynamic conductivities, obtained in exactly the same conditions. Quantization of dynamic Hall conductivity has been observed at frequencies below  $\approx 100 \text{ GHz}$ . Above this frequency the Hall conductivity was found to tend to classical behavior: plateaus are replaced by small oscillations around a nearly straight line  $\sigma \propto B^{-1}$ . The amplitude of these oscillations decreases with increasing frequency and at  $\approx 1 \text{ THz}$  the Hall conductivity follows the classical Drude model. While in the static case the imaginary part of  $\sigma_{xy}$  is zero, in the range 70–1100 GHz  $\text{Im } \sigma_{xy}$  was found to demonstrate quantum oscillations that are periodic in the inverse magnetic field. The observation of the oscillations

---

in  $\text{Im } \sigma_{xy}$  became possible due to the ability to measure the complex phase of transmission coefficients, especially of the crossed coefficient  $t_{\perp}$ . Recent numerical calculations for a realistic intermediate potential, using the method of exact diagonalization, predict persistence of the plateaus in the THz range. This prediction was not confirmed in the presented experiments. The breakdown of quantization at  $\approx 100$  GHz is in agreement with two analytical models, using the opposite limits of the impurity potential: short-range  $\delta$ -impurities and a smoothly varying potential. The critical frequency in these models is determined by the width of the broadened Landau levels. Estimation of the width, based on electron mobility, results in the correct critical frequency of the observed breakdown. At the same time, the experimental shape of the distorted plateaus is not described by these models. In order to verify, how universal is the relation of the breakdown frequency with the width of Landau levels, experimental study on various systems with different mobilities is needed. Such experiments on GaAs/AlGaAs and HgTe/CdHgTe quantum wells are already planned. Thus we can expect further progress in understanding of the dynamic QHE in the near future.



# Acknowledgments

I thank the following people:

- Prof. Andrei Pimenov for the valuable guidance, for giving me freedom of choosing my research topics and for the careful proofreading of the manuscript.
- Dr. Alexey Shuvaev for the generous sharing of his experience in physics and computer technologies.
- Dr. Sebastian Engelbrecht for the introduction into experimental sub-THz spectroscopy.
- Prof. Dimitri Basov for giving me the opportunity to extend my range above 1.2 THz and for the valuable advices on preparation of manuscripts.
- Dr. Andre Vogel, Michaela Pail, Martina Lexner and, of course, Stephanie Wogowitsch for their exemplary administrative work and readiness to help.
- Nathan Armstrong, Dr. Aliaksei Charnukha, Kirk Post and Yinming Shao for the introduction into FTIR technique. Special thanks goes to Nathan for his demonstration of the right way of doing any painstaking job.
- Don Macfarland for growing the GaAs/AlGaAs heterostructures.
- Andreas Lahner and the whole staff of the TU workshop for their technical support.
- Dr. Artem Kuzmenko for the valuable discussions of physics of multiferroics.
- Prof. Yuri Lozovik for the valuable discussion of the dynamic QHE.
- Dr. Anton Shchepetilnikov for the indium contacts and for the theory of two-dimensional systems.
- Anna Pimenov for the help with the sample preparation.
- Lukas Weymann for the Kurzfassung and for maintaining silence in the low-frequency acoustic range.
- My colleagues Dr. Markus Schiebl, Dr. Graeme Johnstone, Dr. Enda Scally, Thomas Kain, Dr. David Szaller, Dr. Evan Constable, Jan Gospodaric, Lorenz Bergen, and Siyuan Dai for the friendly working atmosphere and their constant optimism.
- My family, who contributed into accomplishment of this work indirectly, via love and moral support.





# Bibliography

- [1] C. Burgess, K. D. Mielenz. *Aspects of the development of colorimetric analysis and quantitative molecular spectroscopy in the ultraviolet-visible region*. Elsevier Science Publishers. ISBN 9780444599056 (1987)
- [2] G. V. Kozlov, A. A. Volkov, C. Dahl, L. Genzel, P. Goy, J. P. Kotthaus, M. C. Nuss, J. Orenstein, G. Grüner. *Coherent Source Submillimeter Wave Spectroscopy*. Springer (1998)
- [3] B. A. Bernevig, T. L. Hughes, S.-C. Zhang. *Quantum Spin Hall Effect and Topological Phase Transition in HgTe Quantum Wells*. *Science* **314**, 5806, p. 1757 (2006), URL <http://www.sciencemag.org/content/314/5806/1757.abstract>
- [4] J. B. Oostinga, L. Maier, P. Schüffegen, D. Knott, C. Ames, C. Brüne, G. Tkachov, H. Buhmann, L. W. Molenkamp. *Josephson Supercurrent through the Topological Surface States of Strained Bulk HgTe*. *Phys. Rev. X* **3**, p. 021007 (2013), URL <https://link.aps.org/doi/10.1103/PhysRevX.3.021007>
- [5] A. Pfeuffer-Jeschke. *Bandstruktur und Landau-Niveaus quecksilberhaltiger II-VI Heterostrukturen*. Ph.D. thesis, University of Wuerzburg (2000)
- [6] Z. D. Kvon, E. B. Olshanetsky, N. N. Mikhailov, D. A. Kozlov. *Two-dimensional electron systems in HgTe quantum wells*. *Low Temp. Phys.* **35**, 1, p. 6 (2009), URL <http://dx.doi.org/10.1063/1.3064862>
- [7] R. Prange, S. Girvin. *The Quantum Hall effect*. Springer-Verlag. ISBN 9783540962861 (1987), URL <https://books.google.at/books?id=Y7XvAAAAMAAJ>
- [8] F. Kuchar, R. Meisels, G. Weimann, W. Schlapp. *Microwave Hall conductivity of the two-dimensional electron gas in GaAs-Al<sub>x</sub>Ga<sub>1-x</sub>As*. *Phys. Rev. B* **33**, p. 2965 (1986), URL <https://link.aps.org/doi/10.1103/PhysRevB.33.2965>
- [9] L. A. Galchenkov, I. M. Grodnenskii, M. V. Kostovetskii, O. R. Matov. *Frequency dependence of the Hall conductivity of a 2D electron gas*. *JETP Lett.* **46**, p. 542 (1987), URL [http://www.jetpletters.ac.ru/ps/1234/article\\_18636.shtml](http://www.jetpletters.ac.ru/ps/1234/article_18636.shtml)
- [10] T. Morimoto, Y. Hatsugai, H. Aoki. *Optical Hall Conductivity in Ordinary and Graphene Quantum Hall Systems*. *Phys. Rev. Lett.* **103**, p. 116803 (2009), URL <https://link.aps.org/doi/10.1103/PhysRevLett.103.116803>

- [11] T. Morimoto, Y. Avishai, H. Aoki. *Dynamical scaling analysis of the optical Hall conductivity in the quantum Hall regime*. Phys. Rev. B **82**, p. 081404 (2010), URL <https://link.aps.org/doi/10.1103/PhysRevB.82.081404>
- [12] S. M. Apenko, Y. E. Lozovik. *Quantization of the Hall conductivity of a two-dimensional electron gas in a strong magnetic field*. JETP **62**, p. 328 (1985), URL <http://www.jetp.ac.ru/cgi-bin/r/index/e/62/2/p328?a=list>
- [13] Y. E. Lozovik, V. M. Farztdinov, Z. S. Gevorkyan. *Dynamic quantum Hall effect*. JETP Lett. **39**, p. 179 (1984), URL [http://www.jetpletters.ac.ru/ps/1287/article\\_19439.shtml](http://www.jetpletters.ac.ru/ps/1287/article_19439.shtml)
- [14] M. Bibes, A. Barthelemy. *Multiferroics: Towards a magnetoelectric memory*. Nature Materials **7**, 6, p. 425 (2008), URL <https://www.nature.com/articles/nmat2189>
- [15] S. Teitler, B. W. Henvis. *Refraction in stratified, anisotropic media*. J. Opt. Soc. Am. **60**, 6, p. 830 (1970), URL <http://www.osapublishing.org/abstract.cfm?URI=josa-60-6-830>
- [16] D. W. Berreman. *Optics in Stratified and Anisotropic Media: 4x4-Matrix Formulation*. J. Opt. Soc. Am. **62**, 4, p. 502 (1972), URL <http://www.osapublishing.org/abstract.cfm?URI=josa-62-4-502>
- [17] E. D. Palik, J. K. Furdyna. *Infrared and microwave magnetoplasma effects in semiconductors*. Rep. Prog. Phys. **33**, 3, p. 1193 (1970), URL <http://stacks.iop.org/0034-4885/33/i=3/a=307>
- [18] N. Ashcroft, N. Mermin. *Solid state physics*. Saunders College (1976)
- [19] P. Drude. *Zur Elektronentheorie der Metalle*. Annalen der Physik **1**, p. 566 (1900), URL <http://dx.doi.org/10.1002/andp.19003060312>
- [20] P. Drude. *Zur Elektronentheorie der Metalle. Galvanomagnetische und thermomagnetische Effecte*. Annalen der Physik **3**, p. 369 (1900), URL <http://dx.doi.org/10.1002/andp.19003081102>
- [21] A. Abrikosov. *Fundamentals of the Theory of Metals*. Dover Publications. ISBN 9780486819013 (2017), URL <https://books.google.at/books?id=tTo2DwAAQBAJ>
- [22] F. Blatt. *Theory of mobility of electrons in solids*. Academic Press Inc (1957)
- [23] A. Animalu. *Intermediate quantum theory of crystalline solids*. Prentice-Hall Inc (1977), URL [https://www.researchgate.net/profile/Alexander\\_Animalu/publication/292153026\\_Intermediate\\_Quantum\\_Theory\\_of\\_Crystalline\\_Solids/links/56ab633108aed814bdea13e2/Intermediate-Quantum-Theory-of-Crystalline-Solids.pdf](https://www.researchgate.net/profile/Alexander_Animalu/publication/292153026_Intermediate_Quantum_Theory_of_Crystalline_Solids/links/56ab633108aed814bdea13e2/Intermediate-Quantum-Theory-of-Crystalline-Solids.pdf)

- 
- [24] R. H. Dicke. *Coherence in Spontaneous Radiation Processes*. Phys. Rev. **93**, p. 99 (1954), URL <https://link.aps.org/doi/10.1103/PhysRev.93.99>
- [25] Q. Zhang, T. Arikawa, E. Kato, J. L. Reno, W. Pan, J. D. Watson, M. J. Manfra, M. A. Zudov, M. Tokman, M. Erukhimova, A. Belyanin, J. Kono. *Superradiant Decay of Cyclotron Resonance of Two-Dimensional Electron Gases*. Phys. Rev. Lett. **113**, p. 047601 (2014), URL <https://link.aps.org/doi/10.1103/PhysRevLett.113.047601>
- [26] M. Z. Hasan, C. L. Kane. *Colloquium: Topological insulators*. Rev. Mod. Phys. **82**, p. 3045 (2010), URL <http://link.aps.org/doi/10.1103/RevModPhys.82.3045>
- [27] X.-L. Qi, T. L. Hughes, S.-C. Zhang. *Topological field theory of time-reversal invariant insulators*. Phys. Rev. B **78**, p. 195424 (2008), URL <http://link.aps.org/doi/10.1103/PhysRevB.78.195424>
- [28] W.-K. Tse, A. H. MacDonald. *Giant Magneto-Optical Kerr Effect and Universal Faraday Effect in Thin-Film Topological Insulators*. Phys. Rev. Lett. **105**, p. 057401 (2010), URL <http://link.aps.org/doi/10.1103/PhysRevLett.105.057401>
- [29] W.-K. Tse, A. H. MacDonald. *Magneto-optical Faraday and Kerr effects in topological insulator films and in other layered quantized Hall systems*. Phys. Rev. B **84**, p. 205327 (2011), URL <http://link.aps.org/doi/10.1103/PhysRevB.84.205327>
- [30] J. Maciejko, X.-L. Qi, H. D. Drew, S.-C. Zhang. *Topological Quantization in Units of the Fine Structure Constant*. Phys. Rev. Lett. **105**, p. 166803 (2010), URL <http://link.aps.org/doi/10.1103/PhysRevLett.105.166803>
- [31] G. Tkachov, E. M. Hankiewicz. *Anomalous galvanomagnetism, cyclotron resonance, and microwave spectroscopy of topological insulators*. Phys. Rev. B **84**, p. 035405 (2011), URL <http://link.aps.org/doi/10.1103/PhysRevB.84.035405>
- [32] V. Latussek. *Elektronische Zustände in Typ-III-Halbleiterheterostrukturen*. Ph.D. thesis, University of Wuerzburg (2004)
- [33] B. Büttner, C. X. Liu, G. Tkachov, E. G. Novik, C. Brüne, H. Buhmann, E. M. Hankiewicz, P. Recher, B. Trauzettel, S. C. Zhang, L. W. Molenkamp. *Single valley Dirac fermions in zero-gap HgTe quantum wells*. Nat. Phys. **7**, 5, p. 418 (2011)
- [34] A. M. Shuvaev, G. V. Astakhov, A. Pimenov, C. Brüne, H. Buhmann, L. W. Molenkamp. *Giant Magneto-Optical Faraday Effect in HgTe Thin Films in the Terahertz Spectral Range*. Phys. Rev. Lett. **106**, p. 107404 (2011), URL <http://link.aps.org/doi/10.1103/PhysRevLett.106.107404>

- [35] J. N. Hancock, J. L. M. van Mechelen, A. B. Kuzmenko, D. van der Marel, C. Brüne, E. G. Novik, G. V. Astakhov, H. Buhmann, L. W. Molenkamp. *Surface State Charge Dynamics of a High-Mobility Three-Dimensional Topological Insulator*. Phys. Rev. Lett. **107**, p. 136803 (2011), URL <http://link.aps.org/doi/10.1103/PhysRevLett.107.136803>
- [36] A. M. Shuvaev, G. V. Astakhov, G. Tkachov, C. Brüne, H. Buhmann, L. W. Molenkamp, A. Pimenov. *Terahertz quantum Hall effect of Dirac fermions in a topological insulator*. Phys. Rev. B **87**, p. 121104 (2013), URL <http://link.aps.org/doi/10.1103/PhysRevB.87.121104>
- [37] Z. D. Kvon, S. N. Danilov, D. A. Kozlov, C. Zoth, N. N. Mikhailov, S. A. Dvoretiskii, S. D. Ganichev. *Cyclotron resonance of Dirac fermions in HgTe quantum wells*. JETP Letters **94**, 11, p. 816 (2012), URL <https://doi.org/10.1134/S002136401123007X>
- [38] A. V. Ikonnikov, M. S. Zholudev, K. E. Spirin, A. A. Lastovkin, K. V. Maremyanin, V. Y. Aleshkin, V. I. Gavrilenko, O. Drachenko, M. Helm, J. Wosnitza, M. Goiran, N. N. Mikhailov, S. A. Dvoretiskii, F. Teppe, N. Diakonova, C. Consejo, B. Chenaud, W. Knap. *Cyclotron resonance and interband optical transitions in HgTe/CdTe (013) quantum well heterostructures*. Semicond. Sci. Technol. **26**, 12, p. 125011 (2011), URL <http://stacks.iop.org/0268-1242/26/i=12/a=125011>
- [39] P. Olbrich, C. Zoth, P. Vierling, K.-M. Dantscher, G. V. Budkin, S. A. Tarasenko, V. V. Bel'kov, D. A. Kozlov, Z. D. Kvon, N. N. Mikhailov, S. A. Dvoretzky, S. D. Ganichev. *Giant photocurrents in a Dirac fermion system at cyclotron resonance*. Phys. Rev. B **87**, p. 235439 (2013), URL <https://link.aps.org/doi/10.1103/PhysRevB.87.235439>
- [40] C. Zoth, P. Olbrich, P. Vierling, K.-M. Dantscher, V. V. Bel'kov, M. A. Semina, M. M. Glazov, L. E. Golub, D. A. Kozlov, Z. D. Kvon, N. N. Mikhailov, S. A. Dvoretzky, S. D. Ganichev. *Quantum oscillations of photocurrents in HgTe quantum wells with Dirac and parabolic dispersions*. Phys. Rev. B **90**, p. 205415 (2014), URL <http://link.aps.org/doi/10.1103/PhysRevB.90.205415>
- [41] V. Varavin, S. Dvoretzky, V. Liberman, N. Mikhailov, Y. Sidorov. *Molecular beam epitaxy of high quality  $Hg_{1-x}Cd_xTe$  films with control of the composition distribution*. Journal of Crystal Growth **159**, 1, p. 1161 (1996), URL <http://www.sciencedirect.com/science/article/pii/0022024895008454>
- [42] M. König, S. Wiedmann, C. Brüne, A. Roth, H. Buhmann, L. W. Molenkamp, X.-L. Qi, S.-C. Zhang. *Quantum Spin Hall Insulator State in HgTe Quantum Wells*. Science **318**, 5851, p. 766 (2007), URL <http://www.sciencemag.org/content/318/5851/766.abstract>

- 
- [43] A. H. Castro Neto, F. Guinea, N. M. R. Peres, K. S. Novoselov, A. K. Geim. *The electronic properties of graphene*. Rev. Mod. Phys. **81**, p. 109 (2009), URL <http://link.aps.org/doi/10.1103/RevModPhys.81.109>
- [44] M. I. Nathan. *Persistent photoconductivity in AlGaAs/GaAs modulation doped layers and field effect transistors: A review*. Solid-State Electronics **29**, 2, p. 167 (1986), URL <http://www.sciencedirect.com/science/article/pii/0038110186900353>
- [45] A. M. Shuvaev, G. V. Astakhov, C. Brüne, H. Buhmann, L. W. Molenkamp, A. Pimenov. *Terahertz magneto-optical spectroscopy in HgTe thin films*. Semicond. Sci. Technol. **27**, 12, p. 124004 (2012), URL <http://stacks.iop.org/0268-1242/27/i=12/a=124004>
- [46] K. S. Novoselov, A. K. Geim, S. V. Morozov, D. Jiang, M. I. Katsnelson, I. V. Grigorieva, S. V. Dubonos, A. A. Firsov. *Two-dimensional gas of massless Dirac fermions in graphene*. Nature **438**, p. 197 (2005)
- [47] Z.-D. Kvon, S. N. Danilov, N. N. Mikhailov, S. A. Dvoretzky, W. Prettl, S. D. Ganichev. *Cyclotron resonance photoconductivity of a two-dimensional electron gas in HgTe quantum wells*. Physica E **40**, 6, p. 1885 (2008), URL <http://www.sciencedirect.com/science/article/pii/S1386947707003645>
- [48] A. Ikonnikov, A. Lastovkin, K. Spirin, M. Zholudev, V. Rumyantsev, K. Maremyanin, A. Antonov, V. Aleshkin, V. Gavrilenko, S. Dvoretzskii, N. Mikhailov, Y. Sadofyev, N. Samal. *Terahertz spectroscopy of quantum-well narrow-bandgap HgTe/CdTe-based heterostructures*. JETP Lett. **92**, 11, p. 756 (2010), URL <http://dx.doi.org/10.1134/S0021364010230086>
- [49] C. Kant. *Probing spins and phonons with light. Optical spectroscopy on transition-metal monoxides*. Ph.D. thesis, University of Augsburg (2010)
- [50] Y. Shao, K. W. Post, J.-S. Wu, S. Dai, A. J. Frenzel, A. R. Richardella, J. S. Lee, N. Samarth, M. M. Fogler, A. V. Balatsky, D. E. Kharzeev, D. N. Basov. *Faraday Rotation Due to Surface States in the Topological Insulator  $(\text{Bi}_{1-x}\text{Sb}_x)_2\text{Te}_3$* . Nano Lett. **17**, 2, p. 980 (2017), URL <http://dx.doi.org/10.1021/acs.nanolett.6b04313>
- [51] J. Ludwig, Y. B. Vasilyev, N. N. Mikhailov, J. M. Poumirol, Z. Jiang, O. Vafek, D. Smirnov. *Cyclotron resonance of single-valley Dirac fermions in nearly gapless HgTe quantum wells*. Phys. Rev. B **89**, p. 241406 (2014), URL <http://link.aps.org/doi/10.1103/PhysRevB.89.241406>
- [52] M. Hass, B. Henvis. *Infrared lattice reflection spectra of III-V compound semiconductors*. Journal of Physics and Chemistry of Solids **23**, 8, p. 1099. ISSN 0022-3697 (1962), URL <http://www.sciencedirect.com/science/article/pii/0022369762901270>

- [53] E. M. Sheregii, J. Cebulski, A. Marcelli, M. Piccinini. *Temperature Dependence Discontinuity of the Phonon Mode Frequencies Caused by a Zero-Gap State in HgCdTe Alloys*. Phys. Rev. Lett. **102**, p. 045504 (2009), URL <https://link.aps.org/doi/10.1103/PhysRevLett.102.045504>
- [54] J. Chu, A. Sher. *Physics and Properties of Narrow Gap Semiconductors*. Springer New York (2007)
- [55] J. W. McClure. *Diamagnetism of Graphite*. Phys. Rev. **104**, p. 666 (1956), URL <https://link.aps.org/doi/10.1103/PhysRev.104.666>
- [56] J. M. Luttinger, W. Kohn. *Motion of Electrons and Holes in Perturbed Periodic Fields*. Phys. Rev. **97**, p. 869 (1955), URL <https://link.aps.org/doi/10.1103/PhysRev.97.869>
- [57] D. A. Kozlov, M. L. Savchenko, J. Ziegler, Z. D. Kvon, N. N. Mikhailov, S. A. Dvoretiskii, D. Weiss. *Capacitance spectroscopy of a system of gapless Dirac fermions in a HgTe quantum well*. JETP Letters **104**, 12, p. 859 (2016), URL <https://doi.org/10.1134/S0021364016240103>
- [58] W.-K. Tse, A. H. MacDonald. *Magneto-optical and magnetoelectric effects of topological insulators in quantizing magnetic fields*. Phys. Rev. B **82**, p. 161104 (2010), URL <http://link.aps.org/doi/10.1103/PhysRevB.82.161104>
- [59] R. Shimano, G. Yumoto, J. Y. Yoo, R. Matsunaga, S. Tanabe, H. Hibino, T. Morimoto, H. Aoki. *Quantum Faraday and Kerr rotations in graphene*. Nat. Commun. **4**, p. 1841 (2013), URL <http://dx.doi.org/10.1038/ncomms2866>
- [60] K. N. Okada, Y. Takahashi, M. Mogi, R. Yoshimi, A. Tsukazaki, K. S. Takahashi, N. Ogawa, M. Kawasaki, Y. Tokura. *Observation of topological Faraday and Kerr rotations in quantum anomalous Hall state by terahertz magneto-optics*. Nat. Commun. **7**, p. 12245 (2016), URL <http://www.nature.com/ncomms/2016/160720/ncomms12245/full/ncomms12245.html>
- [61] L. Wu, M. Salehi, N. Koirala, J. Moon, S. Oh, N. P. Armitage. *Quantized Faraday and Kerr rotation and axion electrodynamics of a 3D topological insulator*. Science **354**, p. 1124 (2016), URL <http://dx.doi.org/10.1126/science.aaf5541>
- [62] V. A. Volkov, S. A. Mikhailov. *Quantization of the Faraday effect in systems with a quantum Hall effect*. JETP Lett. **41**, 9, p. 476 (1985), URL [http://jetpletters.ac.ru/ps/1467/article\\_22375.shtml](http://jetpletters.ac.ru/ps/1467/article_22375.shtml)
- [63] V. Dziom, A. Shuvaev, N. N. Mikhailov, A. Pimenov. *Terahertz properties of Dirac fermions in HgTe films with optical doping*. 2D Materials **4**, 2, p. 024005 (2017), URL <http://stacks.iop.org/2053-1583/4/i=2/a=024005>



- 
- [64] A. Shuvaev, A. Pimenov, G. V. Astakhov, M. Mühlbauer, C. Brüne, H. Buhmann, L. W. Molenkamp. *Room temperature electrically tunable terahertz Faraday effect*. Appl. Phys. Lett. **102**, 24, p. 241902 (2013), URL <http://link.aip.org/link/?APL/102/241902/1>
- [65] D. A. Kozlov, Z. D. Kvon, N. N. Mikhailov, S. A. Dvoretiskii. *Quantum hall effect in a system of gapless Dirac fermions in HgTe quantum wells*. JETP Lett. **100**, 11, p. 724 (2015), URL <http://dx.doi.org/10.1134/S0021364014230076>
- [66] D. A. Kozlov, Z. D. Kvon, N. N. Mikhailov, S. A. Dvoretzky. *Weak localization of Dirac fermions in HgTe quantum wells*. JETP Letters **96**, 11, p. 730 (2013), URL <http://dx.doi.org/10.1134/S0021364012230099>
- [67] K. v. Klitzing, G. Dorda, M. Pepper. *New Method for High-Accuracy Determination of the Fine-Structure Constant Based on Quantized Hall Resistance*. Phys. Rev. Lett. **45**, p. 494 (1980), URL <https://link.aps.org/doi/10.1103/PhysRevLett.45.494>
- [68] K. N. Okada, Y. Takahashi, M. Mogi, R. Yoshimi, A. Tsukazaki, K. S. Takahashi, N. Ogawa, M. Kawasaki, Y. Tokura. *Terahertz spectroscopy on Faraday and Kerr rotations in a quantum anomalous Hall state*. Nat. Commun. **7**, p. 12245 (2016), URL <http://dx.doi.org/10.1038/ncomms12245>
- [69] V. Dziom, A. Shuvaev, A. Pimenov, G. V. Astakhov, C. Ames, K. Bendias, J. Böttcher, G. Tkachov, E. M. Hankiewicz, C. Brüne, L. W. Buhmann, H. Molenkamp. *Observation of the universal magnetoelectric effect in a 3D topological insulator*. Nat. Commun. **8**, p. 15197 (2017), URL <http://dx.doi.org/10.1038/ncomms15197>
- [70] W.-K. Tse. *Coherent magneto-optical effects in topological insulators: Excitation near the absorption edge*. Phys. Rev. B **94**, p. 125430 (2016), URL <https://link.aps.org/doi/10.1103/PhysRevB.94.125430>
- [71] W.-R. Lee, W.-K. Tse. *Dynamical quantum anomalous Hall effect in strong optical fields*. Phys. Rev. B **95**, p. 201411 (2017), URL <https://link.aps.org/doi/10.1103/PhysRevB.95.201411>
- [72] Y. Ikebe, T. Morimoto, R. Masutomi, T. Okamoto, H. Aoki, R. Shimano. *Optical Hall Effect in the Integer Quantum Hall Regime*. Phys. Rev. Lett. **104**, p. 256802 (2010), URL <https://link.aps.org/doi/10.1103/PhysRevLett.104.256802>
- [73] A. V. Stier, C. T. Ellis, J. Kwon, H. Xing, H. Zhang, D. Eason, G. Strasser, T. Morimoto, H. Aoki, H. Zeng, B. D. McCombe, J. Cerne. *Terahertz Dynamics of a Topologically Protected State: Quantum Hall Effect Plateaus near the Cyclotron Resonance of a Two-Dimensional Electron Gas*. Phys. Rev. Lett. **115**, p. 247401 (2015), URL <https://link.aps.org/doi/10.1103/PhysRevLett.115.247401>

- [74] M. Failla, J. Keller, G. Scalari, C. Maissen, J. Faist, C. Reichl, W. Wegscheider, O. J. Newell, D. R. Leadley, M. Myronov, J. Lloyd-Hughes. *Terahertz quantum Hall effect for spin-split heavy-hole gases in strained Ge quantum wells*. New Journal of Physics **18**, 11, p. 113036 (2016), URL <http://stacks.iop.org/1367-2630/18/i=11/a=113036>
- [75] H. C. Montgomery. *Method for Measuring Electrical Resistivity of Anisotropic Materials*. Journal of Applied Physics **42**, 7, p. 2971 (1971), URL <https://doi.org/10.1063/1.1660656>
- [76] F. Kuchar, R. Meisels, K. Y. Lim, P. Pichler, G. Weimann, W. Schlapp. *Hall Conductivity at Microwave and Submillimeter Frequencies in the Quantum Hall Effect Regime*. Physica Scripta **1987**, T19A, p. 79 (1987), URL <http://stacks.iop.org/1402-4896/1987/i=T19A/a=013>
- [77] R. E. Prange. *Quantized Hall resistance and the measurement of the fine-structure constant*. Phys. Rev. B **23**, p. 4802 (1981), URL <https://link.aps.org/doi/10.1103/PhysRevB.23.4802>
- [78] Y. E. Lozovik. *private communications* (2017)
- [79] T. Ando, Y. Uemura. *Theory of Oscillatory g Factor in an MOS Inversion Layer under Strong Magnetic Fields*. J. Phys. Soc. Japan **37**, 4, p. 1044 (1974), URL <https://doi.org/10.1143/JPSJ.37.1044>
- [80] A. Shuvaev, V. Dziom, Z. D. Kvon, N. N. Mikhailov, A. Pimenov. *Universal Faraday Rotation in HgTe Wells with Critical Thickness*. Phys. Rev. Lett. **117**, p. 117401 (2016), URL <https://link.aps.org/doi/10.1103/PhysRevLett.117.117401>
- [81] S. Iordansky. *On the conductivity of two dimensional electrons in a strong magnetic field*. Solid State Communications **43**, 1, p. 1. ISSN 0038-1098 (1982), URL <http://www.sciencedirect.com/science/article/pii/0038109882911413>
- [82] R. F. Kazarinov, S. Luryi. *Quantum percolation and quantization of Hall resistance in two-dimensional electron gas*. Phys. Rev. B **25**, p. 7626 (1982), URL <https://link.aps.org/doi/10.1103/PhysRevB.25.7626>
- [83] M. Fiebig. *Revival of the magnetoelectric effect*. J. Phys. D: Appl. Phys. **38**, 8, p. R123 (2005), URL <http://stacks.iop.org/0022-3727/38/R123>
- [84] R. Ramesh, N. A. Spaldin. *Multiferroics: progress and prospects in thin films*. Nat. Mater. **6**, 1, p. 21 (2007), URL <http://dx.doi.org/10.1038/nmat1805>
- [85] W. Eerenstein, N. D. Mathur, J. F. Scott. *Multiferroic and magnetoelectric materials*. Nature **442**, 7104, p. 759 (2006), URL <http://dx.doi.org/10.1038/nature05023>



- 
- [86] Y. Tokura. *Multiferroics as Quantum Electromagnets*. Science **312**, 5779, p. 1481 (2006), URL <http://www.sciencemag.org/cgi/reprint/312/5779/1481.pdf>
- [87] S.-W. Cheong, M. Mostovoy. *Multiferroics: a magnetic twist for ferroelectricity*. Nat. Mater. **6**, 1, p. 13 (2007), URL <http://dx.doi.org/10.1038/nmat1804>
- [88] A. Pimenov, A. A. Mukhin, V. Y. Ivanov, V. D. Travkin, A. M. Balbashov, A. Loidl. *Possible evidence for electromagnons in multiferroic manganites*. Nat. Phys. **2**, 2, p. 97 (2006), URL <http://dx.doi.org/10.1038/nphys212>
- [89] N. Kida, S. Kumakura, S. Ishiwata, Y. Taguchi, Y. Tokura. *Gigantic terahertz magnetochromism via electromagnons in the hexaferrite magnet  $Ba_2Mg_2Fe_{12}O_{22}$* . Phys. Rev. B **83**, p. 064422 (2011), URL <http://link.aps.org/doi/10.1103/PhysRevB.83.064422>
- [90] S. Bordacs, I. Kezsmarki, D. Szaller, L. Demko, N. Kida, H. Murakawa, Y. Onose, R. Shimano, T. Room, U. Nagel, S. Miyahara, N. Furukawa, Y. Tokura. *Chirality of matter shows up via spin excitations*. Nat. Phys. **8**, 10, p. 734 (2012)
- [91] I. Kézsmárki, N. Kida, H. Murakawa, S. Bordács, Y. Onose, Y. Tokura. *Enhanced Directional Dichroism of Terahertz Light in Resonance with Magnetic Excitations of the Multiferroic  $Ba_2CoGe_2O_7$  Oxide Compound*. Phys. Rev. Lett. **106**, p. 057403 (2011), URL <http://link.aps.org/doi/10.1103/PhysRevLett.106.057403>
- [92] Y. Takahashi, R. Shimano, Y. Kaneko, H. Murakawa, Y. Tokura. *Magnetoelectric resonance with electromagnons in a perovskite helimagnet*. Nat. Phys. **8**, 2, p. 121 (2012)
- [93] Y. Takahashi, Y. Yamasaki, Y. Tokura. *Terahertz Magnetoelectric Resonance Enhanced by Mutual Coupling of Electromagnons*. Phys. Rev. Lett. **111**, p. 037204 (2013), URL <http://link.aps.org/doi/10.1103/PhysRevLett.111.037204>
- [94] P. Rovillain, R. de Sousa, Y. Gallais, A. Sacuto, M. A. Measson, D. Colson, A. Forget, M. Bibes, A. Barthelemy, M. Cazayous. *Electric-field control of spin waves at room temperature in multiferroic  $BiFeO_3$* . Nat. Mater. **9**, 12, pp. 975–979 (2010)
- [95] Y. Tokura, N. Kida. *Dynamical magnetoelectric effects in multiferroic oxides*. Phil. Trans. Royal Soc. A **369**, 1951, p. 3679 (2011), URL <http://rsta.royalsocietypublishing.org/content/369/1951/3679.abstract>
- [96] A. M. Shuvaev, A. A. Mukhin, A. Pimenov. *Magnetic and magnetoelectric excitations in multiferroic manganites*. J. Phys.: Condens. Matter **23**, 11, p. 113201 (2011), URL <http://stacks.iop.org/0953-8984/23/i=11/a=113201>
- [97] A. B. Sushkov, M. Mostovoy, R. V. Aguilar, S.-W. Cheong, H. D. Drew. *Electromagnons in multiferroic  $RMn_2O_5$  compounds and their microscopic origin*. J. Phys.: Condens. Matter **20**, 43, p. 434210 (2008), URL <http://stacks.iop.org/0953-8984/20/434210>

- [98] G. A. Smolenskii, I. E. Chupis. *Ferroelectromagnets*. Sov. Phys. Usp. **25**, 7, p. 475 (1982), URL <http://stacks.iop.org/0038-5670/25/i=7/a=R02>
- [99] R. V. Aguilar, M. Mostovoy, A. B. Sushkov, C. L. Zhang, Y. J. Choi, S.-W. Cheong, H. D. Drew. *Origin of Electromagnon Excitations in Multiferroic RMnO<sub>3</sub>*. Phys. Rev. Lett. **102**, 4, 047203 (pp. 4) (2009), URL <http://link.aps.org/abstract/PRL/v102/e047203>
- [100] J. S. Lee, N. Kida, S. Miyahara, Y. Takahashi, Y. Yamasaki, R. Shimano, N. Furukawa, Y. Tokura. *Systematics of electromagnons in the spiral spin-ordered states of RMnO<sub>3</sub>*. Phys. Rev. B **79**, 18, 180403 (pp. 4) (2009), URL <http://link.aps.org/abstract/PRB/v79/e180403>
- [101] M. P. V. Stenberg, R. de Sousa. *Model for twin electromagnons and magnetically induced oscillatory polarization in multiferroic RMnO<sub>3</sub>*. Phys. Rev. B **80**, 9, 094419 (2009), URL <http://link.aps.org/abstract/PRB/v80/e094419>
- [102] A. Pimenov, A. M. Shuvaev, A. A. Mukhin, A. Loidl. *Electromagnons in multiferroic manganites*. J. Phys.: Condens. Matter **20**, 43, p. 434209 (2008), URL <http://stacks.iop.org/0953-8984/20/434209>
- [103] D. Senff, N. Aliouane, D. N. Argyriou, A. Hiess, L. P. Regnault, P. Link, K. Hradil, Y. Sidis, M. Braden. *Magnetic excitations in a cycloidal magnet: the magnon spectrum of multiferroic TbMnO<sub>3</sub>*. J. Phys.: Condens. Matter **20**, 43, p. 434212 (2008), URL <http://stacks.iop.org/0953-8984/20/434212>
- [104] H. Katsura, A. V. Balatsky, N. Nagaosa. *Dynamical Magnetoelectric Coupling in Helical Magnets*. Phys. Rev. Lett. **98**, 2, 027203 (pp. 4) (2007), URL <http://link.aps.org/abstract/PRL/v98/e027203>
- [105] A. Pimenov, A. Shuvaev, A. Loidl, F. Schrettle, A. A. Mukhin, V. D. Travkin, V. Y. Ivanov, A. M. Balbashov. *Magnetic and Magnetoelectric Excitations in TbMnO<sub>3</sub>*. Phys. Rev. Lett. **102**, 10, 107203 (pp. 4) (2009), URL <http://link.aps.org/abstract/PRL/v102/e107203>
- [106] A. Cano. *Theory of electromagnon resonances in the optical response of spiral magnets*. Phys. Rev. B **80**, p. 180416 (2009), URL <http://link.aps.org/doi/10.1103/PhysRevB.80.180416>
- [107] D. Senff, P. Link, K. Hradil, A. Hiess, L. P. Regnault, Y. Sidis, N. Aliouane, D. N. Argyriou, M. Braden. *Magnetic Excitations in Multiferroic TbMnO<sub>3</sub>: Evidence for a Hybridized Soft Mode*. Phys. Rev. Lett. **98**, 13, 137206 (pp. 4) (2007), URL <http://link.aps.org/abstract/PRL/v98/e137206>
- [108] M. Mostovoy. *Ferroelectricity in Spiral Magnets*. Phys. Rev. Lett. **96**, 6, 067601 (pp. 4) (2006), URL <http://link.aps.org/abstract/PRL/v96/e067601>

- 
- [109] M. Kenzelmann, A. B. Harris, S. Jonas, C. Broholm, J. Schefer, S. B. Kim, C. L. Zhang, S.-W. Cheong, O. P. Vajk, J. W. Lynn. *Magnetic Inversion Symmetry Breaking and Ferroelectricity in  $TbMnO_3$* . Phys. Rev. Lett. **95**, 8, p. 087206 (2005)
- [110] A. Shuvaev. *Spectroscopic study of manganites with magnetoelectric coupling*. Ph.D. thesis, University of Würzburg, Würzburg (2012), URL <http://opus.bibliothek.uni-wuerzburg.de/volltexte/2013/7871/>
- [111] A. Shuvaev, V. Dziom, A. Pimenov, M. Schiebl, A. A. Mukhin, A. C. Komarek, T. Finger, M. Braden, A. Pimenov. *Electric Field Control of Terahertz Polarization in a Multiferroic Manganite with Electromagnons*. Phys. Rev. Lett. **111**, p. 227201 (2013), URL <http://link.aps.org/doi/10.1103/PhysRevLett.111.227201>
- [112] N. Kida, Y. Ikebe, Y. Takahashi, J. P. He, Y. Kaneko, Y. Yamasaki, R. Shimano, T. Arima, N. Nagaosa, Y. Tokura. *Electrically driven spin excitation in the ferroelectric magnet  $DyMnO_3$* . Phys. Rev. B **78**, 10, 104414 (pp. 9) (2008), URL <http://link.aps.org/abstract/PRB/v78/e104414>
- [113] L. Landau, E. Lifshitz. *Electrodynamics of Continuous Media*. Course of Theoretical Physics, Pergamon Press (1975)
- [114] A. M. Kuzmenko, A. Shuvaev, V. Dziom, A. Pimenov, M. Schiebl, A. A. Mukhin, V. Y. Ivanov, L. N. Bezmaternykh, A. Pimenov. *Giant gigahertz optical activity in multiferroic ferroborate*. Phys. Rev. B **89**, p. 174407 (2014), URL <https://link.aps.org/doi/10.1103/PhysRevB.89.174407>
- [115] A. M. Kuzmenko, V. Dziom, A. Shuvaev, A. Pimenov, M. Schiebl, A. A. Mukhin, V. Y. Ivanov, I. A. Gudim, L. N. Bezmaternykh, A. Pimenov. *Large directional optical anisotropy in multiferroic ferroborate*. Phys. Rev. B **92**, p. 184409 (2015), URL <https://link.aps.org/doi/10.1103/PhysRevB.92.184409>
- [116] A. M. Kuzmenko, D. Szaller, T. Kain, V. Dziom, L. Weymann, A. Shuvaev, A. Pimenov, A. A. Mukhin, V. Y. Ivanov, I. A. Gudim, L. N. Bezmaternykh, A. Pimenov. *Switching of Magnons by Electric and Magnetic Fields in Multiferroic Borates*. Phys. Rev. Lett. **120**, p. 027203 (2018), URL <https://link.aps.org/doi/10.1103/PhysRevLett.120.027203>



# List of own publications

- A. M. Kuzmenko, D. Szaller, T. Kain, V. Dziom, L. Weymann, A. Shuvaev, Anna Pimenov, A. A. Mukhin, V. Y. Ivanov, I. A. Gudim, L. N. Bezmaternykh, A. Pimenov, *Switching of magnons by electric and magnetic fields in multiferroic borates*, Phys. Rev. Lett. 120, 027203 (2018) [URL](#)
- A. M. Shuvaev, V. Dziom, N. N. Mikhailov, Z. D. Kvon, Y. Shao, D. N. Basov, A. Pimenov, *Band structure of a two-dimensional Dirac semimetal from cyclotron resonance*, Phys. Rev. B 96, 155434 (2017) [URL](#)
- V. Dziom, A. Shuvaev, N. N. Mikhailov, A. Pimenov, *Terahertz properties of Dirac fermions in HgTe films with optical doping*, 2D Materials 4, 024005 (2017) [URL](#)
- V. Dziom, A. Shuvaev, A. Pimenov, G. V. Astakhov, C. Ames, K. Bendias, J. Böttcher, G. Tkachov, E. M. Hankiewicz, C. Brüne, H. Buhmann, L. W. Molenkamp, *Observation of the universal magnetoelectric effect in a 3D topological insulator*, Nature Communications 8, 15197 (2017) [URL](#)
- A. Shuvaev, V. Dziom, Z. D. Kvon, N. N. Mikhailov, A. Pimenov, *Universal Faraday rotation in HgTe wells with critical thickness*, Phys. Rev. Lett. 117, 117401 (2016) [URL](#)
- A. M. Kuzmenko, A. A. Mukhin, V. Y. Ivanov, G. A. Komandin, A. Shuvaev, A. Pimenov, V. Dziom, L. N. Bezmaternykh, I. A. Gudim, *Terahertz spectroscopy of crystal-field transitions in magnetoelectric  $TmAl_3(BO_3)_4$* , Phys. Rev. B 94, 174419 (2016) [URL](#)
- A. M. Kuzmenko, V. Dziom, A. Shuvaev, Anna Pimenov, M. Schiebl, A. A. Mukhin, V. Y. Ivanov, I. A. Gudim, L. N. Bezmaternykh, A. Pimenov, *Large directional optical anisotropy in multiferroic ferroborate*, Phys. Rev. B 92, 184409 (2015) [URL](#)
- M. Schiebl, A. Shuvaev, A. Pimenov, G. E. Johnstone, V. Dziom, A. A. Mukhin, V. Yu. Ivanov, A. Pimenov, *Order-disorder type critical behavior at the magnetoelectric phase transition in multiferroic  $DyMnO_3$* , Phys. Rev. B 91, 224205 (2015) [URL](#)
- A. A. Mukhin, A. M. Kuzmenko, V. Ivanov, A. G. Pimenov, A. M. Shuvaev, V. E. Dziom, *Dynamic magnetoelectric phenomena with electromagnons in rare-earth borate multiferroics*, Physics-Uspekhi 58, 993 (2015) [URL](#)

- A. M. Kuzmenko, A. Shuvaev, V. Dziom, A. Pimenov, M. Schiebl, A. A. Mukhin, V. Y. Ivanov, L. N. Bezmaternykh, A. Pimenov, *Giant gigahertz optical activity in multiferroic ferroborate*, Phys. Rev. B 89, 174407 (2014) [URL](#)
- A. Shuvaev, V. Dziom, Anna Pimenov, M. Schiebl, A. A. Mukhin, A. C. Komarek, T. Finger, M. Braden, A. Pimenov, *Electric field control of terahertz polarization in a multiferroic manganite with electromagnons*, Phys. Rev. Lett. 111, 227201 (2013) [URL](#)
- A. M. Vasiliev, L. A. Prozorova, L. E. Svistov, V. Tsurkan, V. Dziom, A. Shuvaev, Anna Pimenov, A. Pimenov, *ESR of the quasi-two-dimensional antiferromagnet  $\text{CuCrO}_2$  with a triangular lattice*, Phys. Rev. B 88, 144403 (2013) [URL](#)
- V. Dziom, A. Shevchun, M. Trunin, “*Whispering-gallery*” modes for surface impedance measurements of superconducting crystals, Trudy MFTI (in russian), Vol. 3, 3 (11) (2011) [URL](#)

# Curriculum Vitae

## Personal data

Name	Uladzislau Dziom
E-mail	dziom@ifp.tuwien.ac.at
Date of birth	2 Nov 1988
Place of birth	Vitebsk, Belarus

## Education

2012 – 2018	Vienna University of Technology E138 Institute of Solid State Physics Ph.D. student. Supervisor: Prof. Dr. Andrei Pimenov
2010 – 2012	Moscow Institute of Physics and Technology Institute of Solid State Physics, Chernogolovka, Russia Master degree in general and applied physics. Supervisor: Dr. Mikhail Trunin
2006 – 2010	Moscow Institute of Physics and Technology Bachelor degree in general and applied physics
2002 – 2006	School #31, Vitebsk, Belarus
1995 – 2002	School #28, Vitebsk, Belarus

## Employment

2012 – 2018	Project assistant in Solid State Spectroscopy group E138 Institute of Solid State Physics, Vienna University of Technology
June – Dec 2015	Guest researcher in Basov IR Laboratory University Of California San Diego
2009 – 2012	Chief laboratory assistant in Laboratory of Electron Kinetics Institute of Solid State Physics, Chernogolovka, Russia.